



J U S T A S Š E R E I K A

---

**I N V E S T I G A T I O N O F  
T H E I N F L U E N C E O F  
A C T I V E A N D P A S S I V E  
C O N T R O L M E T H O D S  
O N T H E D Y N A M I C S  
A N D S T R U C T U R E O F  
S E P A R A T E D  
S I N G L E - P H A S E F L O W**

---

D O C T O R A L D I S S E R T A T I O N

K a u n a s  
2 0 2 4

LITHUANIAN ENERGY INSTITUTE

JUSTAS ŠEREIKA

INVESTIGATION OF THE INFLUENCE OF  
ACTIVE AND PASSIVE CONTROL METHODS  
ON THE DYNAMICS AND STRUCTURE OF  
SEPARATED SINGLE-PHASE FLOW

Doctoral Dissertation

Technological Sciences, Energetics and Power Engineering (T 006)

2024, Kaunas

This doctoral dissertation was prepared at Lithuanian Energy Institute, Laboratory of Heat-Equipment Research and Testing during the period of 2020–2024. The studies were supported by Research Council of Lithuania.

The doctoral right has been granted to Kaunas University of Technology together with Lithuanian Energy Institute.

**Scientific Supervisors:**

Dr. Nerijus PEDIŠIUS (Lithuanian Energy Institute, Technological Sciences, Energetics and Power Engineering, T 006) (September 2020 – February 2024).

Senior Researcher Dr. Paulius VILKINIS (Lithuanian Energy Institute, Technological Sciences, Energetics and Power Engineering, T 006) (March 2024 – August 2024).

Edited by: English language editor Karolina Petraškaitė (UAB “BELLA VERBA”), Lithuanian language editor Loretė Sarapinienė (No. 713767).

**Dissertation Defence Board of Energetics and Power Engineering Science Field:**

Assoc. Prof. Dr. Robertas POŠKAS (Kaunas University of Technology, Technological Sciences, Energetics and Power Engineering, T 006) – **chairperson**;

Prof. Dr. Algirdas MAKNICKAS (Vilnius Gediminas Technical University, Technological Sciences, Mechanical Engineering, T 009);

Prof. Dr. Hab. Gintautas MILIAUSKAS (Kaunas University of Technology, Technological Sciences, Energetics and Power Engineering, T 006);

Prof. Dr. Martin OBLIGADO (École Centrale de Lille, France, Technological Sciences, Energetics and Power Engineering, T 006);

Assoc. Prof. Dr. Linas PAUKŠTAITIS (Kaunas University of Technology, Technological Sciences, Energetics and Power Engineering, T 006).

The public defence of the dissertation will be held at 10 a.m. on 26 September 2024 at the public meeting of Dissertation Defence Board of Energetics and Power Engineering Science Field in Conference room at Lithuanian Energy Institute.

Address: Breslaujos 3-202, LT-44403 Kaunas, Lithuania.

Phone: +370 37 401801; e-mail [studijos@lei.lt](mailto:studijos@lei.lt)

Doctoral dissertation was sent out on 26 August, 2024.

The doctoral dissertation is available on the internet <http://ktu.edu> and at the libraries of Kaunas University of Technology (Gedimino 50, LT-44239 Kaunas, Lithuania) and Lithuanian Energy Institute (Breslaujos 3, LT-44403 Kaunas, Lithuania).

© J. Šereika, 2024

LIETUVOS ENERGETIKOS INSTITUTAS

JUSTAS ŠEREIKA

AKTYVIŲ IR PASYVIŲ VALDYMO METODŲ  
ĮTAKOS ATITRŪKUSIO VIENFAZIO SRAUTO  
DINAMIKAI IR STRUKTŪRAI TYRIMAS

Daktaro disertacija

Technologijos mokslai, energetika ir termoinžinerija (T 006)

2024, Kaunas

Disertacija rengta 2020-2024 metais Lietuvos energetikos instituto Šiluminių įrengimų tyrimo ir bandymų laboratorijoje. Mokslinius tyrimus rėmė Lietuvos mokslo taryba.

Doktorantūros teisė Kauno technologijos universitetui suteikta kartu su Lietuvos energetikos institutu.

### **Moksliniai vadovai:**

dr. Nerijus PEDIŠIUS (Lietuvos energetikos institutas, technologijos mokslai, energetika ir termoinžinerija, T 006) (2020 m. rugsėjis – 2024 m. vasaris).

vyresn. m. d. dr. Paulius VILKINIS (Lietuvos energetikos institutas, technologijos mokslai, energetika ir termoinžinerija, T 006) (2024 m. kovas – 2024 m. rugpjūtis).

Disertaciją redagavo: anglų kalbos redaktorė Karolina Petraškaitė (UAB “BELLA VERBA”), lietuvių kalbos redaktorė Loretė Sarapinienė (IVP Nr. 713767).

### **Energetikos ir termoinžinerijos mokslo krypties disertacijos gynimo taryba:**

doc. dr. Robertas POŠKAS (Kauno technologijos universitetas, technologijos mokslai, energetika ir termoinžinerija, T 006) – **pirmininkas**;

prof. dr. Algirdas MAKNIČKAS (Vilniaus Gedimino technikos universitetas, technologijos mokslai, mechanikos inžinerija, T 009);

prof. habil. dr. Gintautas MILIAUSKAS (Kauno technologijos universitetas, technologijos mokslai, energetika ir termoinžinerija, T 006);

prof. dr. Martin OBLIGADO (Centrinis Lilio Institutas, Prancūzija, technologijos mokslai, energetika ir termoinžinerija, T 006);

doc. dr. Linas PAUKŠTAITIS (Kauno technologijos universitetas, technologijos mokslai, energetika ir termoinžinerija, T 006).

Disertacija bus ginama viešame Energetikos ir termoinžinerijos mokslo krypties disertacijos gynimo tarybos posėdyje 2024 m. rugsėjo 26 d. 10 val. Lietuvos energetikos instituto Posėdžių salėje.

Adresas: Breslaujos g. 3-202, LT-44403 Kaunas, Lietuva.

Tel: +370 37 401801; el. paštas studijos@lei.lt

Disertacija išsiųsta 2024 m. rugpjūčio 26 d.

Su disertacija galima susipažinti interneto svetainėje <http://ktu.edu>, Kauno technologijos universiteto bibliotekoje (Gedimino g. 50, LT-44239 Kaunas, Lietuva) ir Lietuvos energetikos instituto skaitykloje (Breslaujos g. 3, LT-44403 Kaunas, Lietuva).

# CONTENTS

LIST OF TABLES .....	8
LIST OF FIGURES.....	9
NOMENCLATURE.....	12
ABBREVIATIONS.....	15
INTRODUCTION.....	16
1. LITERATURE ANALYSIS.....	19
1.1. Flow over backward-facing step.....	19
1.2. Flow in cavities.....	21
1.3. Flow control.....	24
1.3.1. Active flow control.....	25
1.3.1.1. Pulsatile flow in channels sudden cross-section changes ....	26
1.3.2. Passive flow control.....	28
1.3.2.1. Flow over roughness elements .....	28
1.3.2.2. Flow in channels with different step configurations .....	30
1.4. The overview of literature analysis and the author’s contribution to the research field .....	31
2. METHODOLOGY AND EQUIPMENT .....	33
2.1. Physical object.....	33
2.2. Experimental facility .....	35
2.2.1. PIV set-up.....	35
2.2.2. $\mu$ PIV set-up.....	36
2.2.3. Image analysis .....	37
2.2.4. Stationary and pulsatile inlet conditions.....	38
2.2.5. Reynolds number calculations.....	39
2.2.6. The uncertainty of flow rate and velocity calculations.....	40
2.2.7. The uncertainty of recirculation zone length measurements ....	41
2.2.8. Turbulence intensity and phase velocity calculations in pulsatile flow.....	41
2.3. Numerical simulation .....	42

2.3.1.	Reynolds averaged Navier-Stokes equations.....	44
2.3.2.	Meshing .....	45
2.3.3.	Boundary conditions.....	47
2.4.	Comparison between results of experiments and numerical simulations.....	47
3.	RESULTS AND DISCUSSION.....	49
3.1.	Recirculation zone dynamics of stationary flow in cavities .....	49
3.2.	Active flow control.....	51
3.2.1.	Recirculation zone behaviour during the pulsation cycle .....	52
3.2.2.	Pulsation amplitude impact on recirculation zone dynamics....	53
3.2.3.	Pulsation amplitude impact on statistical flow parameters.....	56
3.2.3.1.	Impact of pulsation amplitude on turbulence intensity distribution in the cavity .....	57
3.2.3.2.	Impact of pulsation amplitude on vorticity and shear rate distribution in the cavity .....	59
3.2.4.	The impact of pulsation frequency on flow structure .....	61
3.2.4.1.	Pulsation frequency impact on recirculation zone development during pulsation cycle.....	61
3.2.4.2.	Pulsation frequency impact on the corner and upper vortices in a closed-type cavity .....	63
3.2.4.3.	Pulsation frequency impact on share rate distribution in a closed-type cavity .....	64
3.2.5.	Recirculation zone length dependency on Re comparison with other studies.....	66
3.3.	Passive flow control.....	67
3.3.1.	Adjustment of cavity geometrical parameters .....	67
3.3.1.1.	Cavity inner corner curvature influence on the velocity distribution.....	68
3.3.1.2.	Cavity outlet/inlet hydraulic diameter ratio impact on the longitudinal velocity distribution.....	72
3.3.2.	Implementation of roughness elements .....	74
3.3.2.1.	Roughness element impact on velocity distribution inside a cavity.....	75

3.3.2.2.	Impact of roughness elements on shear rate distribution.....	80
3.3.2.3.	Pressure drop characteristics and friction factor dependence of roughness element configuration.....	82
	CONCLUSIONS.....	85
4.	SANTRAUKA.....	87
	ĮVADAS.....	87
4.1.	Literatūros apžvalga .....	90
4.2.	Tyrimų metodika ir įranga.....	92
4.2.1.	Eksperimentiniai tyrimo metodai .....	92
4.2.1.1.	PIV įrenginys.....	92
4.2.1.2.	μPIV įrenginys .....	93
4.2.1.3.	Matavimų neapibrėžtis .....	94
4.2.2.	Skaitinis modeliavimas.....	94
4.3.	Tyrimų rezultatai .....	95
4.3.1.	Recirkuliacinės zonos dinamika, esant stacionariam tekėjimui kavernoje.....	96
4.3.2.	Aktyvus srauto valdymas.....	97
4.3.2.1.	Recirkuliacinės zonos elgsena pulsacijų ciklo metu .....	98
4.3.2.2.	Pulsacijų amplitudės įtaka recirkuliacinės zonos dinamikai ...	99
4.3.2.3.	Pulsacijų amplitudės įtaka statistiniams srauto parametrams	101
4.3.2.4.	Pulsacijų dažnio įtaka srauto struktūrai.....	104
4.3.2.5.	Recirkuliacinės zonos ilgio priklausomybės nuo Re palyginimas su kitų autorių darbais.....	105
4.3.3.	Pasyvus srauto valdymas .....	106
4.3.3.1.	Kavernos geometrinių parametrų įtaka srauto struktūrai .....	106
4.3.3.2.	Šiurkštumo elementų įtaka srauto struktūrai ir slėgio nuostoliams kanale.....	111
	IŠVADOS .....	117
	REFERENCES.....	119
	CURRICULUM VITAE .....	128
	PUBLICATIONS RELATED TO THE DISSERTATION .....	129



## LIST OF TABLES

<b>Table 1</b> Schemes and dimensions of the experimental channels .....	34
<b>Table 2</b> Amplitude and pulsation frequency of different flow cases .....	52
<b>1 lentelė.</b> Tiriamųjų tekėjimo atvejų parametrų vertės.....	98

## LIST OF FIGURES

<b>Fig. 1</b> The separated flow field behind the BFS .....	19
<b>Fig. 2</b> The classification of cavities by the ratio of cavity length and step height: a) open-type cavity; b) transitional type cavity; c) closed-type cavity. ....	22
<b>Fig. 3</b> Classification of flow control methods .....	25
<b>Fig. 4</b> Characteristics of steady and pulsatile flow: (A) – steady flow; (B) – pulsatile flow; (C) – oscillatory flow .....	26
<b>Fig. 5</b> PIV system scheme .....	36
<b>Fig. 6</b> $\mu$ PIV system scheme .....	37
<b>Fig. 7</b> Principal scheme of PIV image processing.....	38
<b>Fig. 8</b> Variation of pressure during the pulsation cycle with different pulsation amplitudes.....	39
<b>Fig. 9</b> Volumetric flow rate calibration curve .....	39
<b>Fig. 10</b> Representation of a structured mesh in a 2D closed-type cavity .....	46
<b>Fig. 11</b> Mesh independency test in a) open-type cavity, b) closed-type cavity.....	47
<b>Fig. 12</b> Comparisons of numerically and experimentally obtained results in a) open-type cavity at $Re_{Dh} = 1000$ ; b) closed-type cavity .....	48
<b>Fig. 13</b> Stationary flow streamlines in a transitional-type cavity ( $L/h_1 = 8$ ) .....	49
<b>Fig. 14</b> Recirculation zone length dependency on $Re_{h1}$ in transitional- and closed-type cavity with $L/h_1 = 8$ and $L/h_1 = 16$ , respectively.....	50
<b>Fig. 15</b> Numerically obtained flow velocity streamlines in an open-type cavity ( $L/h_1 = 4$ ) .....	51
<b>Fig. 16</b> Flow velocity streamline variation in transitional-type cavity ( $L/h_1 = 8$ ) during the pulsation cycle of $A = 0.60$ and $f = 0.5$ Hz .....	52
<b>Fig. 17</b> Time-averaged velocity streamlines in a transitional-type cavity at $Re_{h1} = 50$ – $2000$ for stationary flow and pulsatile flow with $A = 0.15$ and $0.60$ .....	54
<b>Fig. 18</b> Experimentally obtained dependency of the relative recirculation zone length on $Re_{h1}$ in stationary and pulsatile flow.....	55
<b>Fig. 19</b> The impact of amplitude on recirculation zone length in laminar and transitional flow regimes .....	56
<b>Fig. 20</b> $Tl$ profiles at $Re_{h1}$ values of a) 500, b) 1000 c) 1500, and d) 2000.....	58
<b>Fig. 21</b> Relative vorticity $\omega/\omega_{max}$ contours in transitional type cavity of both stationary and pulsatile flow cases with different amplitudes at $Re_{h1} = 1500$ .....	59
<b>Fig. 22</b> Longitudinal shear rate profile along the transitional-type cavity at $Re_{h1}$ values of a) 100, b) 500, c) 1500, and d) 2000 .....	60
<b>Fig. 23</b> The dependency of recirculation zone on velocity phase angle in a closed-type cavity ( $L/h_1 = 16$ ) a) $Re_{h1} = 300$ ; b) $Re = 1500$ .....	62
<b>Fig. 24</b> Numerically simulated dependency of the relative length of the corner and upper vortices on velocity phase angle at different pulsation frequencies: a) corner vortex; b) upper vortex .....	63
<b>Fig. 25</b> Velocity streamlines of the flow during different pulsation phases at $Re = 1500$ ; $f = 1$ Hz and $A = 1$ : a) $\varphi = 0^\circ$ ; b) $\varphi = 45^\circ$ ; c) $\varphi = 90^\circ$ ; d) $\varphi = 135^\circ$ ; e) $\varphi = 180^\circ$ ; f) $\varphi = 225^\circ$ ; g) $\varphi = 270^\circ$ ; h) $\varphi = 315^\circ$ .....	64

<b>Fig. 26</b> Experimentally obtained vertical shear rate profiles at different closed-type cavity locations at a) $Re_{h1} = 300$ ; b) $Re_{h1} = 1500$ .....	65
<b>Fig. 27</b> Experimentally obtained shear rate profile along the closed-type cavity at $y/H = 0.5$ and $Re_{h1} = 1500$ .....	66
<b>Fig. 28</b> The comparison of recirculation zone length dependency on $Re$ with other studies.....	67
<b>Fig. 29</b> Open-type cavities with a different curvature radius of inner corners.....	68
<b>Fig. 30</b> Numerically obtained $u_x$ profiles in open-type cavities with different step configurations at a) $Re_{Dh} = 10$ ; b) $Re_{Dh} = 100$ ; c) $Re_{Dh} = 1000$ .....	69
<b>Fig. 31</b> Velocity streamlines in Ch1, Ch2 and Ch3 .....	70
<b>Fig. 32</b> $x-z$ axis velocity profiles at a) $Re_{Dh} = 10$ ; b) $Re_{Dh} = 100$ ; c) $Re_{Dh} = 1000$ ....	71
<b>Fig. 33</b> $x-z$ plane velocity streamlines in Ch1, Ch2 and Ch3 .....	72
<b>Fig. 34</b> The scheme of an open-type cavity ( $L/h_1 = 4$ ) with the location of the longitudinal velocity profile .....	73
<b>Fig. 35</b> Longitudinal velocity distribution in the middle of the open-type cavity with a different outlet to inlet hydraulic diameter ratio, at a) $Re_{Dh} = 10$ ; b) $Re_{Dh} = 100$ ; c) $Re_{Dh} = 1000$ .....	74
<b>Fig. 36</b> Schematic representation of experimental channel with different number of roughness elements: a – 0; b – 1; c – 2; d – 3.....	75
<b>Fig. 37</b> Velocity streamlines in cavities with different roughness element configurations at $Re_{Dh} = 430 - 12000$ .....	77
<b>Fig. 38</b> Velocity profiles measured in cavities with the configuration of roughness elements; a) and b) $\lambda = 8.8$ ; c) and d) $\lambda = 4.7$ ; e) and f) $\lambda = 3.3$ ; g) and h) $\lambda = 2.8$ , at $Re_{Dh} = 430 - 15000$ .....	79
<b>Fig. 39</b> Shear rate scalar maps in the cases of a), b) plane cavity; c), d) $\lambda = 4.7$ ; e), f) $\lambda = 3.3$ ; g), h) $\lambda = 2.8$ , at $Re_{Dh} = 430$ and $Re_{Dh} = 12000$ .....	80
<b>Fig. 40</b> Shear rate $\gamma/\gamma_0$ profiles along measured cavities: a) plain cavity; b) $\lambda = 4.7$ ; c) $\lambda = 3.3$ ; d) $\lambda = 2.8$ , at $Re_{Dh} = 430 - 12000$ .....	81
<b>Fig. 41</b> Friction factor dependence on $Re_{Dh}$ for different roughness element configurations .....	83
<b>Fig. 42</b> Pressure drop dependence on different configurations of roughness elements at different $Re_{Dh}$ .....	84
<b>43 pav.</b> Atgalinį laiptą aptekancio srauto struktūros schema .....	90
<b>44 pav.</b> PIV įrenginio schema .....	93
<b>45 pav.</b> $\mu$ PIV įrenginio schema.....	94
<b>46 pav.</b> Struktūrizuoto tinklelio pavyzdys 2D uždarojo tipo kavernoje.....	95
<b>47 pav.</b> Srauto linijos pereinamojo tipo kavernoje, esant stacionariam tekėjimui ...	96
<b>48 pav.</b> Recirkuliacinės zonos ilgio priklausomybė nuo $Re_{h1}$ pereinamojo ir uždarojo tipo kavernoje su $L/h_1 = 8$ ir $L/h_1 = 16$ , atitinkamai .....	97
<b>49 pav.</b> Srauto linijos esant stacionariam tekėjimui atvirojo tipo kavernoje ( $L/h_1 = 4$ ) .....	97
<b>50 pav.</b> Srauto linijos pulsacinio ciklo metu pereinamojo tipo kavernoje, esant $A = 0,60$ ir $f = 0,5$ Hz.....	99

<b>51 pav.</b> Recirkuliacinės zonos ilgio priklausomybė nuo $Re_{h1}$ , esant stacionariam ir pulsuojančiam tekėjimui, pereinamojo ir uždarojo tipo kavernoje .....	100
<b>52 pav.</b> Recirkuliacinės zonos pokyčio priklausomybė nuo amplitudės, esant pulsuojančiam tekėjimui.....	101
<b>53 pav.</b> <i>TI</i> profiliai, esant a) $Re_{h1} = 500$ ; b) $Re_{h1} = 1000$ ; c) $Re_{h1} = 1500$ ; d) $Re_{h1} = 2000$ .....	102
<b>54 pav.</b> Išilginio šlyties greičio horizontalūs profiliai pereinamojo tipo kavernoje, esant a) $Re_{h1} = 100$ ; b) $Re_{h1} = 500$ ; c) $Re_{h1} = 1500$ ; d) $Re_{h1} = 2000$ .....	103
<b>55 pav.</b> Recirkuliacinės zonos ilgio priklausomybė nuo pulsacijų ciklo fazės kampo uždarojo tipo kavernoje, esant a) $Re_{h1} = 300$ ; b) $Re_{h1} = 1500$ .....	104
<b>56 pav.</b> Recirkuliacinės zonos ilgio priklausomybės nuo $Re_{h1}$ palyginimas su kitų autorių darbais .....	105
<b>57 pav.</b> Skaičiavimams naudotų trimačių atviro tipo kavernų geometrijos su skirtingai apvalintais vidiniais kampais.....	106
<b>58 pav.</b> Santykinio greičio profiliai <i>x-y</i> ašyje atviro tipo kavernoje, esant a) $Re_{Dh} = 10$ ; b) $Re_{Dh} = 100$ ; c) $Re_{Dh} = 1000$ .....	107
<b>59 pav.</b> Greičio srauto linijos atviro tipo kavernoje, esant skirtingoms vidinių kavernos kampų konfigūracijoms.....	108
<b>60 pav.</b> Santykinio greičio profiliai <i>x-z</i> plokštumoje atviro tipo kavernoje, esant a) $Re_{Dh} = 10$ ; b) $Re_{Dh} = 100$ ; c) $Re_{Dh} = 1000$ .....	109
<b>61 pav.</b> Atviro tipo kaverna ( $L/h_1 = 4$ ) su išilginio greičio profilio lokacija.....	110
<b>62 pav.</b> Išilginio greičio pasiskirstymas, esant skirtingiems ištekėjimo ir įtekėjimo hidraulinių diametrų santykiams, esant a) $Re_{Dh} = 10$ ; b) $Re_{Dh} = 100$ ; c) $Re_{Dh} = 1000$ .....	111
<b>63 pav.</b> Kanalas su skirtingu skaičiumi šiurkštumo elementų: a) 0; b) 1; c) 2; d) 3	111
<b>64 pav.</b> Vidutinio greičio srauto linijose kavernoje su skirtinga šiurkštumo elementų konfigūracija, esant $Re_{Dh} = 430 - 12000$ .....	113
<b>65 pav.</b> Šlyties greičio pasiskirstymas, esant a, b - $\lambda = 8,8$ ; c, d - $\lambda = 4,7$ ; e, f - $\lambda = 3,3$ ; g, h - $\lambda = 2,8$ .....	114
<b>66 pav.</b> Trinties koeficiento priklausomybė nuo $Re_{Dh}$ , esant skirtingai šiurkštumo elementų konfigūracijai kavernoje .....	115
<b>67 pav.</b> Slėgio nuostolių priklausomybė nuo atstumo tarp šiurkštumo elementų $\lambda$	116

## NOMENCLATURE

$A$	[-]	Pulsation amplitude, $A = \frac{p_{max}}{p_0}$
AR	[-]	Aspect ratio, $AR = \frac{b}{h}$
$b$	[m]	Cavity width
$C_f$	[-]	Skin friction coefficient, $C_f = \frac{\tau_w}{\frac{1}{2}\rho v^2}$
$d$	[m]	Distance between pressure measurement points
$D_h$	[m]	Hydraulic diameter, $D_h = \frac{2hb}{(h+b)}$
$D_{h\_in}$	[m]	Inlet hydraulic diameter,
$D_{h\_out}$	[m]	Outlet hydraulic diameter,
ER	[-]	Expansion ratio, $ER = \frac{H}{h_1}$
$f$	[Hz]	Pulsation frequency
$fr$	[-]	Friction factor, $fr = \frac{2\Delta p D_h}{d\rho v^2}$
$h$	[m]	Channel inlet/outlet height
$H$	[m]	Height of the channel in the cavity cross-section, $H = (h + h_1)$
$h'$	[m]	Vertical velocity profile height
$h_1$	[m]	Cavity step height
$L$	[m]	Cavity length
$L_{ch}$	[m]	Characteristic length
$l$	[m]	Length between roughness elements vertices
$p$	[Pa]	Pressure
$p_0$	[Pa]	Mean inlet pressure
$p_{max}$	[Pa]	Maximum pressure of pulsation cycle
$Q$	[m <sup>3</sup> /s]	Volumetric flow rate
$R$	[m]	Radius of curvature

$Re$	[-]	Reynolds number, $Re = \frac{QL_{ch}\rho}{S\mu}$
$Re_{h1}$	[-]	Reynolds number, where the characteristic length is the height of the step, $Re = \frac{Qh_1\rho}{S\mu}$
$Re_{Dh}$	[-]	Reynolds number, where the characteristic length is the hydraulic diameter, $Re = \frac{QD_h\rho}{S\mu}$
$S$	[m <sup>2</sup> ]	Inlet surface area
$s$	[m]	Roughness element height
$t$	[s]	Time
$T$	[s]	Time period, $T = \frac{1}{f}$
$T_{\circ C}$	[°C]	Ambient temperature.
$TI$	[-]	Turbulence intensity, $TI = \frac{U'}{U}$
$u$	[m/s]	Velocity, $u = \sqrt{u_x^2 + u_y^2}$
$\bar{u}$	[m/s]	Mean phase velocity
$U$	[m/s]	Mean inlet velocity, $U = \frac{Q}{S}$
$u'$	[m/s]	Velocity fluctuation
$U'$	[m/s]	Mean phase flow fluctuation
$u_{\max}$	[m/s]	Maximum velocity
$u_x$	[m/s]	$x$ -axis velocity
$u_{x,rms}$	[m/s]	Root mean square of $x$ -axis velocity
$u_y$	[m/s]	$y$ -axis velocity
$u_{\phi}$	[m/s]	Phase velocity
$Wo$	[-]	Womersley number, $Wo = \sqrt{\frac{fD_h^2}{\nu}}$
$x_1$	[m]	Distance to the beginning of the upper vortex
$x_2$	[m]	Distance to the end of the upper vortex

$x_R$	[m]	Length of the recirculation zone
$\gamma$	[1/s]	Shear rate, $\gamma = \frac{\partial u_x}{\partial y} + \frac{\partial u_y}{\partial x}$ $\gamma = \partial U/\partial y + \partial V/\partial x$
$\Delta p$	[Pa]	Pressure loss
$\varepsilon$	[m]	Roughness size
$\lambda$	[-]	Subcavity length to roughness element height ratio, $\lambda = \frac{l}{s}$ ;
$\mu$	[kg/(m×s)]	Dynamic viscosity
$\nu$	[m <sup>2</sup> /s]	Kinematic viscosity
$\tau$	[s]	Measurement time
$\varphi$	[°]	Pulsation phase angle
$\omega$	[-]	Vorticity, $\omega = \frac{\partial u_x}{\partial y} - \frac{\partial u_y}{\partial x}$

## ABBREVIATIONS

BFS	–	Backward-facing step
FFS	–	Forward-facing step
RANS	–	Reynolds averaged Navier-Stokes
LES	–	Large eddy simulation
PIV	–	Particle image velocimetry
CCD	–	Charge-coupled device
CFD	–	Computational fluid dynamics
FVM	–	Finite volume method



## INTRODUCTION

Flow separation in channels with sudden changes in cross-section is a fundamental process in numerous engineering applications, including the airflow around vehicles, buildings, airfoils, and spoilers. (Chen et al., 2018). This phenomenon is often encountered in flow dynamics, heat transfer enhancement, particle trapping, and related research fields. (Faure, 2014, Shen et al., 2015, 2017, Wang et al., 2022). All of these research fields focus on similar problems – flow instabilities, turbulence, vortex shedding, and similar complex behaviour, which need to be controlled in order to enhance the performance of fluidic systems, promote energy efficiency, extend the lifespan of mechanical components by stabilising the heat transfer processes, etc. The necessity for flow control comes from the inherent complexities posed by fluid behaviour in diverse systems; therefore, flow control is a promising field of fluid dynamics, and it is in rapid development due to the high attention of researchers (Ghaemi, 2020, Bergadà et al., 2023, Yin, 2023).

Factors impacting flow separation are usually studied by employing the PIV method, as it allows precise measurements of flow structure to be performed in a non-intrusive way. The PIV method has been significantly developed in recent years since the equipment required for it and image processing methods have been vastly improved (Rohacs et al., 2023). Experimental visualisation of the flow is often combined with computational fluid dynamics (CFD), which lets to expand the research capabilities even further. These complex studies, which combine both experimental and numerical analysis, are often met in flow control studies (Vanierschot et al., 2014, Bardera et al., 2021, Fan et al., 2022).

Recently, a lot of active flow control methods have been extensively studied, including synthetic jets, electromagnetic forcing, rotation, forced oscillations, pulsatile flow, etc. (Chen et al., 2022). It is known that the most significant alteration of fluid characteristics can be achieved by creating pulsatile flow conditions (McEvoy et al., 2019). The studies of pulsatile flow are getting increasingly more attention regarding its effects on the heat transfer processes, although studies of its effects on separated fluid dynamics are scarce.

Passive flow control is often preferred due to its inherent simplicity. One of the most common passive flow control methods that are gaining a lot of attention is the implementation of roughness elements (Liu et al., 2019, Zhang et al., 2019, Gao et al., 2022, Han et al., 2022, Li et al., 2024). Implementation of roughness elements is known to have a significant impact on separated flow, and unwanted outcomes can be avoided by manipulating their configuration. The separated flow can also be controlled by manipulating the geometrical parameters of the channel, thus increasing the stability of the flow and ensuring uniform velocity distribution (Bentaleb et al., 2012, Das et al., 2016).

Studies of separated fluid flow control efficiency provide the necessary fundamental knowledge, which allows the enhancement of the performance of fluid

systems by eliminating the unwanted outcomes of fluid behaviour, resulting in improved efficiency and possible reduction of energy consumption.

### **Object of the Research**

Separated flow dynamics and structure in channels with sudden cross-section changes.

### **The aim of Doctoral Dissertation**

The aim of this work is to experimentally and numerically investigate the flow which is influenced by pulsations, roughness elements and geometrical parameters, and to determine the factors defining the recirculation zone dynamics and separated flow structure in cavities.

### **Tasks of the Doctoral Dissertation**

In order to achieve the objective, the following tasks should be solved:

1. To determine the influence of pulsation frequency and amplitude on time-averaged recirculation zone length in cavities.
2. To determine the formation and development regularities of the recirculation zone during the pulsation cycle in cavities.
3. To determine the influence of pulsations on the turbulence intensity distribution in cavities.
4. To determine the influence of geometrical parameters such as inner cavity corner curvature and outlet/inlet hydraulic diameter ratio to the velocity distribution inside of a cavity.
5. To determine the influence of roughness elements on velocity distribution and pressure loss in cavities.

### **Statements carried out for defence**

1. Pulsatile flow reduces the recirculation zone length in laminar and transitional flow regimes, with the magnitude of the effect inversely proportional to pulsation amplitude in the laminar regime.
2. The alterations in the development of the recirculation zone during the different frequency pulsation cycle occur due to the different responses of the recirculation zone to the pulsation period.
3. Velocity fluctuations caused by pulsatile flow are relevant to turbulent intensity only in transitional flow regime.
4. Cavity inner corner curvature has no impact on the flow structure; however, a significant impact is caused by the outlet/inlet hydraulic diameter ratio, which affects the longitudinal velocity as the fluid approaches the forward-facing step.

5. The pressure losses directly depend on the length between the triangular roughness elements until the critical size of subcavities formed between the roughness elements is reached.

### **Scientific novelty**

This study improves fundamental knowledge of flow structure and recirculation zone dynamics influenced by flow control methods, which allows for determining the behaviour regularities of additional vortices, identifying the flow control method determinants of efficiency, and identifying the origin of velocity fluctuations in different regimes.

### **Practical value**

The practical significance of flow control research lies in its potential to enhance the performance of fluid systems, resulting in improved efficiency and reduced energy consumption. Provided knowledge on passive flow control has the potential to reduce costs associated with various engineering systems even further, as it does not require external energy sources. Moreover, the combination of flow separation and pulsatile flow is a prevalent technique employed in the biomedical field, where fundamental knowledge of flow control is necessary for microfluidic system improvement.

### **Scientific approval**

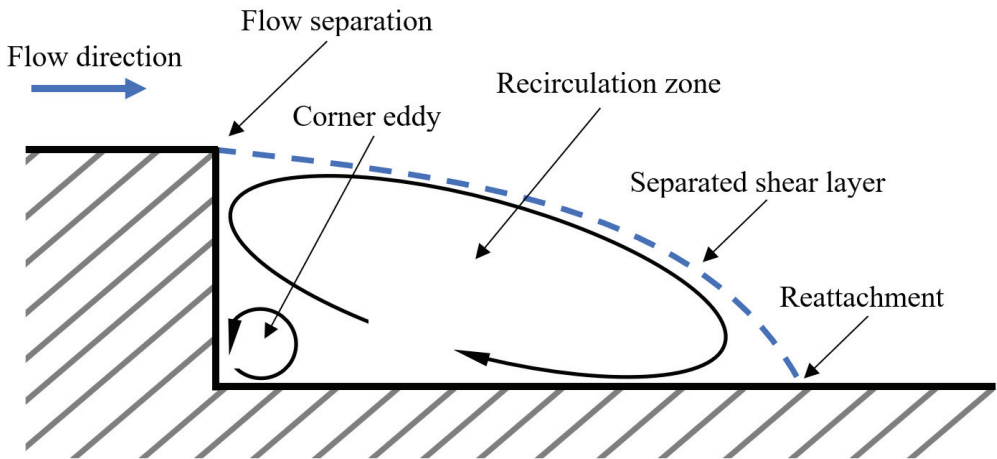
The results presented in this dissertation were published in 4 scientific articles in journals with an impact factor that is referenced in the “Clarivate Analytics” “Web of Science” database. The results were also presented at 3 international conferences.

## 1. LITERATURE ANALYSIS

The phenomenon of flow separation in channels with sudden geometric changes is a frequent subject in fluid dynamics research. Examining the dynamics and structure of separated flow enhances our understanding of fundamental fluid mechanics and facilitates its application in practical scenarios. Both numerical and experimental methods are extensively used to study the steady flow structure and dynamics of separated flow. This phenomenon is commonly observed in general flow dynamics, heat transfer enhancement, particle separation, and related research areas (Shen et al., 2015, 2017, Wang et al., 2022, Abbas et al., 2023, Islam et al., 2023, Murugan et al., 2023).

### 1.1. Flow over backward-facing step

A common way to study separated flows is by studying flow over a backward-facing step (BFS), which is a widely studied phenomenon in fluid dynamics due to its simple geometry and complex physics behind it (Fig. 1).



**Fig. 1** The separated flow field behind the BFS

Up to the present day, the flow over BFS is a relevant fluid dynamics topic (Wu et al., 2022, Goktepe et al., 2023, Julian et al., 2023, Manna et al., 2023, Varun Kumar et al., 2023), as it addresses such aspects as flow separation, flow transition and instabilities, frequent industrial and engineering applicability, and flow control. A lot of work has been done on these topics, and the general regularities of fluid behaviour have already been determined. One of the main parameters describing the flow structure is recirculation zone length. Armaly et al. (Armaly et al., 1983) investigated the flow over BFS and defined every flow regime based on recirculation zone length variation. At the laminar flow regime, the recirculation zone length depends on  $Re$  in an almost linear manner. The transitional flow regime starts as the

recirculation zone length starts decreasing with increasing  $Re$ , due to the presence of instabilities that are caused by the transitional flow itself. Eventually, in a turbulent flow regime, the recirculation zone length reaches its asymptotical value, where it no longer depends on  $Re$ . However, the recirculation zone length does not solely rely on  $Re$ . It can also be impacted by geometrical parameters such as aspect ratio ( $b/h$ ) and expansion ratio ( $H/h$ ). A relatively small aspect ratio can cause three-dimensional instabilities, which may alter the recirculation zone length and cause changes in velocity distribution (Williams et al., 1997). Lim et al. (Lim et al., 1990) performed a combined numerical and experimental study on three-dimensional flow characteristics behind BFS. The authors showed that recirculation zone length is up to 25% shorter in a channel with  $AR = 3.3$  compared to the case of typical two-dimensional flow over BFS. Barkley et al. (Barkley et al., 2002) investigated the three-dimensional instabilities in a narrow channel with BFS and discovered that the main three-dimensional instabilities occur at  $Re = 748$  and  $AR = 2$ . The expansion ratio also has a significant impact on recirculation zone dynamics, and its effects are also widely studied (Cheng et al., 2005). Stogiannis et al. (Stogiannis et al., 2014) showed that recirculation zone length depends on ER almost linearly. The authors showed that by increasing  $H/h$  from 1.25 to 2.5, the recirculation zone length can be increased by up to 60%. These results coincide with a numerical and experimental study by Gong et al. (Gong et al., 1996), where a linear relation of recirculation zone length with ER is determined. Therefore, when studying the dynamics of recirculation zone length, it is necessary to determine the fixed values of geometrical parameters to avoid various instabilities that may alter the behaviour of separated flow and impact flow structure defining parameters such as recirculation zone length.

The instabilities of separated flow are caused not only by the geometrical features. During transitional and turbulent flow regimes, the flow becomes unstable due to periodically recurring vortices (Vilkinis et al., 2020), leading to a complex flow structure. The separated flow is unsteady and presents global instabilities, thus resulting in pressure oscillations (Deng et al., 2020, Ezzatneshan, 2021, Chavan et al., 2022, Guerra et al., 2023). Ma et al. (Ma et al., 2022) performed a study regarding the stability issues at  $Re$  right above its critical value ( $Re = 1000$ ), at which the separated/reattaching shear layer becomes unstable and starts to evolve three-dimensional chaotic structures. Their velocity measurements performed with time-resolved PIV show that the separated shear layer remains two-dimensional in the near wake of the step, and subsequently, it starts to evolve three-dimensional structures, including the coexisting spanwise streaks and vertical flapping motions, in the latter half of the shear layer. Tihon et al. (Tihon et al., 2010) investigated the stability in flow over BFS and defined that the magnitude of velocity fluctuations in the near-wall region is a consequence of the local mean velocity. The spectral analysis performed by the authors showed that the low frequency fluctuations dominate the reattachment region under steady inlet flow conditions. Biswas et al. (Biswas et al., 2004) revealed

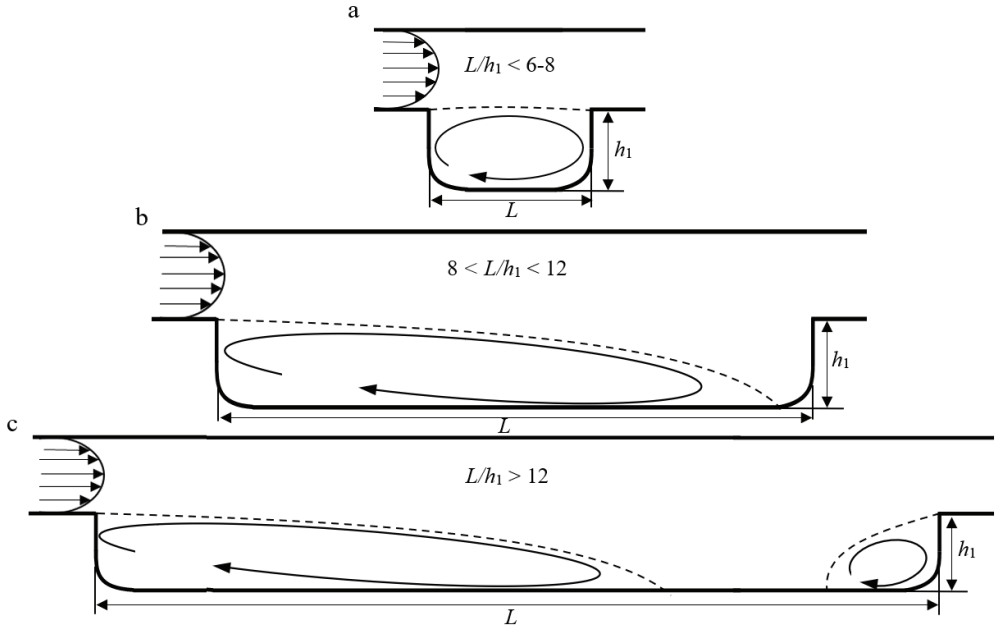
that when  $Re > 400$ , the flow becomes three-dimensional due to the effect of sidewall and shows oscillatory behaviour. Additionally, the authors managed to determine the pressure loss dependency on the expansion ratio of the channel, where a high expansion ratio caused high pressure losses. Beaudoin et al. (Beaudoin et al., 2004) reported the existence of a three-dimensional stationary structure with a periodicity in the spanwise direction of the flow. The origin of these instabilities is consistent with a centrifugal instability, which appears in the vicinity of the reattached flow and outside of the recirculation zone.

It is known that unstable flow may alter heat transfer processes. Chen et al. (Chen et al., 2006) presented the simulations of turbulent convection flow adjacent to a two-dimensional BFS to explore the effects of step height on turbulent separated flow and heat transfer. The authors showed that the heat transfer efficiency is directly proportionate to step height as the simulated temperature decreases inside the recirculation zone and reaches the minimum value near the reattachment region. Such regularities of temperature distribution may lead to overheated surfaces if not appropriately addressed. Xie et al. (Xie et al., 2017) presented a direct numerical simulation of the vortical structure behind BFS and its effect on the heat transfer process in the transitional flow regime. The authors indicated that in the region after separated shear layer reattachment (when length to step height ratio is between 6 and 14) the heat transfer was enhanced at  $Re = 1200$ . The intensified heat transfer was identified by magnified Nusselt (Nu) number fluctuations.

The regularities of different instabilities in separated flows directly affect heat transfer. Instabilities, such as Kelvin-Helmholtz and Görtler vortices, amplify the complexity of flow patterns, resulting in fluctuations in velocity, pressure, and temperature fields (Issakhov et al., 2021). These instabilities can lead to enhanced heat transfer in some regions and reduced heat transfer in others; therefore, studies addressing the flow structure in channels with BFS have received significant attention and have had an impactful value to this day.

## **1.2. Flow in cavities**

A cavity is a type of channel with sudden cross section expansion and contraction created by implementing BFS and forward-facing steps (FFS). It creates a more intricate flow configuration compared to a channel with BFS. The BFS induces flow separation and recirculation in the upstream region, while the FFS alter the flow further and may lead to additional separation and recirculation downstream. Cavities exhibit complex fluid interactions resulting in a combination of flow separation, recirculation zone and vortex shedding since they follow the same recirculation zone growth regularities depending on  $Re$ . These interactions have a significant impact on heat transfer processes.



**Fig. 2** The classification of cavities by the ratio of cavity length and step height: a) open-type cavity; b) transitional type cavity; c) closed-type cavity.

It is generally agreed to classify cavities into three types: open-type cavity ( $L/h_1 < 6 - 8$ ), transitional-type cavity ( $8 < L/h_1 < 12$ ) and closed-type cavity ( $L/h_1 > 12$ ) (Fig. 2)(Tracy et al., 1997). The classification of cavities relies on cavity length and step height ratio as they cause different flow behaviours. For instance, closed flow occurs in closed-type cavities where the flow detaches from BFS and then reattaches at the bottom of the cavity. In contrast, open flow occurs when the spacing between steps is too small for the flow to reattach at the bottom of the cavity, causing the shear layer to bridge across the cavity.

Numerous detailed investigations into the dynamics of separated flow in cavities have been conducted to comprehend the underlying hydrodynamics. Chung et al. (Chung et al., 2017) demonstrated that maximum fluctuations occur in a transitional-type cavity due to a sufficiently large downstream region and a closely positioned rear edge of the cavity. Additionally, an investigation into the shear layer structure within the cavity revealed that the cavity oscillations were sinusoidal in shape (Desikan et al., 2022). Given the various studies on flow structures, numerous investigations have been conducted on both open- and closed-type cavities. Fishler et al. (Fishler et al., 2013) performed an experimental study on microscale cylindrical cavities, examining how geometry and  $Re$  on the flow structure. Faure et al. (Faure et al., 2009, Faure, 2014) provided a thorough analysis of flow structures in open-type cavities, particularly focusing on flow instabilities. Shen et al. (Shen et al., 2015) studied rectangular microcavities at low  $Re$ , identifying three flow patterns – attached,

separated, and transitional – based on the reattachment of the separated shear layer to the bottom wall of the channel. Guo and Luo (Guo et al., 2019) investigated the connection between depth-to-length ratio and flow structure, visualizing transitions between various cavity flow types. Zhang et al. (Zhang et al., 2002) identified threshold values for the length-to-depth ratio that indicate transitions between different flow regimes. Vilkinis and Pedišius (Vilkinis et al., 2020) analysed the dynamics of the recirculation zone length in both transitional- and closed-type cavities, showing their dependence on length-to-depth and expansion ratios. Henderson et al. (Henderson et al., 2000) explored the time-dependent flow structures in transitional-type cavities under subsonic flow conditions. Changes in the vortex system’s configuration throughout the cycle produce dumbbell-like flow patterns involving a stretched primary vortex near the BFS and a diminished secondary vortex near the FFS, which eventually merges with the primary vortex at the end of the cycle. The time-averaged flow pattern features a single elongated vortex near the leading edge, extending across most of the cavity and reattaching to the bottom wall.

Coleman et al. (Coleman et al., 2007) and Leonardi et al. (Leonardi et al., 2003) investigated turbulent flow within rectangular cavities separated by square bars. In transitional-type cavities, opposing-rotating vortices govern the flow, with a larger recirculation region upstream and a smaller one near the forward-facing step. Cheng and Hung (Cheng et al., 2006) employed the lattice Boltzmann method to explore vortex structures in a two-dimensional, lid-driven open-type cavity, varying the cavity’s length-to-depth ratio ( $L/h_1$ ) and Re. This investigation revealed how vortex structures are influenced by these factors, particularly showcasing the changes when  $L/h_1 \leq 1$  and how the number of vortices increases as  $L/h_1$  decreases and Re increases. Similarly, Faure et al. (Faure et al., 2007) carried out flow visualisation within an open-type cavity at moderate Re (1150 – 10670) and varying length-to-step-height ratios ( $L/h_1 = 0.5-2$ ). Their analysis indicated that secondary instabilities in the shear layer do not induce 3D developments, and a secondary vortex in the upstream cavity is linked to the instability of the main vortex.

The flow dynamics research field is inherently connected to heat transfer studies due to the influence of recirculation zone development. In open-type cavities, heat transfer has been extensively studied. Bilgen et al. (Bilgen et al., 2005) examined natural convection-driven heat transfer in partially closed cavities with  $L/h_1 = 1$ , revealing the dependence of the Nu on the Rayleigh number (Ra), aspect ratio, aperture position, and inclination angle. Muftuoglu et al. (Muftuoglu et al., 2008) investigated natural convection heat transfer in open-type cavities with a discrete heat source, determining optimal heater positions in relation to Ra and assessing the impact of channel aspect ratios. Prakash et al. (Prakash et al., 2012) investigated the convective loss in open-type cavities, revealing that the highest convective loss occurs in a hemispherical cavity with specific opening ratios. Laouira et al. (Laouira et al., 2020) explored mixed convection in a trapezoidal open-type cavity with varying heat



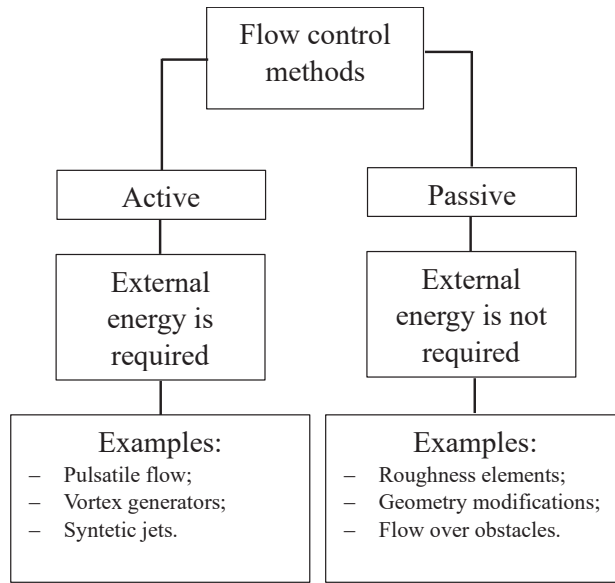
source lengths, finding a correlation between the highest Nu and the longest heat source and observing heat transfer enhancement altering the velocity distribution within the cavity.

Studies of flow in cavities offer the necessary fundamental knowledge in hydrodynamic processes, which may lead to enhanced heat exchange and efficiency in various practical applications. However, the literature analysis shows that when the flow is affected by sudden expansions and contractions, it leads to instabilities and perturbations, usually unwanted fluid behaviour, as it may cause various critical measures. By understanding the already thoroughly studied behaviour of confined and separated fluid flows, it is possible to enhance their stability, which may lead to increased efficiency and performance of multiscale fluid devices.

### **1.3. Flow control**

Flow control is a promising field of fluid dynamics which is in rapid development due to its high practical significance, attracting a lot of scientists' attention (Joshi et al., 2016, Bergadà et al., 2023, Yin, 2023). Fluid control is focused on manipulating the behaviour and characteristics of flows in various practical applications, such as aerospace, automotive, biomedical engineering, energy production, heating ventilation and air conditioning systems, etc. (Chen et al., 2018). The knowledge obtained from studying flow control techniques is inherent in enhancing the efficiency of various industrial processes by altering flow rates, adjusting pressure gradients, and employing specific equipment to control fluid flow.

Flow control techniques are usually separated into two groups – active and passive flow control (Fig. 3) (Ghaemi, 2020, Lalitha et al., 2022, Moulinos et al., 2022). Active flow control aims to alter the natural flow and achieve specific performance enhancements by using external energy. Passive flow control refers to the manipulation and optimisation of the fluid behaviour using intrinsic features of surface, structure, or geometry without the addition of external energy.



**Fig. 3** Classification of flow control methods

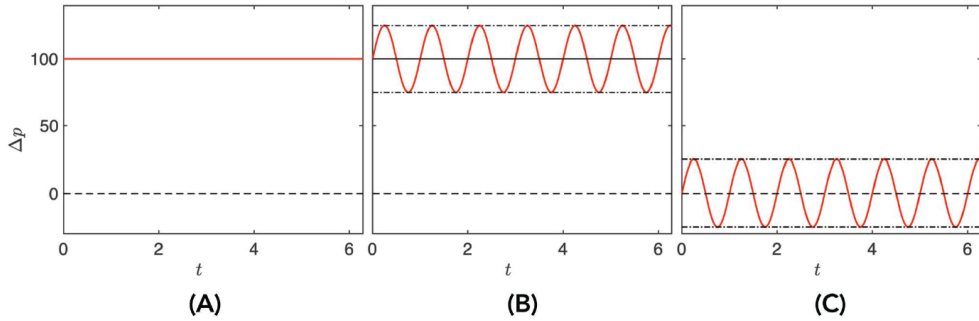
The need for flow control arises from the inherent complexities and challenges posed by fluid behaviour in various systems. Fluid flows exhibit turbulence, separation, and other complexities that may hinder the performance and desired outcomes. For instance, separated flow incurs a large amount of energy loss and limits the performance of many flow-related devices, such as aeroplanes, diffusers, etc. (Tian et al., 2006, Pochylý et al., 2019, Xia et al., 2021, Oyeniran et al., 2022). Separated flow may lead to diminished heat-exchange processes and increased pressure losses (Chun et al., 1996). These outcomes from the unwanted process of fluid separation can be altered by employing flow control techniques.

The focus of the present work is directed towards the separated fluid dynamics caused by sudden expansion and contraction of the channel. Therefore, the literature analysis is constructed by first reviewing research works in the general separated fluid dynamics field. Afterwards, the impact of active and passive flow control methods on separated flow is reviewed. Finally, a short discussion is made, where the aim and tasks of this work are formed and discussed.

### 1.3.1. Active flow control

Over the years, a significant number of active flow control methods have been studied, including synthetic jets, electromagnetic forcing, rotation, forced oscillations, pulsatile flow, etc. (Chen et al., 2022). Of all these methods, pulsatile flow has shown the most significant impact on heat transfer intensification (McEvoy et al., 2019). The heat exchange magnification effects of pulsatile flow have been theoretically and experimentally proven (van Buren et al., 2019, Zhang, Bian, et al., 2019, Dawood et

al., 2024). Ward et al. (Ward et al., 2015) defined the enhancement of heat transfer processes as a consequence of intensified fluid mixing under pulsatile flow conditions. However, with the intensified fluid mixing comes physical complexity, such as induced unsteady flow separation and transient wall shear stresses (Dol et al., 2014). These complexities have brought significant attention due to their value in many practical applications (Chen et al., 2018).



**Fig. 4** Characteristics of steady and pulsatile flow: (A) – steady flow; (B) – pulsatile flow; (C) – oscillatory flow (Dincau et al., 2020)

Before discussing the effects of pulsatile flow, it is necessary to define what type of it is analysed. The characteristics of steady and pulsatile flow are given in Fig. 4. When the flow is driven by a constant differential pressure, a steady flow is obtained (Fig. 4 (A)). When the pressure periodically varies – two types of flow are obtained: pulsatile and oscillatory (Fig. 4(B) and (C)). The main difference between pulsatile and oscillatory flows is the fluid movement. In pulsatile flow, the fluid constantly flows in one direction, while in oscillatory flow, the average velocity in an ideal instance is 0. In pulsatile flow, the fluid is influenced by both viscous and inertia forces resulting from the pulsatile nature, even at low  $Re$ .

### 1.3.1.1. Pulsatile flow in channels sudden cross-section changes

The implementation of the BFS in channel geometry facilitates the observation of various outcomes resulting from the pulsatile flow. Initially, pulsations lead to increased shear rate values on the lower channel wall (Tihon et al., 2010, 2012), which is a phenomenon related to fluid mixing. Regardless of pulsation frequency, pulsations tend to increase wall shear rate, thereby reinforcing the reverse flow within the recirculation zone (Valencia, 1997, Valencia et al., 1997). Furthermore, the pulsations induce magnified vorticity in the fluid flow (Dandois et al., 2007), consequently exerting an influence on heat exchange by magnifying the heat transfer within the region of the recirculation zone across varying  $Re$ . Additionally, heat transfer under specific pulsation parameters displays an enhancement of up to 70% when contrasted with a steady flow (Davletshin et al., 2019).

Secondly, flow pulsations result in a reduction of the recirculation zone length. The flow at different  $Re$  has an optimal pulsation frequency with the most significant effect (Tihon et al., 2001, 2010, 2012). The magnitude of recirculation zone length reduction depends on pulsation amplitude, frequency and  $Re$  (Tihon et al., 2012). In the laminar flow, the most significant effect occurs at lower frequencies ( $f < 1$  Hz), whereas within the transitional flow regime, the highest influence is observed at higher pulsation frequencies ( $1 \text{ Hz} < f < 3 \text{ Hz}$ ) (Tihon et al., 2010). Due to the shortened recirculation zone during pulsatile flow, the fully developed parabolic velocity profile occurs at a reduced distance from the step in the channel (Salek et al., 2009).

Within the pulsatile cycle, as the flow velocity continues changing, the development of the separated flow emerges as an interesting foundational subject, although research in this area is scarce. Only few studies have been conducted to investigate the flow characteristics during this pulsatile cycle (Ibrahim et al., 1994, Valencia, 1997, Valencia et al., 1997). In the pulsatile flow, at the beginning of the cycle, the  $x_R$  value is the same as that of the steady flow under the corresponding instantaneous Reynolds number (Valencia, 1997). This occurrence has been termed as “quasi-steady” after a comparison of numerical and experimental findings (Ibrahim et al., 1994). The comparison revealed that the flow behaviour is quasi-steady under the conditions of laminar flow with a low pulsation frequency. However, the flow departs from this quasi-steady state as the pulsation frequency increases. Moreover, the impact of pulsations on the development of the flow structure becomes more impacted with increasing  $Re$  numbers. Notably, the formation of a vortex on the upper channel wall materialises at lower  $Re$  numbers in comparison to stationary flow (Dol et al., 2014, Dol, 2016).

In many engineering applications, channel expansion is limited by an FFS, forming a cavity in the channel where flow dynamics become more complex. Studies of pulsatile flow within open-type cavities are mainly focused on heat transfer processes (Cheng, 2005, Selimefendigil, 2016, Zamzari et al., 2017). These studies show that the enhancement of heat transfer is achieved by increasing  $Re$  and the amplitude of pulsations, though this enhancement is noticeable only at specific frequencies (Huang et al., 2018, Zhang, Bian, et al., 2019). In open-type cavities, the flow structure is defined by the interaction between the separated shear layer and FFS; therefore, the flow structure in the cavity is mainly determined by the geometry and flow pulsations have a negligible effect on it (Zhang, Bian, et al., 2019). Throughout the pulsation cycle, there are certain phases during which the mixing of fluids is strengthened; therefore, the heat transfer is enhanced. As the frequency of pulsations increases to a particular value, depending on the cavity size, fluid ejection from the cavity occurs (Nishimura et al., 2000).

Pulsatile flow in cavities has the most significant influence on vortical structures. The dynamics of vortices progress through distinct stages in contrast to

steady flows. Zhang et al. (Zhang et al., 2022) investigated the vortex dynamics within a deep rectangular cavity and observed that a five-stage evolution of vortices, namely generation, travelling, merging, stretching, and weakening, is affected by  $Re$  and Womersley number ( $Wo$ ). An increase in  $Re$  led to an earlier occurrence of the vortex evolution stages, whereas an increase in  $Wo$  brings the opposite effect. Due to changes in vortical patterns throughout the pulsation cycle, the average structure of stationary flow differed from that of pulsatile flow (Zhang, Bian, et al., 2019). Consequently, this led to changes in the flow structure and a reduction in the length of the recirculation zone (Velazquez et al., 2009, Dol et al., 2014). These changes affected the heat transfer efficiency parameters (Kherbeet et al., 2014) or pressure distribution in stenosis (MdMolla et al., 2017). Hence, there is a demand for generalised regularities in pulsatile flow within benchmark geometries to accelerate the development and enhance the effectiveness of applications associated with these explored phenomena. Currently, the focus predominantly lies on flows in open-type cavities, while studies concerning longer cavities marked by the reattachment of separated shear layers to the bottom cavity wall are scarce.

### **1.3.2. Passive flow control**

The active flow control methods allow the separated fluid dynamics to be impacted, although its use often leads to energy loss and difficulties in implementing it. The use of passive flow control may be preferred owing to the simplicity of it. For instance, the implementation of roughness elements and manipulation of channel roughness is known to have an essential influence on the flow structure and heat transfer characteristics; therefore, the studies have become increasingly important and frequent during the past few years (Gao et al., 2022, Han et al., 2022, Li et al., 2024). An alternative approach to controlling the separated flow passively is the implementation of different curvature radius corners, which confines the fluid movement since it is known to significantly affect aerothermodynamic properties (Jin et al., 2021). It was observed that the attention to this simple passive flow control technique has been rising recently (Kumar et al., 2018, Bose et al., 2020, Alam, 2022, Ismail et al., 2022, Wang et al., 2024).

These two specific passive flow control methods have been chosen as they offer a huge potential for manipulating fluid dynamics in relatively simple ways. These methods will be discussed separately in the following subsections to gain a clearer understanding of how each technique independently affects the separated flow behaviour.

#### **1.3.2.1. Flow over roughness elements**

Flow studies over different roughness elements address the problems of flow resistance and problems related to heat transfer. To enhance heat transfer efficiency, rough surfaces find extensive applications as they disrupt the thermal boundary layer.

The roughness characteristics on the channel walls impact pressure drop along the channel and elevate shear stress near the roughness elements. The behaviour of separated flow, whether it reconnects to the channel wall or bridges between roughness elements, depends on the roughness size and configuration. This leads to a reduction in effective flow area and an increase in pressure drop.

A literature survey shows that the alteration of channel wall roughness exerts an influence on pressure drop and the enhancement of heat transfer (Pelević et al., 2016, Yuan et al., 2016). Numerical simulations by Rovenskaya (Rovenskaya, 2017) and Zhang et al. (Zhang, Luo, et al., 2019) establish that the most significant effect is attributed to rectangular roughness. Roughness elements shaped as semicircles and trapeziums exhibit intermediate effects, following an ascending order. Notably, the highest friction losses are caused by rectangular roughness elements due to the formation of the largest recirculation zone behind them. However, trapezoidal, semicircular, and triangular elements generate smaller recirculation zones. An analysis of the spacing between roughness elements reveals a decrease in pressure drop as the distance between these elements is increased. Lalegani et al. (Lalegani et al., 2018) showed these findings in microchannels with roughness elements of various shapes on one wall, suggesting the consideration of heightened triangular surface roughness to mitigate pressure drop. In contrast, Zhang et al. (Zhang et al., 2010) numerically investigated the effects of roughness shape and size parameters on heat transfer in the laminar flow regime and demonstrated that triangular and semicircular roughness elements induce higher pressure drop, intensified recirculation, and an increased local Nu compared with rectangular roughness elements. Liu et al. (Liu, Han, et al., 2019) emphasised that the spacing between roughness elements becomes more important as roughness height diminishes. Moreover, it is generally agreed upon (Hu et al., 2003, Rawool et al., 2006, Lalegani et al., 2018) that higher roughness height triggers increased pressure drop, while expanded spacing between roughness elements diminishes pressure drop by allowing flow reattachment to the wall and an increase of the effective flow surface.

Coleman et al. (Coleman et al., 2007) investigated the flow structure over rectangular roughness elements with different spacing. Their study revealed that changes in the flow structure and adjustments in velocity profiles above these elements occur after exceeding a particular distance between them. Stoesser and Nikora (Stoesser et al., 2008) employed LES and revealed that the flow structure differs for roughness element spacings of  $l/s = 4.5$  and  $l/s = 9$ . These differences are in terms of the structure of the recirculation zone, as well as the distribution of turbulent intensities and shear stresses above the cavities.

Zhang et al. (Zhang et al., 2018) numerically investigated the heat transfer efficiency in channels featuring triangular roughness elements of varying sizes. The authors showed that specific sizes of triangular roughness elements contribute to a reduction in convective heat transfer efficiency due to the confinement of hot or cold

fluid within the cavities formed between these roughness elements, which restricts effective mixing with the bulk fluid. With an increase in roughness size approaching the critical dimension, inertial forces within the cavities intensify, resulting in intense mixing and an increased heat exchange efficiency.

### **1.3.2.2. Flow in channels with different step configurations**

Das and Cohen (Das et al., 2016) numerically and experimentally investigated flow in an open-type cavity with  $L/h_1 = 3.58$  to reduce pressure oscillations and noise by changing the rear face geometry of the cavity. Bentaleb et al. (Bentaleb et al., 2012) performed a numerical study on boundary layer separation along a gently curved step. The authors have shown that a rounded backward-facing step causes a tenuous separation process with a very shallow separation angle due to a thin reverse flow layer that covers the step. Bravo et al. (Bravo et al., 2000) measured the longitudinal mean velocity and turbulent intensity downstream of a backward-facing step with rounded edges. The authors showed that rounded step edges shorten the recirculation zone and significantly reduce the Reynolds stresses' peak. Kumar et al. (Kumar et al., 2018) numerically and experimentally studied the heat transfer and friction loss of turbulent flow in a duct of a triangular cross section. The authors concluded that the rounder corners create better fluid interaction at the corner with the main flow field, resulting in an increase of Nu, indicating the intensification of heat transfer processes. Kumar et al. (Kumar, 2017) numerically studied the supersonic turbulent flow over a backward-facing rounded step by using the hybrid RANS-LES / Spalart-Allmaras turbulence model. The authors unveiled that the gradual expansion occurs over the rounded step, leading to the delay in the separation of the viscous layer, causing the formation of a shorter shear layer along with the equally shorter recirculation zone. Marquet et al. (Marquet et al., 2006) studied the linear three-dimensional dynamics of a recirculation zone in a channel with rounded BFS. The authors highlighted that the mechanism associated with the transient amplification of two-dimensional perturbations is the Kelvin-Helmholtz mechanism, which is active in the shear layer of the recirculation zone. Neumann et al. (Neumann et al., 2004) investigated the coherent structures of turbulent separated flows over sharp-edged and rounded steps. The authors showed that the rounded step results in a much smaller recirculation zone than in the case of the sharp-edged step. Additionally, there are no secondary recirculation regions in the case of rounded steps, meaning that the flow is more stable. Wang et al. (Wang et al., 2020) numerically investigated the flow past cubes with rounded corners and examined the noise emitted to the far field. The authors revealed that the mean drag coefficient drops significantly once the cube is rounded, even with a small corner radius and length ratio. Additionally, the introduction of rounded corners changed the shape of the noise spectrum. The emitted noise is reduced significantly with the increase of the relative corner radius from  $R/L = 1/12$  to  $1/3$ , but the sound level increases again when  $R/L = 2/5$  due to vortex shedding.

#### **1.4. The overview of literature analysis and the author's contribution to the research field**

A literature survey shows that separated flow dynamics are primarily studied in channels with BFS, where both experimental and numerical works are focused on various 2D and 3D instabilities and recirculation zone dynamics in every flow regime. Researchers mostly focus on heat transfer efficiency problems or the impact of statistical flow parameters on them. Another big part of the studies is focused on open-type cavities and their heat exchange since the flow structure in such channels has already been thoroughly studied.

The problem of flow control is shown to be a perspective field of research, as it still requires further investigation. The works are also mainly scattered between two types of channels – the open-type cavities and channels with BFS. Active flow control methods such as pulsatile flow are mainly focused on heat transfer processes, and the analysis of pulsatile flow structure is scarce. Passive flow control methods are shifted towards the effects on the boundary layer or the heat transfer efficiency on roughness element configuration.

The literature analysis has identified areas that necessitate further research. For instance, the study of pulsatile flow has predominantly focused on either laminar or turbulent flows, with limited attention given to transitional flow phenomena. Exploring the transition of pulsatile flow from a laminar to a turbulent regime represents a fundamental inquiry that could unveil essential flow development mechanisms.

Moreover, investigations are currently lacking into the dynamics of recirculation zones and other recirculative regions, such as corner and upper vortices, during the pulsatile cycle. Additionally, the impact of pulsatile flow on the mixing process within separated shear layers requires more comprehensive exploration. While numerous studies of pulsatile flow have centred around pulsation frequency as a defining parameter for flow control efficiency, the influence of flow structure dependency on pulsation amplitude remains unexplored.

In the field of passive flow control methods, the primary focus has predominantly been on channels with boundary-fitted surfaces and the efficiency of heat transfer processes, often neglecting in-depth analysis of flow structures.

Concluding the research of other authors, it is possible to identify the key factors that determine the structure and behaviour of the actively and passively controlled separated flow in channels with sudden cross-section changes. The aim of this work is to experimentally and numerically study the flow which is influenced by pulsations, roughness elements and geometry parameters, and to determine the factors defining the recirculation zone dynamics and separated flow structure in cavities. It enhances the fundamental knowledge regarding flow control methods and provides the possibility of successfully implementing them in practical applications. This study is concentrated on separated flow control methods from a foundational perspective,



prioritising a comprehensive understanding over immediate practical use. The value of this research lies in the possibility of implementing the enhanced fundamental knowledge required to design efficient microfluid applications.

This dissertation is a continuation of the research initiated in P. Vilkinis' dissertation titled "Investigation of flow dynamics and structure in channels with structured surfaces" (Vilkinis, 2019), in which the author revealed the influence of cavities relative to height  $H/h_1$  and length  $L/h_1$  on separated flow structure and dynamics in different flow regimes under stationary flow conditions. The present study continues the previous work by focusing on the influence of flow control methods on the separated flow structure and dynamics. The author of the dissertation analysed the results regarding the differently controlled dynamics of separated fluid flow in variously shaped cavities. The experiments were conducted using the  $\mu$ PIV and PIV systems, whereas the numerical simulations were conducted using *Ansys Fluent* software. The experimental and numerical approaches were used to investigate the impact of active and passive flow control methods on the recirculation zone dynamics and the flow structure in open-, transitional- and closed-type cavities in a wide Re range, which covered all three flow regimes. The author identified the effects of pulsatile flow on the dynamics of recirculation zone lengths in different types of cavities and provided an analysis of statistical parameters that allow evaluation of the flow behaviour in all three flow regimes. The time-dependent behaviour of flow was analysed, and the regularities of recirculation zone dynamics during the pulsatile cycle were highlighted. Additionally, the analysis of pressure loss and friction characteristics were analysed in a flow impacted by roughness elements, which allows to approximately evaluate the possible energy loss due to a particular channel configuration. Finally, the impact of the cavity outlet/inlet hydraulic diameter ratio is defined by analysing the longitudinal velocity distribution between the leading and trailing edges of the cavity.

## 2. METHODOLOGY AND EQUIPMENT

In this section, the research methodology is reviewed, focusing on physical research object, experimental and numerical facilities, measurement error and uncertainty analysis.

### 2.1. Physical object

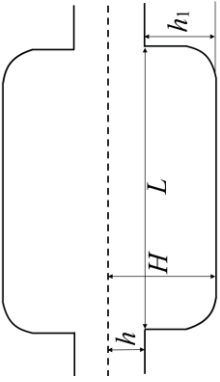
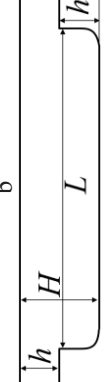

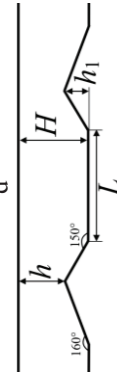
Experiments were conducted in a wide range of micro- and macro-scale cavities, with cavity length to step height ratio ( $L/h_1$ ) ranging from 4 to 16.

The experimental micro-channels (Table 1a, b, c) were custom manufactured from polycarbonate, with a precision declared by the manufacturers of  $\leq 20 \mu\text{m}$ . The micro-chip containing the manufactured micro-channels consists of two plates. The experimental micro-cavity is milled into the plate, while the second plate is glued on top of it.

The experimental macro-channel (Table 1d) was constructed from Plexiglas and designed with a modifiable geometry by embedding various elements as needed. It featured a rectangular cross-section, with two inclined ramps installed on the bottom wall to create a plain cavity between them. The leading and trailing ramps were set at a  $30^\circ$  angle, resulting in a length-to-depth ratio ( $L/h_1$ ) of 8.8 for the cavity. Additional triangular roughness elements, each with a height matching the cavity depth, were added to the cavity bottom.

Table 1 shows the schemes and dimensions of all experimental channels, including the range of Re in which the experiments were conducted.

**Table 1** Schemes and dimensions of the experimental channels

Geometry	ER	AR	H×h×h <sub>1</sub> ×L , mm	Re <sub>h1</sub>	L/h <sub>1</sub>	Cavity type	Applied flow control method	Analysis method	Numerical model
<p>a</p> 	3	3	0.45×0.15 ×0.3×1.2	6 – 666	4	Open	Geometrical parameter adjustment	Numerical	Laminar and <i>k-ε</i> standard
<p>b</p> 	2	3	0.4×0.2×0.2 ×1.6	50 – 2000	8	Transitio nal	Pulsatile flow	Experimental	–
<p>c</p> 	2	2	0.4×0.2× 0.2×3.2	50 – 1650	16	Closed	Pulsatile flow	Experimental and numerical	Reynolds stress-omega
<p>d</p> 	–	1/3	60×40×20 ×176	285 – 18000	4.4	Open	Roughness elements	Experimental	–

## 2.2. Experimental facility

The Particle Image Velocimetry (PIV) method is commonly used to investigate the behaviour and dynamics of fluids. PIV has gained widespread use in fluid mechanics due to its non-intrusive nature, which allows for measurements without perturbing the fluid. The technique involves seeding the fluid with tracer particles illuminated with a pulsed laser and then capturing their motion with a high-speed camera in successive image pairs. The velocity of the fluid can be determined by analysing the displacement of the tracer particles over a known time interval between image pairs. A more detailed explanation of the PIV method and its application are given in the following reference (Raffel et al., 2018).

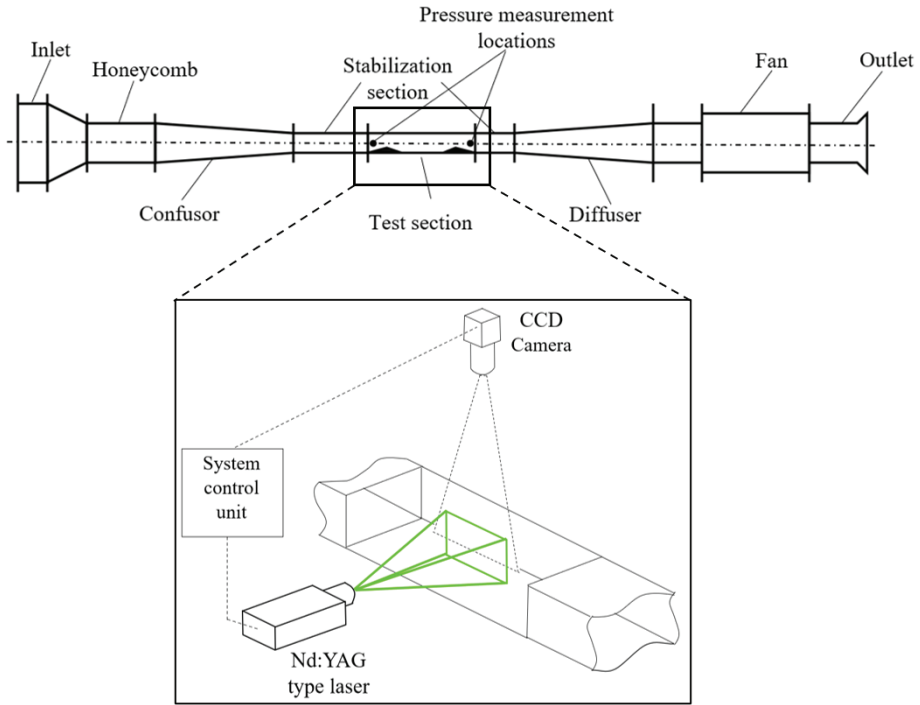
The present work employed two types of PIV systems, namely, regular PIV and micro-PIV ( $\mu$ PIV). Although both techniques operate on the same principle, they are designed for different experimental scales.

### 2.2.1. PIV set-up

The particle image velocimetry system (Fig. 5) used in the experiments consists of a Nd:YAG type laser Dual Power 200–15 (Dantec Dynamics), operating at up to 15 Hz frequency, with pulse energy up to 200 mJ, a wavelength of 532 nm, and pulse length of less than 10 ns. Images are recorded with a 4 Mpx FlowSense EO CCD camera (Dantec Dynamics) with a pixel size of 7.4  $\mu$ m, providing a field of view of approximately 240  $\times$  70 mm<sup>2</sup>. DynamicStudio software (Dantec Dynamics) is used for system control and image acquisition. 200 double-frame image pairs are obtained for each case, and three separate measurements are performed.

The seeding particles are generated from a sugar solution aerosol using the Six-Jet Atomizer 9306 (TSI), producing particles with a diameter of 0.3  $\mu$ m, a density of 1.58  $\times$  10<sup>3</sup> kg/m<sup>3</sup>, and a refractive index of 1.54. The sugar particles in the airflow had a relaxation time of 4  $\times$  10<sup>-7</sup> s, resulting in a Stokes number  $Stk \ll 1$ , indicating that the tracing particles closely followed fluid streamlines. The tracer particles are smaller than the size of individual pixels on the CCD camera, resulting in particle images that occupy the entirety of a single pixel despite being smaller than that pixel's dimensions.

The pressure is measured before and after the plain cavity at a distance of  $L = 460$  mm between measurement locations. FCO12 pressure sensors (Furness Controls) with a measurement range of 0–20 Pa are used, with an uncertainty of 0.5%. The velocity for Re calculations is measured with a thermo-anemometer Testo 435 (with a measurement range of 0 – 20 m/s and a measurement uncertainty of 14,3 – 0,5 %). The ambient temperature is maintained during the measurements at 20  $\pm$  1  $^{\circ}$ C.

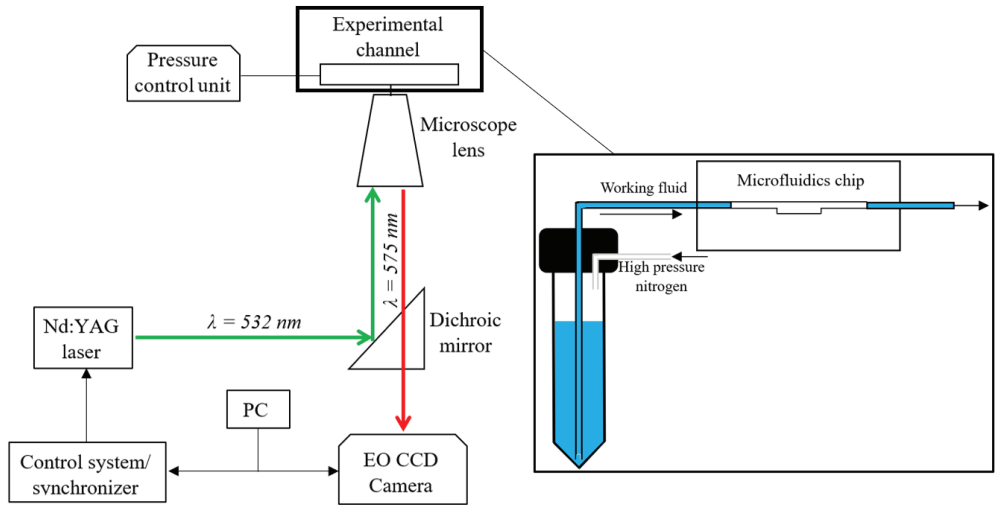


**Fig. 5** PIV system scheme

### 2.2.2. $\mu$ PIV set-up

The microparticle image velocimetry method involves tracking the motion of small tracer particles within a fluid. For this method, deionised water is used as the working fluid and is seeded with fluorescent particles measuring  $1\ \mu\text{m}$  in diameter with a specific gravity of 1.05. The temperature of the fluid is maintained at  $20\pm 1\ ^\circ\text{C}$ . The velocity components in the  $x$ - and  $y$ -axes were computed based on the change in the particle's location and the time elapsed between image pairs.

The  $\mu$ PIV system (Fig. 6) used for the experiment consisted of an Elveflow OB1 MK3 pressure control unit capable of generating inlet pressures up to 8 bar(g) in the experimental channel. The system also included a Nd:YAG laser and its control unit and a 4 Mpx FlowSense EO CCD camera (Dantec Dynamics) mounted on a Leica DM ILM inverted microscope (Leica Microsystems). The camera's matrix size is  $7.4\ \mu\text{m}$ , resulting in a  $1.5\ \text{mm} \times 1.6\ \text{mm}$  field-of-view with 10X magnification. The laser and camera are synchronised to operate at a frequency of 15 Hz. Time-averaged results are obtained by averaging 220 images.



**Fig. 6**  $\mu$ PIV system scheme

The fluorescent particle excitation light wavelength is  $532 \text{ nm}$ . The illuminated laser light is reflected by a dichroic mirror into a microchannel containing the tracer particles. The tracer particles emit light, which is filtered by the dichroic mirror and recorded by the camera. The dichroic mirror allowed all light from one side and only light with  $575 \text{ nm}$  wavelength from the other side, thereby filtering out any disruptive reflections. Finally, the images are obtained using the camera.

### 2.2.3. Image analysis

DynamicStudio v6.11 software (Dantec Dynamics) is employed to analyse the acquired images. Firstly, the image is filtered from all the unnecessary noise coming from various reflections by using the image arithmetic method. Then, the adaptive Particle Image Velocimetry technique is used to determine the velocity vectors based on the particle image pairs. This method utilises a grid of interrogation areas to track the travel distance of the seeding particles for velocity calculation. The principal scheme of PIV image processing is given in Fig. 7. The size and spacing of the interrogation areas are determined manually, corresponding to a specified number of pixels from one area to the next. The particle image fields are divided into interrogation regions of a specific size where the cross-correlation function is calculated to determine the most probable local displacement of tracer particles. Additionally, the interrogation areas are allowed to overlap if the spacing between neighbouring vectors is less than the size of the interrogation area. In this work, the adjacent tiles overlapped by 25% of the area, resulting in a  $25 \text{ }\mu\text{m}$  spacing between the  $x$ -axis velocity vectors and a  $20 \text{ }\mu\text{m}$  spacing between the  $y$ -axis velocity vectors.

Finally, as a result, a velocity vector field is obtained that can be used to analyse the flow further by calculating velocity streamlines, measuring velocity plots, etc.

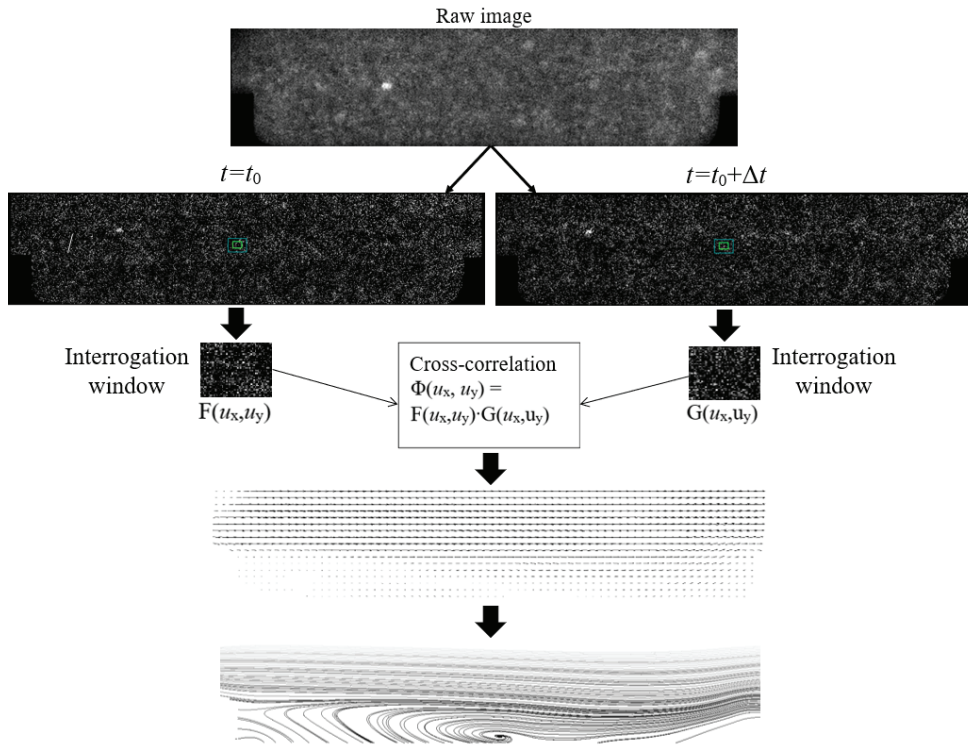
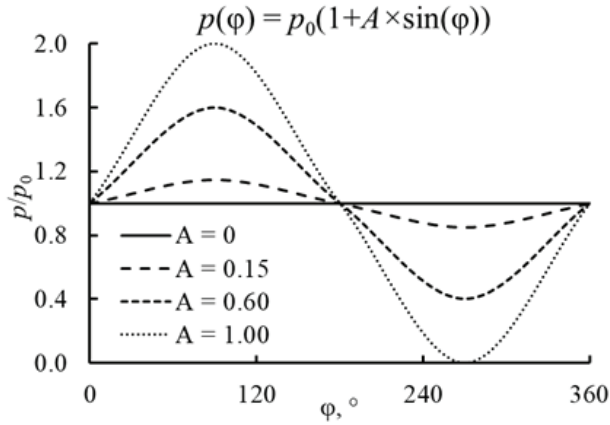


Fig. 7 Principal scheme of PIV image processing

#### 2.2.4. Stationary and pulsatile inlet conditions

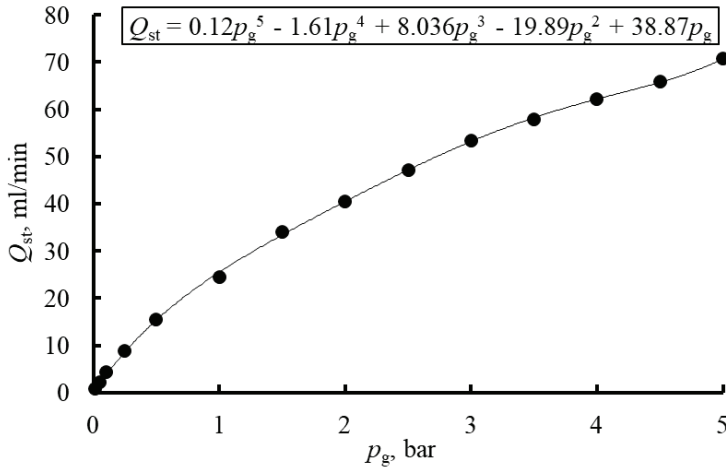
Stationary and pulsatile inlet conditions were generated using the pressure control unit and a high-pressure reservoir. Pressurised nitrogen was directed from the gas tank to the reservoir, thus creating the differential pressure required for fluid to flow into the experimental channel. The necessary pressure for a particular Re was ensured with the use of a pressure control unit. Additionally, using a programmable pressure control unit, the pressure in the reservoir was set to vary in sinusoidal pulses, thus generating the pulsatile inlet flow conditions Fig. 8.



**Fig. 8** Variation of pressure during the pulsation cycle with different pulsation amplitudes

### 2.2.5. Reynolds number calculations

Since two experimental facilities are employed in this work, the characteristic length and velocity measurement methods used in Re calculations differed. In the case of  $\mu$ PIV, the pressure control unit is used; therefore, the volumetric flow rate dependency on inlet gauge pressure needs to be obtained (Fig. 9).



**Fig. 9** Volumetric flow rate calibration curve

The obtained standard volumetric flow curve is recalculated at  $T_C = 0\text{ }^\circ\text{C}$ ; thus, later allowing to take ambient temperature into account when calculating Re:

$$Q_{st} = Q \times \frac{273.15}{273.15 + T_{ambient}\text{ }^\circ\text{C}}; \quad (1)$$



Inlet flow velocity  $u$  is then calculated from the obtained volumetric flow:

$$u = \frac{Q}{S}; \quad (2)$$

where  $S$  is inlet cross section area.

Re is calculated as follows:

$$Re = \frac{u \times L_{ch}}{\nu}; \quad (3)$$

where  $\nu$  is kinematic viscosity at ambient temperature, and  $L_{ch}$  is the characteristic length, which is either  $h_1$  or  $D_h$ , depending on the experimental facility.

During experiments with the PIV facility, the velocity was measured inside the inlet section with a thermo-anemometer, and Re was calculated by taking hydraulic diameter as a characteristic linear dimension due to the specific geometry of the experimental channel. However, during experiments with the  $\mu$ PIV facility, Re was calculated using step height ( $h_1$ ) as a characteristic length.

### 2.2.6. The uncertainty of flow rate and velocity calculations

The expanded volumetric flow rate measurement uncertainty is estimated by using the weighing method used for volume calibration, which can be mathematically expressed as:

$$V_0 = \frac{m}{\rho_w - \rho_a} \left( 1 - \frac{\rho_a}{\rho_s} \right) + \Delta V_g + \Delta V_r; \quad (4)$$

where  $m$  – weighed water mass;  $\rho_w$  – water density;  $\rho_a$  – air density;  $\rho_s$  – weight density;  $\Delta V_g$  – water evaporation losses;  $\Delta V_r$  – measurement repeatability.

The analysis of separate uncertainty components has shown that their value is mainly determined by the repeatability of measurement results. The uncertainty components of the weighing scale and density evaluation and time measurements are relatively small; therefore, the expanded uncertainty is directly evaluated by addressing the uncertainty coming from volume measurement:

$$\Delta Q = \left( \frac{V}{t} \right) \sqrt{\left( \frac{V_0}{V} \right)^2 + \left( \frac{\Delta t}{t} \right)^2}; \quad (5)$$

It is worth mentioning that the relative uncertainty values of volumetric flow rate measurements can be marginally reduced by increasing the volume of passing through water and measurement number; therefore, the relative uncertainty of the flow rate measurement is no more than 2%.

The uncertainty of velocity measurements was determined by assessing the contribution of expanded uncertainty of flow rate, channel cross-section dimensions and the uncertainty of velocity measurement repeatability. It can be mathematically expressed as follows:

$$Un_v^2 = Un_Q^2 \left( \frac{\partial u}{\partial Q} \frac{1}{A} \right)^2 + Un_A^2 \left( \frac{\partial u}{\partial A} \frac{1}{A^2} Q \right)^2; \quad (6)$$

where  $Un$  is the standard uncertainty of velocity ( $u$ ), flow rate ( $Q$ ) and cross section area ( $A$ ). The uncertainty analysis reveals that the expanded uncertainty of velocity measurement by both PIV and  $\mu$ PIV does not exceed 7 %.

### 2.2.7. The uncertainty of recirculation zone length measurements

The recirculation zone length is measured by the minimum  $u_{x,rms}$  value at the lowest possible  $y$  position. This method suggests that the separated shear layer is reattached when the velocity vectors change direction. The precise measurement of recirculation zone length is difficult due to several reasons. The first one is limited resolution. The limitations come from the comparatively large scale of the channel and the exact reattachment point location, which happens in a single resolution window. The second reason is that, in some cases, the whole velocity field is obtained by connecting a few velocity vector fields, and the precise connection cannot be guaranteed. The third reason is the complexity of fluid flow in transitional and turbulent flow regime, when the vortex shedding is observed. It strongly affects the location of the separated layer reattachment point. Each of these three reasons brings a significant component to the measurement uncertainty.

Since the separated shear layer reattachment point fluctuates, the repeatability of measurements is addressed by measuring the recirculation zone length at each timestep. In the laminar flow regime, the recirculation zone length remains constant, and the repeatability is less than 2.3%. In turbulent flow regime, the reattachment point fluctuations increase and the repeatability decreases to 8.9%. The expanded uncertainty of recirculation zone length measurements is less than 15%.

### 2.2.8. Turbulence intensity and phase velocity calculations in pulsatile flow

The method for calculating turbulence intensity described below is also presented in the publication<sup>1</sup>.

Due to the pulsating nature of the inlet, flow inside the measurement area pulsates with the period  $T = 1/f$ . Measurements were made with time step  $\Delta t = 0.067s$ . The number of snapshots was  $N = 180$  or  $210$ , depending on pulsation frequency, the number of snapshots during one period  $n = T/\Delta t$ . The number of pulsation periods during all measurement times is  $N_T = N/n$ .

In order to estimate the turbulent properties of the flow, we should separate the mean phase flow and fluctuations. The mean phase flow velocity is characterised by periodicity in every period of pulsation:

---

<sup>1</sup>Šereika J., Vilkinis P., Skarbalius G., Džiugys A., Pedišius N. Experimental analysis of pulsatile flow effects on flow structure in transitional-type cavity. *Experimental Thermal and Fluid Science*. New York: Elsevier, 2024, Vol. 151, 111073, p. 1-10. ISSN 0894-1777.

$$\bar{u}(\tau + kT) = \bar{u}(\tau), k = [0, N_T - 1], \quad (7)$$

Accordingly, measured velocity in each point at each measurement time can be separated into the components of pulsating (mean phase flow) velocity  $\bar{u}$  and fluctuating velocity  $u'$ :

$$u(t_i) = \bar{u}(t_i) + u'(t_i), \quad (8)$$

where  $i$  is the time index of measurement:

$$t_i = i\Delta t, i = [0, N - 1], \quad (9)$$

and the mean phase flow velocity is estimated as follows:

$$\bar{u}(\tau_j) = \frac{\sum_{i=0}^{N-1} u(t_i) \delta(\tau_j, \text{mod}(t_i, T))}{\sum_{i=0}^{N-1} \delta(\tau_j, \text{mod}(t_i, T))}, \tau_j = j\Delta t, j = [0, n]. \quad (10)$$

Additionally, outlier velocity points were removed from temporal data at a confidence interval of 95% from mean phase velocity. The average velocity of the mean phase flow velocity is estimated as follows:

$$\langle \bar{u} \rangle = \frac{1}{n} \sum_{j=0}^n \bar{u}(\tau_j), \tau_j = j\Delta t, j = [0, n], \quad (11)$$

Turbulent energy  $TKE$  at each phase time is estimated as follows:

$$TKE(\tau_j) = \frac{3 \sum_{i=0}^{N-1} (u'_x(t_i)^2 + u'_y(t_i)^2) \delta(\tau_j, \text{mod}(t_i, T))}{4 \sum_{i=0}^{N-1} \delta(\tau_j, \text{mod}(t_i, T))}, \tau_j = j\Delta t, j = [0, n], \quad (12)$$

Finally, turbulent intensity  $TI$  is estimated as follows:

$$TI(\tau_j) = \frac{U'(\tau_j)}{U} = \frac{\sqrt{\frac{2}{3} TKE(\tau_j)}}{U}, \tau_j = j\Delta t, j = [0, n]. \quad (13)$$

Averaged turbulent intensity is defined as:

$$\langle TI \rangle = \frac{1}{n} \sum_{j=0}^n TI(\tau_j), \tau_j = j\Delta t, j = [0, n] \quad (14)$$

### 2.3. Numerical simulation

To expand research capabilities, CFD was employed. CFD allows to perform analysis beyond the capabilities of experimental setup. Numerical simulations were performed using commercially available *Ansys Fluent* 2019 R2 software based on FVM.

Numerical simulations are conducted by solving Navier-Stokes equations, which describe the motion of viscous fluid substances, express momentum balance and conservation of mass for Newtonian fluids:

$$\left. \begin{aligned} \frac{Du_x}{dt} &= a_x - \frac{1}{\rho} \frac{\partial p}{\partial x} + \nu \nabla^2 u_x \\ \frac{Du_y}{dt} &= a_y - \frac{1}{\rho} \frac{\partial p}{\partial y} + \nu \nabla^2 u_y \\ \frac{Du_z}{dt} &= a_z - \frac{1}{\rho} \frac{\partial p}{\partial z} + \nu \nabla^2 u_z \end{aligned} \right\} \quad (15)$$

where  $\nabla^2 = \frac{\partial^2}{\partial x^2} + \frac{\partial^2}{\partial y^2} + \frac{\partial^2}{\partial z^2}$ ;  $\nu = \frac{\mu}{\rho}$ ;  $a$  – acceleration induced by external forces.

These equations can be described in vectorial form:

$$\frac{D\vec{u}}{dt} = a - \frac{1}{\rho} \text{grad } p + \nu \nabla^2 \vec{u} \quad (16)$$

Since the equation has 6 unknown variables, the fluid continuum and momentum equations are used for the solution. Assuming conservation of mass, the continuum equation for compressible is expressed as follows:

$$\frac{\partial p}{\partial t} + \nabla \cdot \rho u(x, y, z, t) = 0 \quad (17)$$

where  $\nabla = \frac{\partial}{\partial x} + \frac{\partial}{\partial y} + \frac{\partial}{\partial z}$

If the fluid is incompressible, the continuum equation is simplified:

$$\nabla \cdot u(x, y, z, t) = 0 \quad (18)$$

The differential momentum equation for incompressible fluid can be described as follows:

$$\rho \frac{Du_x}{Dt} = - \frac{\partial p}{\partial x} - \mu \left( \frac{\partial^2 u_x}{\partial x^2} + \frac{\partial^2 u_y}{\partial y^2} + \frac{\partial^2 u_z}{\partial z^2} \right) + \rho a_x; \quad (19)$$

$$\rho \frac{Du_y}{Dt} = - \frac{\partial p}{\partial y} - \mu \left( \frac{\partial^2 u_x}{\partial x^2} + \frac{\partial^2 u_y}{\partial y^2} + \frac{\partial^2 u_z}{\partial z^2} \right) + \rho a_y; \quad (20)$$

$$\rho \frac{Du_z}{Dt} = - \frac{\partial p}{\partial z} - \mu \left( \frac{\partial^2 u_x}{\partial x^2} + \frac{\partial^2 u_y}{\partial y^2} + \frac{\partial^2 u_z}{\partial z^2} \right) + \rho a_z; \quad (21)$$

### 2.3.1. Reynolds averaged Navier-Stokes equations

One of the most common ways to solve Navier-Stokes equations is by using the Reynolds-averaged Navier-Stokes (RANS) method, which offers a low computational cost yet still moderately accurate results and acceptable uncertainty, which is constantly being reduced due to consistent model development (Xiao et al., 2019). Furthermore, depending on the research purposes, the RANS approach can satisfy with enough information such as mean velocities, mean pressures, mean stresses etc. (H K Versteeg, 2007).

For the derivation of RANS equations from the instantaneous Navier-Stokes equations, the separation of the flow velocity into mean and fluctuating velocity components is required:

$$u(x, y, z, t) = \bar{u}(x, y, z) + u'(x, y, z, t) \quad (22)$$

where  $\bar{u}$  – mean (time-averaged) velocity component,  $u'$  - fluctuating velocity component.

Since mean flow velocity and fluctuating flow velocity components satisfy the continuum condition, the flow equations can be described:

$$\rho \frac{D\bar{u}_x}{Dt} = -\frac{\partial \bar{p}}{\partial x} + \frac{\partial}{\partial x} \left( \mu \frac{\partial \bar{u}_x}{\partial x} - \rho \overline{u'^2_x} \right) + \frac{\partial}{\partial y} \left( \mu \frac{\partial \bar{u}_x}{\partial y} - \rho \overline{u'_x u'_y} \right) + \frac{\partial}{\partial z} \left( \mu \frac{\partial \bar{u}_x}{\partial z} - \rho \overline{u'_x u'_z} \right); \quad (23)$$

$$\rho \frac{D\bar{u}_y}{Dt} = -\frac{\partial \bar{p}}{\partial y} + \frac{\partial}{\partial x} \left( \mu \frac{\partial \bar{u}_y}{\partial x} - \rho \overline{u'_x u'_z} \right) + \frac{\partial}{\partial y} \left( \mu \frac{\partial \bar{u}_y}{\partial y} - \rho \overline{u'^2_y} \right) + \frac{\partial}{\partial z} \left( \mu \frac{\partial \bar{u}_y}{\partial z} - \rho \overline{u'_z u'_y} \right); \quad (24)$$

$$\rho \frac{D\bar{u}_z}{Dt} = -\frac{\partial \bar{p}}{\partial z} + \frac{\partial}{\partial x} \left( \mu \frac{\partial \bar{u}_z}{\partial x} - \rho \overline{u'_z u'_x} \right) + \frac{\partial}{\partial y} \left( \mu \frac{\partial \bar{u}_z}{\partial y} - \rho \overline{u'_y u'_z} \right) + \frac{\partial}{\partial z} \left( \mu \frac{\partial \bar{u}_z}{\partial z} - \rho \overline{u'^2_z} \right); \quad (25)$$

These equations can be described in common form as follows:

$$\rho \left( \frac{\partial \bar{u}_i}{\partial t} + \bar{u}_j \frac{\partial \bar{u}_i}{\partial x_j} \right) = -\frac{\partial \bar{p}}{\partial x_i} + \frac{\partial}{\partial x_j} \left( \mu \frac{\partial \bar{u}_i}{\partial x_j} - \rho \overline{u'_i u'_j} \right); \quad (26)$$

One of the most common ways to simulate mean flow characteristics is by using the standard  $k$ - $\epsilon$  turbulence model, which consists of two equations as follows:

$$\frac{\partial(\rho k)}{\partial t} + \frac{\partial(\rho k u)}{\partial x} = \frac{\partial}{\partial x} \left[ \left( \mu + \frac{\mu_\tau}{\sigma_k} \right) \frac{\partial k}{\partial x} \right] + G_k + G_b - \rho \varepsilon - Y_m + S_k \quad (27)$$

$$\frac{\partial(\rho \varepsilon)}{\partial t} + \frac{\partial(\rho \varepsilon u)}{\partial x} = \frac{\partial}{\partial x} \left[ \left( \mu + \frac{\mu_\tau}{\sigma_\varepsilon} \right) \frac{\partial \varepsilon}{\partial x} \right] + C_{1\varepsilon} \frac{\varepsilon}{k} (G_k + C_{3\varepsilon} G_b) - C_{2\varepsilon} \rho \frac{\varepsilon^2}{k} + S_\varepsilon \quad (28)$$

The (26) and (27) equations correspond to kinetic energy  $k$  and dissipation  $\varepsilon$  equations, respectively, where  $G_k$  and  $G_b$  – the generation of turbulence kinetic energy due to the mean velocity gradient and buoyancy, respectively;  $Y_m$  – contribution of the fluctuating dilatation in compressible turbulence to the overall dissipation rate,  $S_k$  and  $S_\varepsilon$  – user defined source terms,  $\sigma_k$ ,  $\sigma_\varepsilon$  – Prandtl numbers for  $k$  and  $\varepsilon$ ;  $C_{1\varepsilon}$ ,  $C_{2\varepsilon}$ ,  $C_{3\varepsilon}$  are adjustable constants. The constant values of adjustable constants were used:  $C_{1\varepsilon} = 1.44$ ;  $C_{2\varepsilon} = 1.92$ ;  $\sigma_k = 1$ ;  $\sigma_\varepsilon = 1.3$ . The constant  $C_{3\varepsilon}$  determines the degree to which  $\varepsilon$  is affected by the buoyancy. In *Fluent*  $C_{3\varepsilon}$  is calculated from a relation  $C_{3\varepsilon} = \tanh \left| \frac{v}{u} \right|$ . In this work, the  $k$ - $\varepsilon$  standard model was used for the impact of geometrical parameters on the flow structure in an open-type cavity at  $Re_{Dh} = 1000$ , while the laminar model was used in the range of  $Re_{Dh} = 10 - 100$ .

Additionally, for the flow simulations in a closed-type cavity, the Reynolds stress-omega model was employed, which involves the calculation of separate stresses  $\frac{\partial(\rho u'_i u'_j)}{\partial t}$  by using differential transport equations:

$$\frac{\partial(\rho u'_i u'_j)}{\partial t} = D_{Tij} + D_{Lij} + P_{ij} + \Pi_{ij} + \Omega_{ij} - \varepsilon_{ij} \quad (29)$$

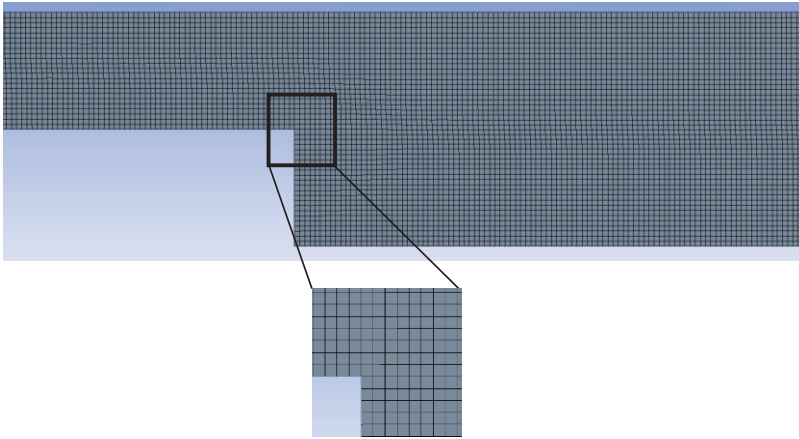
$D_{Tij}$ ,  $D_{Lij}$  – turbulent and molecular diffusion;  $P_{ij}$  – stress production;  $\Pi_{ij}$  – deformations caused by pressure and velocity gradients;  $\Omega_{ij}$  – stresses caused by rotational flow;  $\varepsilon_{ij}$  – dissipation of turbulent energy.

RANS models have been the primary method for simulating flow characteristics for the last few decades due to their less costly computing requirement and affordable use compared to LES and DNS methods (Yusof et al., 2020). However, while RANS is ideal for the mean characteristics of the flow, it is limited when the flow is pulsatile or unsteady. In pulsatile flow cases, unsteady RANS (URANS) was applied for a more accurate analysis of time-dependent flow. URANS allows the achievement of results within a reasonable computation time and can be effectively employed when the comparison with experimental results is possible (Hillewaere et al., 2012).

### 2.3.2. Meshing

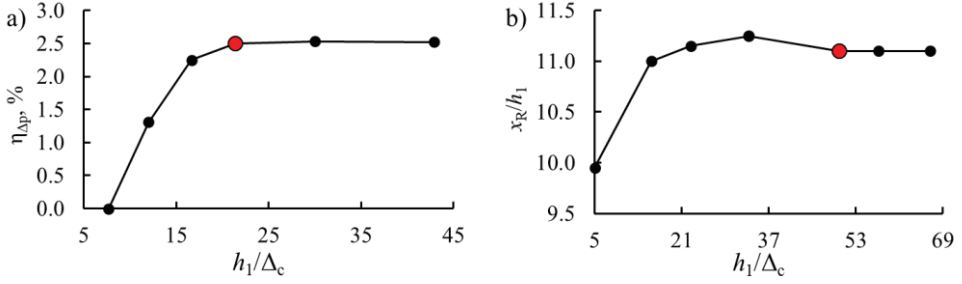
Meshing is a crucial step in CFD simulations. It involves dividing the computational domain into smaller, finite-sized elements, i.e., cells, each associated with a set of variables that represent the fluid properties, such as velocity, pressure, temperature, etc. In *Ansys Fluent*, meshing is performed mainly using 3 techniques: structured, unstructured, and hybrid. Structured meshes are composed of rectangular

or curvilinear cells arranged in a regular grid, while unstructured meshes are composed of irregularly shaped cells generated using automated meshing algorithms. An example of a structured mesh is given in Fig. 10. It is worth mentioning that the grid given in Fig. 10 is purposely coarse for a convenient representation. Hybrid meshes combine elements from both structured and unstructured meshes, offering a compromise between accuracy and computational efficiency. In this work, for both 2D and 3D simulations, a structured meshing method was employed; therefore, the mesh grids consisted of rectangular cells in 2D computational domains and hexahedrons in 3D ones.



**Fig. 10** Representation of a structured mesh in a 2D closed-type cavity

A fine mesh is required to provide accurate simulations, which significantly increases the computational cost. To avoid this problem, a grid independence test is necessary. It is usually performed by monitoring a parameter of choice, for instance, pressure, temperature or, as in the present case – the total pressure difference (Fig. 11a) and the recirculation zone length (Fig. 11b). In channels with sudden cross-sectional changes recirculation zone length is a crucial parameter which defines the flow structure. Grid independence is ensured by computing several different grids with increasing the number of grid elements. As the element number increases, the length of the recirculation zone changes its size until it becomes independent of the element size; therefore, to perform economic calculations, the grid is chosen exactly at the mesh size, which shows very little to no dependency on the monitoring parameter (Fig. 11). In simulations within a 3D open-type cavity, the step height and cell size ratio were  $h_1/\Delta_c \approx 21$ , whereas in the 2D closed-type cavity –  $h_1/\Delta_c \approx 51$ . The exact number of cells in open-type and closed-type cavities were  $5 \times 10^5$  and  $2 \times 10^5$ , respectively.



**Fig. 11** Mesh independency test in a) open-type cavity, b) closed-type cavity

In the present work, the pressure-based solver is used. It works by first solving a set of equations for the pressure field, which are derived from the continuity equation and the momentum equations. These equations are solved using the iterative SIMPLE (Semi-Implicit Method for Pressure-Linked Equations) method, which applies corrections to the pressure field. Additionally, a second-order upwind scheme was applied to discretise the momentum equation. The simulations were performed with a convergence criterion of at least  $10^{-6}$  for continuity.

### 2.3.3. Boundary conditions

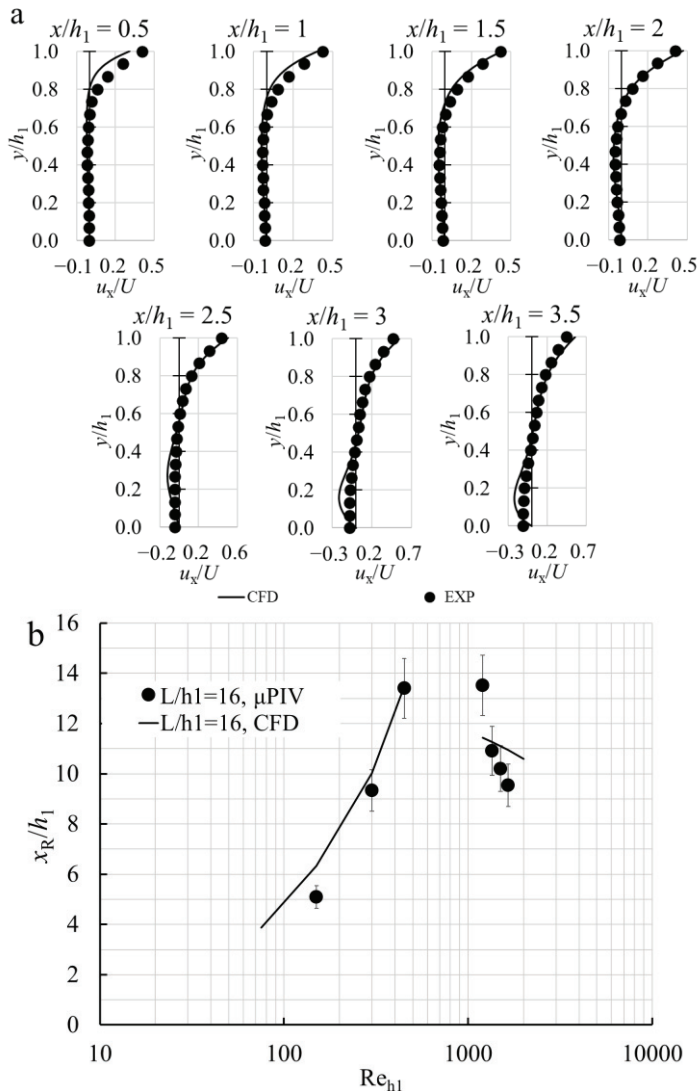
During numerical simulations, the working fluid was water with a constant density of  $\rho = 998.2 \text{ kg/m}^3$  and a constant dynamic viscosity of  $1.003 \cdot 10^{-3} \text{ kg/(m}\cdot\text{s)}$ . In stationary flow cases, a flat velocity profile was set with its value ranging from  $u = 0.0223 \text{ m/s}$  (at  $Re_{Dh} = 10$ ) to  $u = 2.23 \text{ m/s}$  (at  $Re_{Dh} = 1000$ ) in an open-type cavity. In a closed-type cavity the velocity ranged from  $u = 0.25 \text{ m/s}$  (at  $Re_{h1} = 50$ ) to  $u = 10 \text{ m/s}$  (at  $Re_{h1} = 2000$ ). In both cavity cases, the turbulence intensity at the inlet was set to 5 %, and the initial gauge pressure was set to 0. At the outlet, the gauge pressure was set to 0 in all the simulated cases. To simulate the pulsatile flow in a closed-type cavity, a user defined function was created, which allowed the inlet velocity to vary in sinusoidal pulses during transient simulations. The velocity, though still with a flat profile, varied from 0 to  $2 \cdot u_{max}$  creating a pulsation amplitude of  $A = 1$ .

## 2.4. Comparison between results of experiments and numerical simulations

Combining both experimental and numerical approaches improves the study's accuracy and reliability due to the possibility of comparison of experimental and numerical results and allows the range of investigated properties to be extended. A comparison with experimental results is necessary to ensure the validity of numerically obtained results. The present comparisons are conducted by comparing the experimental and numerical results of this work and are based on two parameters – velocity distribution and recirculation zone length dependency on  $Re$ . The comparisons of different simulations are given in Fig. 12. Both comparisons show acceptable agreement. When investigating the flow separation phenomenon in



channels with sudden expansion and contraction, the recirculation zone length can be used as a compared parameter. If the reattachment of the separated shear layer is absent – velocity is used instead; therefore, in the open-type cavity, numerically and experimentally obtained flow velocity distribution results are compared (Fig. 12a), while the recirculation zone length dependency on  $Re$  is compared in a closed-type cavity (Fig. 12b). Even though in a closed-type cavity the relative recirculation zone length values differ considerably at  $Re_{h1} = 1000 - 1750$ , the regularities of recirculation zone dynamics in a closed-type cavity coincide almost perfectly, therefore, the agreement between experimental and numerical results are acceptable.



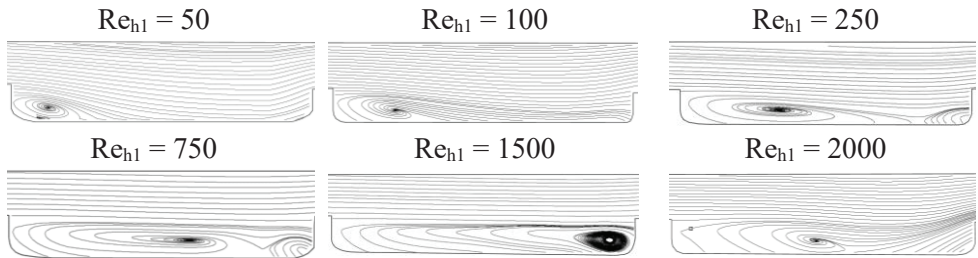
**Fig. 12** Comparisons of numerically and experimentally obtained results in a) open-type cavity at  $Re_{Dh} = 1000$ ; b) closed-type cavity

### 3. RESULTS AND DISCUSSION

In this section, all experimentally and numerically obtained results are given, analysed, and discussed. This section will be divided into two main subsections regarding active and passive flow control methods. The active flow control technique corresponds to controlling the flow by varying the pulsation parameters while investigating the vortex development and recirculation zone length dynamics and monitoring statistical flow parameters such as shear rate, turbulence intensity, and vorticity distribution. Passive flow control methods correspond to introducing different configurations of roughness elements installed on the bottom of the channel, thus confining the recirculation zone from achieving large volumes while simultaneously investigating velocity and shear rate distribution with the addition of pressure loss analysis. Additionally, the impact of geometrical cavity parameters is analysed by studying the influence of rounded cavity inner corners and inlet/outlet diameter ratio on velocity distribution inside of a cavity.

#### 3.1. Recirculation zone dynamics of stationary flow in cavities

The experimentally obtained time-averaged velocity streamlines of the flow in a transitional-type cavity at various  $Re_{h1}$  are presented to visualise the dynamics of the recirculation zone in the cavity based on the flow regime (Fig. 13).

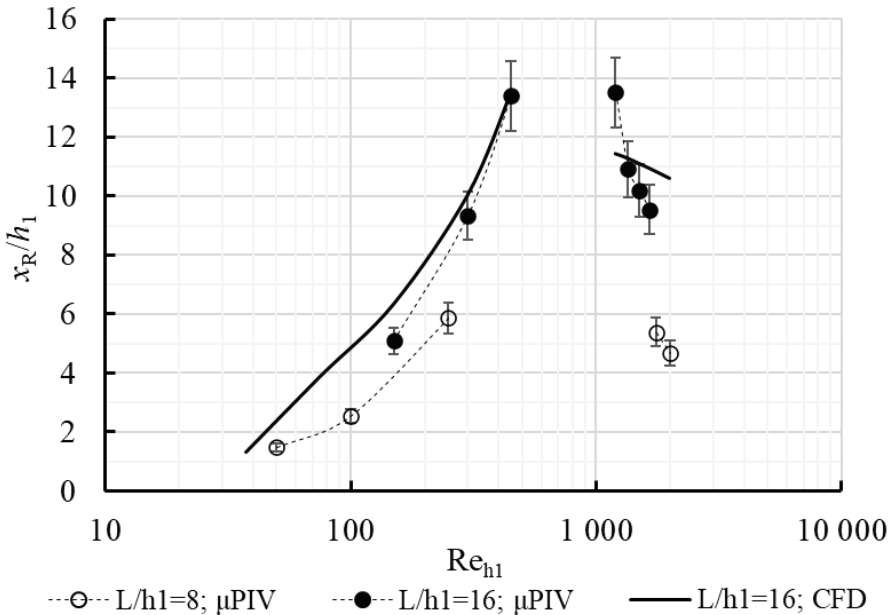


**Fig. 13** Stationary flow streamlines in a transitional-type cavity ( $L/h_1 = 8$ )

In the laminar flow regime, at  $Re_{h1} = 50 - 100$ , the flow separation occurs due to an adverse pressure gradient which is caused by the sudden cross-sectional changes of the channel (Armaly et al., 1983). The recirculation zone is formed behind the BFS, and the separated shear layer is reattached to the bottom of the cavity. The recirculation zone is known to be steady during the laminar flow regime. The recirculation zone growth rate is strongly dependent on  $Re_{h1}$  when the flow is laminar, as its length increases with increasing  $Re_{h1}$  nearly linearly. After the recirculation zone reaches its maximum length (in the present case at  $Re_{h1} \approx 250$ ), the transitional flow regime begins, and the separated shear layer is not reattached to the bottom of the cavity; therefore, the whole cavity is then filled with a recirculation zone. Experiments in a transitional-type cavity show that reattachment of the separated shear layer reoccurs only at  $Re_{h1} = 1750$  (Fig. 14). When the flow enters a turbulent flow regime,

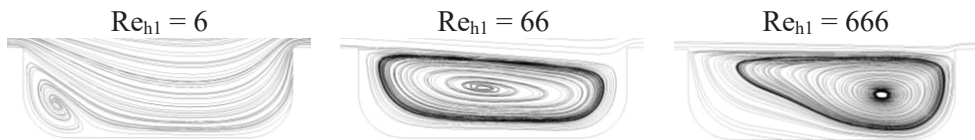
it is expected for the relative recirculation zone length to reach its asymptotical value, where it no longer depends on  $Re$  (Armaly et al., 1983).

Even though the relative recirculation zone length values differ considerably, the regularities of recirculation zone dynamics in transitional- and closed-type cavities coincide almost perfectly, the main difference being the  $Re_{h1}$  range of when the flow is detached from the bottom of the channel (Fig. 14). In laminar flow conditions, the length of the recirculation zone is governed by the expansion of the shear layer, which forms due to the interaction between the primary flow and the recirculating flow. (Vilkinis et al., 2020). The flow reattachment absence is observed in the  $Re_{h1}$  range of  $450 < Re_{h1} < 1200$  in a closed-type cavity and  $250 < Re_{h1} < 1750$  in a transitional-type cavity. The  $Re_{h1}$  range, where the separated shear layer is not reattached on the cavity bottom, is wider due to the confinement of closer located FFS in the transitional-type cavity. In a closed-type cavity, further located FFS allows the recirculation zone to elongate more with increasing  $Re_{h1}$ . As a result, the transitional flow regime begins later compared to transitional-type cavity, indicating that a higher adverse pressure gradient is necessary to achieve it. As  $Re_{h1}$  increases further, the length of the recirculation zone begins to decrease, and reattachment of the separated flow is observed once more. The transitional flow regime introduces instabilities in the shear layer, which influence the internal structure of the recirculation zone, resulting in its shortened length.



**Fig. 14** Recirculation zone length dependency on  $Re_{h1}$  in transitional- and closed-type cavity with  $L/h_1 = 8$  and  $L/h_1 = 16$ , respectively

Fig. 15 represents the numerically simulated flow in an open-type cavity. Different regularities of recirculation zone dynamics are observed in an open-type cavity, compared to transitional- and closed-type cavities. At low  $Re$ , when the flow is laminar, if the pressure gradient is sufficient, the flow separation occurs induced by abrupt cross-sectional changes. The size and shape of the recirculation zone depend on various parameters, including the geometry of the step and  $Re$ . In a laminar flow regime, the recirculation zone is expected to have a steady behaviour, where the velocity distribution inside of the cavity remains constant over time. As  $Re$  increases, the recirculation zone fills the whole cavity and the separated shear layer bridges over it (At  $Re_{hl} = 66$ ). As  $Re_{hl}$  increases further, the recirculation zone core is shifted towards the FFS. At that point, the structure of the flow becomes independent on  $Re$ , similar as is transitional- and closed-type cavities.



**Fig. 15** Numerically obtained flow velocity streamlines in an open-type cavity ( $L/h_1 = 4$ )

### 3.2. Active flow control

The results and analysis presented in sections 3.2.1 – 3.2.3, as well as in all their subsections, are also presented in the publication<sup>2</sup>.

The dynamics of the recirculation zone in transitional- and closed-type cavities were analyzed across various  $Re_{hl}$  values and different pulsatile flow parameter scenarios to assess the individual impacts of pulsation amplitude and frequency. Table 2 presents the pulsation amplitude and frequency values for the different flow cases. Case 1 corresponds to the stationary flow condition; hence its pulsation amplitude and frequency are not specified. Three pulsation amplitudes were explicitly chosen to cover the entire range from low amplitude of  $A = 0.15$  to maximum amplitude of  $A = 1.0$ , where  $A = 0.60$  would serve as an intermediate value. Additionally, pulsation frequencies of  $f = 0.5; 1; 2; 5$  Hz were chosen, where  $f = 0.5$  and 1 Hz correspond to slower pulsations that are proved to have the most significant effect on flow structure (Tihon et al., 2012), while high frequencies, such as  $f = 2$  and 5 Hz represent more rapid pulsations, enabling the investigation of recirculation zone response to faster

<sup>2</sup> Šreika J., Vilkinis P., Skarbalius G., Džiugys A., Pedišius N. Experimental analysis of pulsatile flow effects on flow structure in transitional-type cavity. *Experimental Thermal and Fluid Science*. New York: Elsevier, 2024, Vol. 151, 111073, p. 1-10. ISSN 0894-1777.

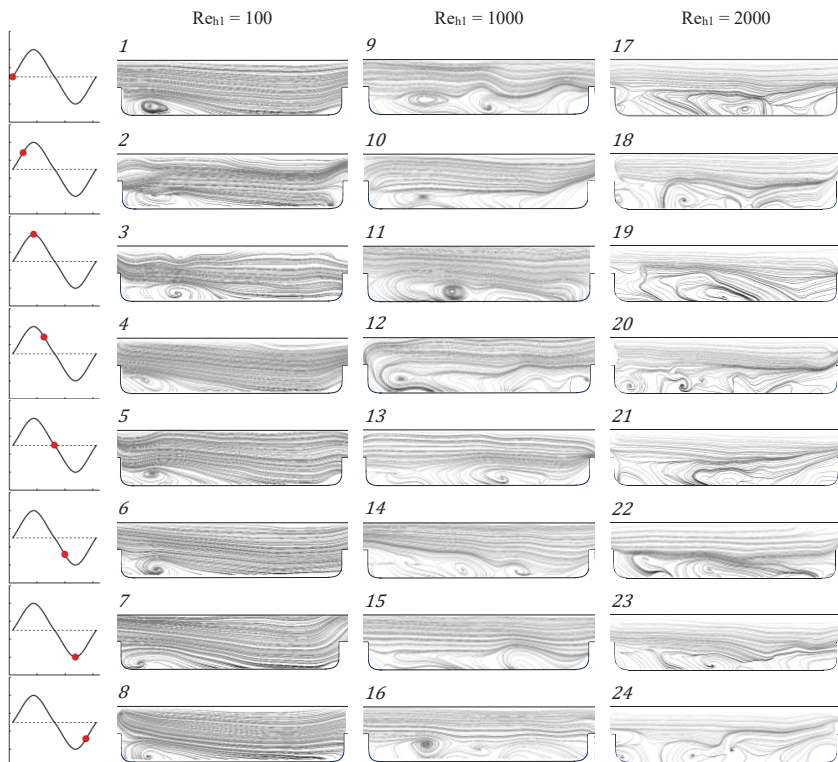
changes in the flow structure. The present section is divided into three subsections where the influence of  $Re$ ,  $A$  and  $f$  is highlighted and discussed separately.

**Table 2** Amplitude and pulsation frequency of different flow cases

Case	$A$	$f$ , Hz	$L/h_1$
1	-	-	8; 16
2	0.15	0.5	8
3	0.15	1.0	8
4	0.60	0.5	8
5	0.60	1.0	8
6	1.00	1.0	16
7	1.00	2.0	16
8	1.00	5.0	16

### 3.2.1. Recirculation zone behaviour during the pulsation cycle

During the pulsation cycle, the dynamics of the recirculation zone depend on the flow regime. Fig. 16 shows the experimentally obtained instantaneous flow velocity streamlines for different phases of the pulsation cycle.



**Fig. 16** Flow velocity streamline variation in transitional-type cavity ( $L/h_1 = 8$ ) during the pulsation cycle of  $A = 0.60$  and  $f = 0.5$  Hz

In the laminar flow regime (Fig. 16 (1-8)), the variation in velocity during the pulsation cycle influences the length of the recirculation zone, causing it to increase and decrease depending on the phase of the cycle since its dependency on  $Re$  in the laminar flow regime follows a linear relationship. Consequently, during the cycle, the recirculation zone length increases during the velocity acceleration phase (at  $0^\circ < \varphi < 90^\circ$  and  $270^\circ < \varphi < 360^\circ$ ) and decreases during the flow deceleration phase (at  $90^\circ < \varphi < 270^\circ$ ). Pulsatile flow causes the vortex centre to change its position, but the recirculation zone remains stagnant.

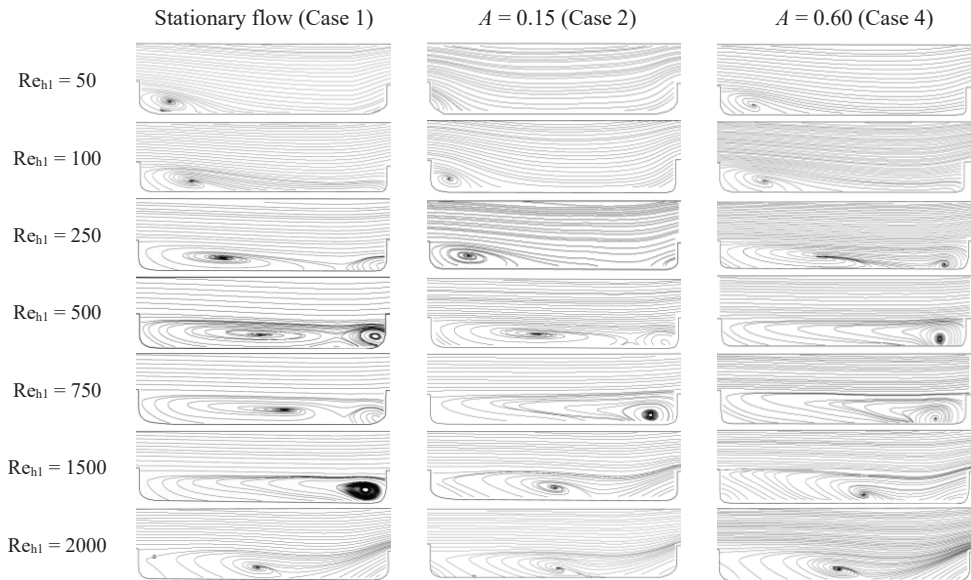
In the transitional flow regime (Fig. 16 (9-16)), a different mechanism governs the development of the recirculation zone. It is no longer stagnant and comprises periodically recurring vortices, as discussed by Vilkinis and Pedišius (Vilkinis et al., 2020). In Fig. 16 at  $Re_{hl} = 1000$ , these recurring vortices are observable throughout the pulsation cycle. During this process, a secondary vortex appears between the BFS and the primary vortex in the lower corner of the cavity, which, as time passes, grows and pushes the primary vortex downstream until the resulting stresses cause the primary vortex to escape from under the shear layer towards the outlet of the cavity. Therefore, during the transitional flow regime, at certain phases of the pulsation cycle, two detached vortices are observed in one frame (Fig. 16 (9 and 14-16)). The same mechanism applies at  $Re_{hl} = 2000$ , although more chaotic vortex movement is visible (Fig. 16 (16-24)). At certain pulsation phases, three vortex cores are observed (Fig. 16 (24)), indicating that the frequency of vortices shedding is higher than pulsatile flow at  $Re_{hl} = 1000$ .

The other investigated pulsatile flow cases show similar tendencies where the frequency of recurring vortices correlates with the pulsation parameters and determines the time-averaged recirculation zone length.

### 3.2.2. Pulsation amplitude impact on recirculation zone dynamics

Fig. 17 displays experimentally obtained flow patterns for cases with distinct amplitude values of  $A = 0.15$  and  $A = 0.60$  (Cases 2 and 4) since the impact of pulsation frequency on flow structure was negligible. At  $Re_{hl} = 50$ , small alterations occur on the length of the recirculation zone at  $A = 0.60$ ; however, its complete absence is observed with applied pulsations with  $A = 0.15$ . Recirculation zone length decreases during pulsatile flow at  $Re_{hl} = 100-250$ , and the increase in recirculation zone length with increasing  $Re_{hl}$  is evident, as it remains linear under laminar flow conditions. Additionally, the recirculation zone interacts with the vortex near the FFS in the transitional flow regime ( $Re_{hl} = 750$ ). Under pulsatile flow conditions, the interaction is more intense; therefore, the recirculation zone centre location shifted to the FFS earlier compared with the stationary flow case. This effect is achieved at  $Re_{hl} = 500$  with  $A = 0.60$ . At  $Re_{hl} = 1750 - 2000$ , the recirculation zone length no longer depends on pulsation parameters and an almost identical distribution of velocity streamlines is observed between investigated flow cases. This proves that in the turbulent flow

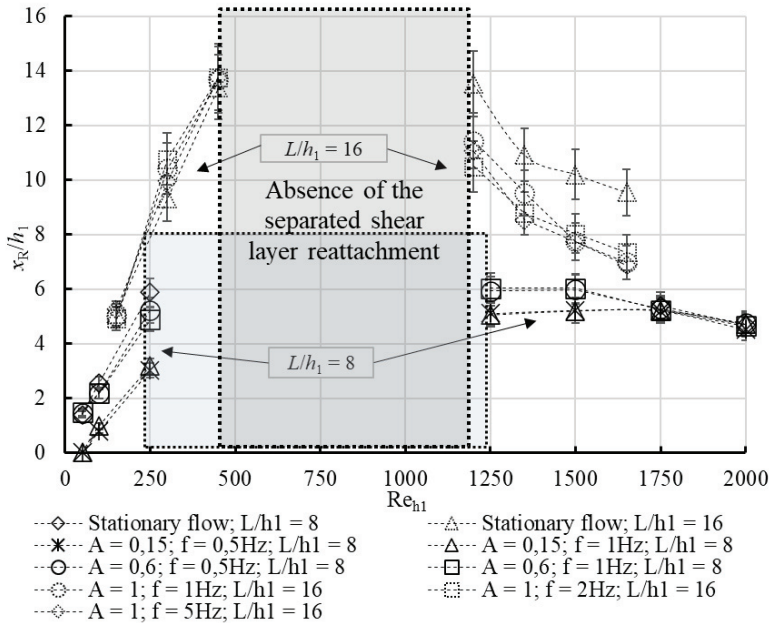
regime, the recirculation zone length reaches its asymptotic value, becoming independent of both  $Re$  and pulsatile flow parameters.



**Fig. 17** Time-averaged velocity streamlines in a transitional-type cavity at  $Re_{h1} = 50$ – $2000$  for stationary flow and pulsatile flow with  $A = 0.15$  and  $0.60$

The recirculation zone length dependencies on  $Re$  given in Fig. 18 are experimentally obtained using the same approach as in Fig. 17, where the flow is averaged throughout the whole measurement. The changes in the recirculation zone length depend on the pulsation amplitude. Lower recirculation zone length values are observed in pulsatile flow cases at  $Re = 50$ – $250$ , due to small vortices in the separated shear layer, which produces a higher rate of entrainment, thus causing the reduction of recirculation zone length (Chun et al., 1996). The recirculation zone length reduction at  $A = 0.15$  is determined based on the linear recirculation zone length growth in the laminar flow regime and the significant change in its structure in the transitional flow regime. When the pulsation amplitude is low ( $A = 0.15$ ), the flow remains primarily in the same flow regime, and changes in the recirculation zone size remain linear during the flow pulsation cycle. When the pulsation amplitude increases to  $A = 0.60$ , the velocity varies more significantly, and a transitional flow regime may be reached when the recirculation zone length increment during the acceleration phase is large. Therefore, time-averaged flow fields feature larger recirculation zone lengths in high-amplitude cases than in low-amplitude cases because the cavity is filled with a stagnant recirculation zone for a certain period. For the same reason, separated shear layer reattachment occurs at a lower  $Re_{h1}$  compared with the case of stationary flow ( $Re_{h1} = 1250$  at pulsatile flow and  $Re_{h1} = 1750$  at stationary flow), and

shorter recirculation zone length values are observed at the beginning of the turbulent flow regime in the pulsatile flow cases. The same trend is observed in a closed-type cavity, where the recirculation zone reduction effect is observed when  $Re_{h1} > 1200$ . However, the main difference between pulsatile flow effects in different types of cavities is observed in laminar flow, where pulsations with  $A = 1$  show little to no effect on recirculation zone length. In a closed-type cavity, the discrepancies in recirculation zone length in the laminar flow regime are marginal and do not exceed the measurement uncertainty.

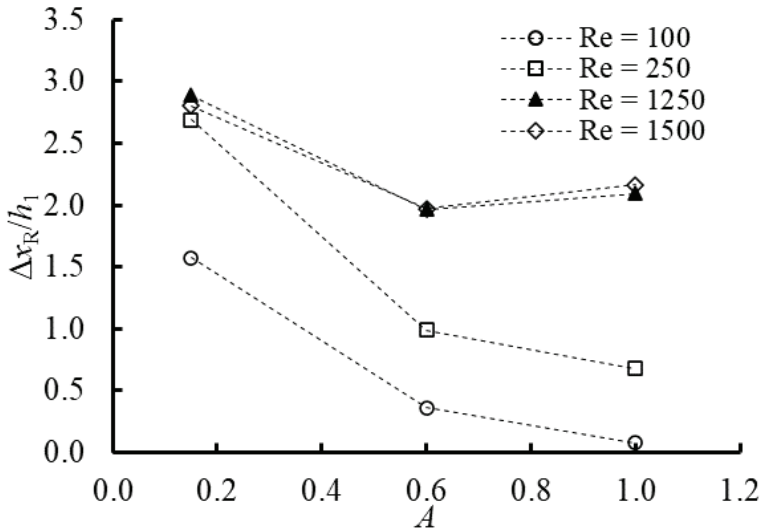


**Fig. 18** Experimentally obtained dependency of the relative recirculation zone length on  $Re_{h1}$  in stationary and pulsatile flow

By comparing the results of experiments in two types of cavities, it is observed that the recirculation zone reduction effect in laminar flow regime is inversely proportionate to pulsation amplitude, as the most significant effect is observed when  $A = 0.15$  and the least significant at  $A = 1$  (Fig. 19). In laminar flow regime high amplitude pulsations ( $A = 1$ ) introduce strong disturbances to the recirculation zone and the transitional-type cavity encloses it with a closely positioned FFS. This potentially leads to a perturbed and extensive recirculation zone. Low amplitude pulsations ( $A = 0.15$ ) lead to weaker recirculation zone disturbances; therefore leading to a more steady recirculation zone, which length is reduced due to the pulsatile flow impact on the vortices in the shear layer, as mentioned earlier. The highest recirculation zone length reduction is achieved at the beginning of the transitional flow regime in a transitional-type cavity at  $Re_{h1} = 250$  and is estimated to be  $\sim 45\%$



and  $\sim 17\%$  for  $A = 0.15$  and  $A = 0.60$ , respectively, compared with the case of stationary flow. Conversely, the pulsation frequency is shown to have a negligible effect on the recirculation zone length. It is observed that the discrepancies between cases with different frequencies were less than 6%. Nevertheless, the dynamic trend of the recirculation zone length in all pulsation cases remained the same as that of the stationary flow.



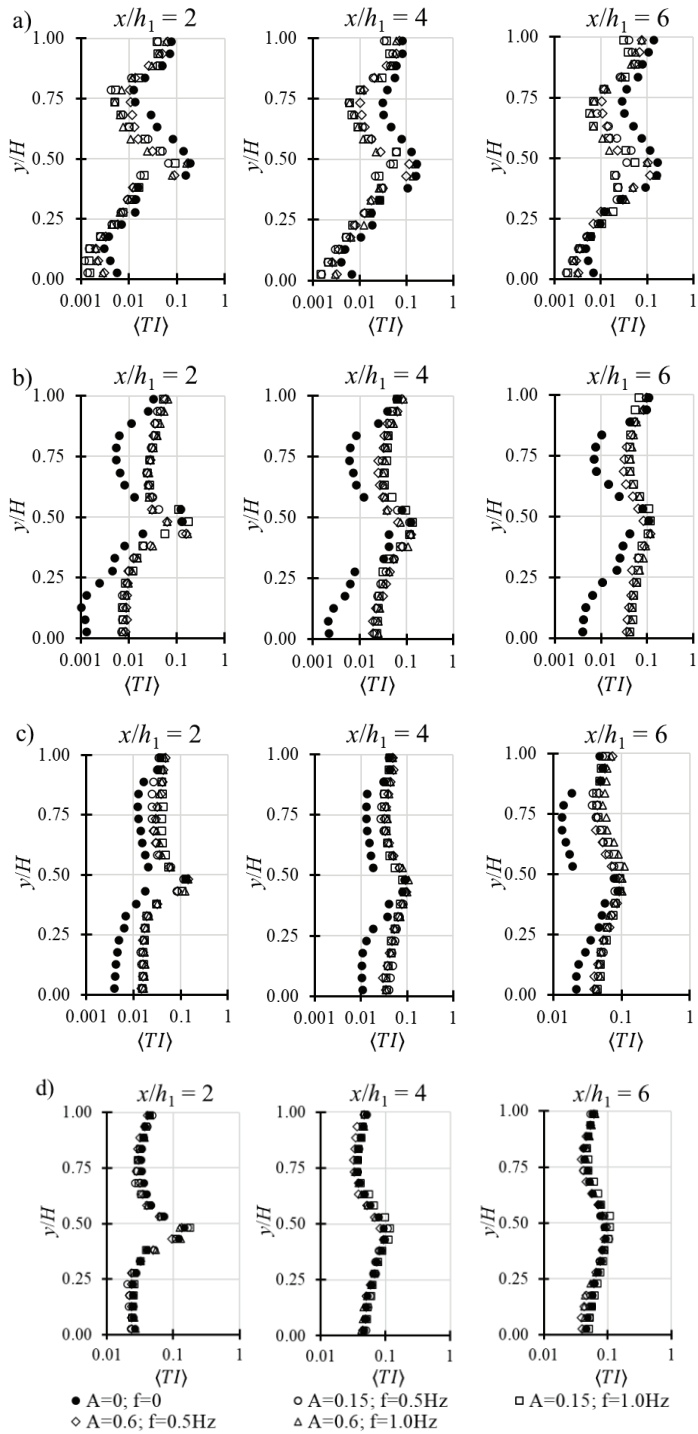
**Fig. 19** The impact of amplitude on recirculation zone length in laminar and transitional flow regimes

### 3.2.3. Pulsation amplitude impact on statistical flow parameters

After studying the recirculation zone dynamics in pulsatile flow, it is essential to highlight the impact of pulsation amplitude on statistical flow parameters. Studying parameters, such as vorticity, turbulence intensity, and shear rate, is crucial in investigating pulsatile flow structure. These parameters provide essential insights into the complex dynamics and characteristics of fluid behaviour. The vorticity distribution inside of the cavity is studied to understand the key information about the rotational behaviour of the fluid and the impact of pulsations on flow stability and mixing. The analysis of turbulence intensity distribution inside a cavity represents the magnitude of fluctuations in velocity and allows to determine the factors which influence it. Shear rate, which quantifies the rate of velocity gradient between adjacent fluid layers, is critical for evaluating the extent of fluid flow behaviour. Investigating shear rate in pulsatile flow structures allows to comprehend the impact of pulsations on the flow's shear-induced transport phenomena.

### 3.2.3.1. Impact of pulsation amplitude on turbulence intensity distribution in the cavity

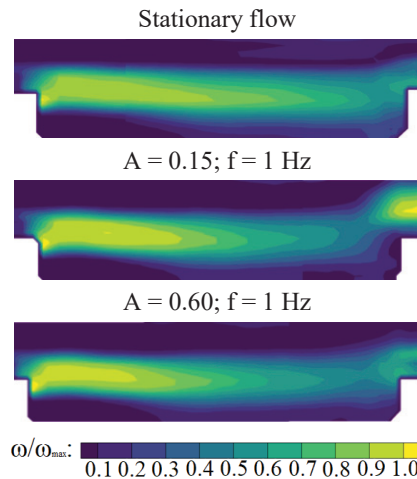
Experimentally obtained  $\langle TI \rangle$  profiles at different transitional-type cavity locations are shown in Fig. 20. At  $Re_{hl} = 500$ , pulsations decreased  $\langle TI \rangle$  in the main flow compared to stationary flow due to the presence of shear layer reattachment moments during the pulsation cycle when  $\frac{u(t_i)}{\langle u(t_i) \rangle} < 1$  (at  $180^\circ < \phi < 360^\circ$ ). Additionally, at  $Re_{hl} = 500$ , the flow is in the transitional regime, in which the velocity fluctuations are increased; therefore, as the velocity decreases during the pulsation cycle, the flow re-enters the laminar regime and reduces the  $\langle TI \rangle$  in all the pulsatile cases. As  $Re_{hl}$  increases to 1000–2000, the  $\langle TI \rangle$  dependency on the pulsatile parameters became less significant because the flow is starting to approach a turbulent regime, and the properties of additional disturbances become less relevant. In the cases of  $Re_{hl} = 1000$  and  $Re_{hl} = 1500$  (Fig. 20 b and c), the  $\langle TI \rangle$  in all the pulsatile flow cases exceeds that in the stationary flow. In transitional and turbulent flow regimes, the recirculation zone is decided by the periodically recurring vortices, which are altered by adding pulsations to the flow. Periodic variations in flow velocity may cause changes in the size, strength, and shedding frequency of vortices within the cavity, leading to increased instabilities and higher  $\langle TI \rangle$  in all pulsatile cases compared to stationary flow at  $Re_{hl} = 1000$  and  $Re_{hl} = 1500$ . However, demonstrating this effect is beyond the capabilities of the current experimental equipment and will be addressed in future research. At  $Re = 2000$  (Fig. 20 d), the velocity fluctuations caused by the turbulent flow regime became dominant; therefore, the instabilities caused by the pulsations were negligible, and a uniform distribution of  $\langle TI \rangle$  was observed.



**Fig. 20**  $\langle TI \rangle$  profiles at  $Re_{h_1}$  values of a) 500, b) 1000 c) 1500, and d) 2000

### 3.2.3.2. Impact of pulsation amplitude on vorticity and shear rate distribution in the cavity

Experimentally obtained relative vorticity contours in a transitional type cavity are shown in Fig. 21. Since the relative vorticity contours in cases with different pulsation frequencies coincided perfectly, only cases with different pulsation amplitude are presented. In all the investigated flow cases, the highest vorticity is located in the separated shear layer and at the edge of the FFS. In pulsatile flow, the vorticity increases at these locations due to increased vortex shedding. Higher vorticity values were indicated in the separated shear layer stretched downstream of the cavity. The separated shear layer tends to flap in the cavity (Kourta et al., 2015, Mushyam et al., 2016, Ceglia et al., 2020, Chiatto et al., 2020), which is consistent with low-amplitude pulsations ( $A = 0.15$ ) in the recirculation zone, thereby increasing the swirling motion. The vorticity increment in the shear layer is comparable for all the presented flow fields; however, the effect of pulsatile flow on the vorticity near the FFS is more significant at a lower amplitude. During the pulsation cycle with  $A = 0.15$ , the vortex formed behind the FFS is extruded from the cavity, resulting in a higher vorticity at the outlet. By contrast, during  $A = 0.60$  pulsations, the vortex dissipates with the recirculation zone.

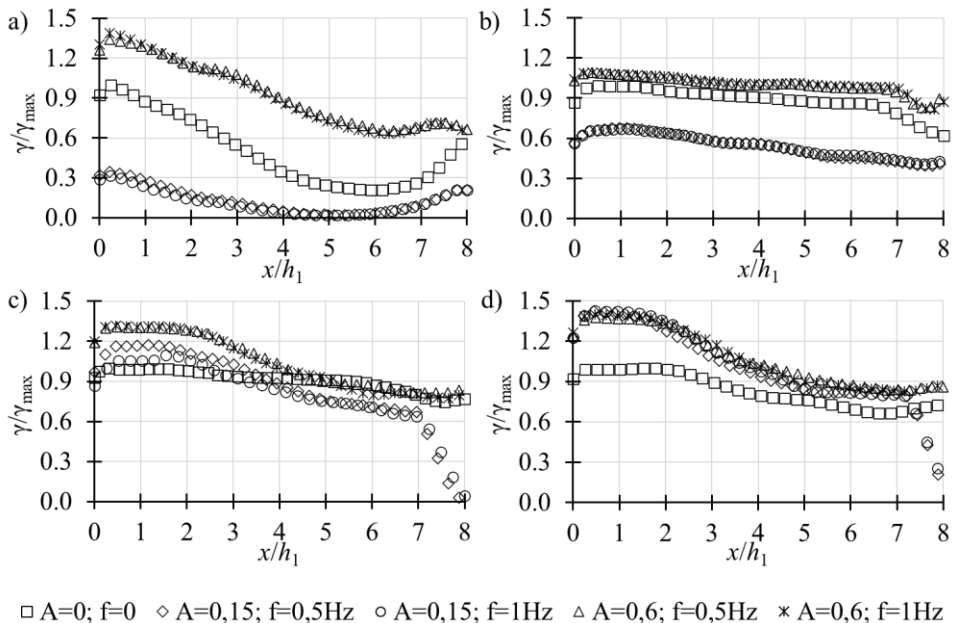


**Fig. 21** Relative vorticity  $\omega/\omega_{\max}$  contours in transitional type cavity of both stationary and pulsatile flow cases with different amplitudes at  $Re_{hl} = 1500$

Experimentally obtained longitudinal shear-rate profiles in Fig. 22 represent fluid mixing in the separated shear layer in a transitional-type cavity. The profile is located at the lid of the cavity. For calculations of share rate, the mean phase flow and fluctuations were not excluded as they were in the turbulence intensity distribution analysis. Parameter  $\gamma_{\max}$  corresponds to the maximum shear rate value of the stationary flow case. The shear-rate distribution along the cavity depends on the structure of the

recirculation zone, particularly its length. The recirculation zone length directly correlates with the length of the separated shear layer, thereby maintaining high shear stress values. The recirculation zone and separated shear layer at low  $Re_{h1}$  are sensitive to flow pulsations. At high pulsation amplitudes, the recirculation zone is disrupted, causing increased instabilities in the flow, whereas at low amplitudes, the energy of the disturbances decreases (Salek et al., 2009). Therefore, at  $Re_{h1} = 100$ – $500$ , the shear rate along the cavity decreased at low amplitudes and increased in high-amplitude cases compared with the case of stationary flow. At a higher  $Re_{h1}$  (i.e., 1500), the shear rate in the stationary flow became constant along the cavity. In this case, the cavity was filled with a stagnant recirculation zone, which is disrupted due to pulsations; therefore, the shear rate in the first section of the cavity ( $x/h_1 < 4$ ) increased in the pulsatile flow. As  $Re_{h1}$  increases further ( $Re_{h1} = 2000$ ), the differences between the different pulsatile flow cases diminish, and a higher shear rate is observed in the pulsatile flow.

At  $Re_{h1} = 1500$  and  $2000$ , the relative shear rate decreases abruptly at  $x/h_1 = 7$  in cases with  $A = 0.15$ . When the pulsation amplitude is low ( $A = 0.15$ ), the vortex near the FFS was extruded from the cavity, as can be seen in the vorticity contours (Fig. 21). Subsequently, the separated shear layer attached to the bottom of the cavity, thus resulting in a lower shear rate at the measured location. In the high-amplitude cases ( $A = 0.60$ ), the flow structure in the cavity remained stable during the pulsation cycle. Therefore, no abrupt changes in the statistical flow data were observed.



**Fig. 22** Longitudinal shear rate profile along the transitional-type cavity at  $Re_{h1}$  values of a) 100, b) 500, c) 1500, and d) 2000

### 3.2.4. The impact of pulsation frequency on flow structure

The results and analysis presented in section 3.2.4., as well as in all its subsections, are also presented in the publication<sup>2</sup>.

As previously shown, the pulsation amplitude has a significant influence on time-averaged recirculation zone dynamics and the statistical parameters of the flow, whereas the pulsation frequency had almost no effect. In the recirculation zone length analysis, the discrepancies between cases with different frequencies were less than 6%, meaning that the recirculation zone length depends only on amplitude. Nevertheless, pulsation frequency moderately affected the time-dependent development of recirculation regions such as corner and upper vortices and recirculation zone.

The analysis of pulsation frequency influence on flow structure presented in this section was conducted in a closed-type cavity for several reasons. Firstly, the variation of the recirculation zone length during the pulsatile cycle was studied in a closed-type cavity due to the longer relative length  $L/h_1 = 16$ , which allows the separated shear layer to reattach on the bottom of the cavity during the whole pulsatile cycle. In transitional-type cavity, this analysis would not be appropriate or would be possible only at a low Re since the separated shear layer reattachment otherwise would not be present throughout the whole pulsatile cycle. Secondly, this section presents an analysis of upper vortex dynamics during the pulsatile cycle, which would not be possible in a transitional-type cavity as its relative length is too low for the upper vortex to appear. The upper vortex is known to appear only in relatively long cavities of channels with BFS. Namely, due to these reasons, the following analysis was conducted in a closed-type cavity.

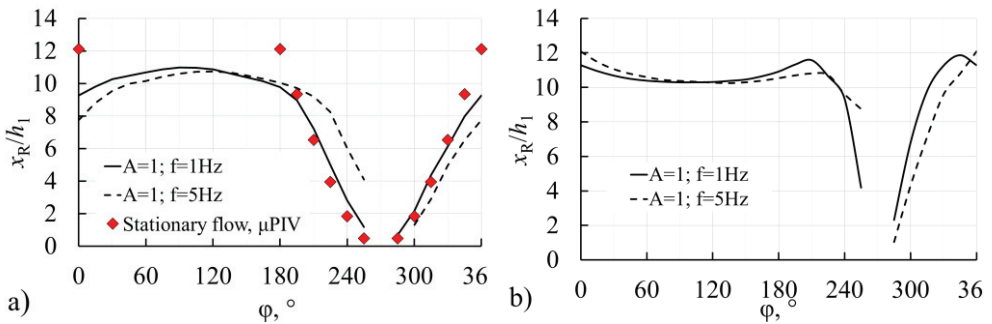
#### 3.2.4.1. Pulsation frequency impact on recirculation zone development during pulsation cycle

To investigate the behaviour of recirculation zone dynamics during the pulsation cycle and highlight the impact of pulsation frequency, the dependency of recirculation zone length on velocity phase angle was numerically obtained and analysed (Fig. 23). The pulsation cycle may be divided into two parts: velocity acceleration ( $0^\circ < \varphi < 90^\circ$  and  $270^\circ < \varphi < 360^\circ$ ) and deceleration phases ( $90^\circ < \varphi < 270^\circ$ ). During the cycle, velocity changes from 0 to  $2 \times u$ ; therefore, instantaneous  $Re_{h1}$  increases accordingly. Different recirculation zone length trends are observed in the first phase of the cycle at  $Re_{h1} = 300$  and 1500. In the case of  $Re_{h1} = 300$ , the recirculation zone length

---

<sup>2</sup> Šereika J., Vilkinis P., Pedišius N. Investigation of pulsatile flow structure in closed-type cavity. *International Journal of Heat and Fluid Flow*. 2021, Vol. 92, 108877, p. 1-7. ISSN 0142-727X.

increases because the flow is still in the laminar flow regime, and the recirculation zone is in its growth phase. While in the case of  $Re_{hl} = 1500$ , in the velocity acceleration phase, flow is approaching a turbulent flow regime, where recirculation zone length reduction is observed (Fig. 18). Therefore, convex and concave recirculation zone length trends in the range of  $0^\circ < \varphi < 210^\circ$ . In the velocity deceleration phase ( $90^\circ < \varphi < 270^\circ$ ), the recirculation zone length reduces until the flow is practically stopped and no typical separated shear layer reattachment to the bottom wall is observed; thus, no recirculation zone length could be measured, and point value at  $\varphi = 270^\circ$  is not given. Nonetheless, this flow structure lasts briefly, and a regular recirculation zone forms as the velocity increases.



**Fig. 23** The dependency of recirculation zone on velocity phase angle in a closed-type cavity ( $L/h_1 = 16$ ) a)  $Re_{hl} = 300$ ; b)  $Re = 1500$

Moderate discrepancies between different  $f$  cases in recirculation zone length throughout the cycle are observed. When  $f = 1$  Hz, at  $Re_{hl} = 300$ , higher recirculation zone length values are observed in the velocity acceleration phase and shorter in the deceleration phase compared to  $f = 5$  Hz case. The opposite effect is observed at  $Re_{hl} = 1500$ ; lower recirculation zone length values are observed at low pulsation frequency ( $f = 1$  Hz) in the acceleration phase. As the pulsation frequency increases, the pulse cycle period reduces; therefore, the velocity changes over time during the pulsation cycle are more significant and cause the flow structure to develop differently. A shorter pulsation cycle period causes the flow structure development lag effect (velocity phase angle-wise). The development of the recirculation zone lags approximately  $10^\circ - 15^\circ$  in the case with  $f = 5$  Hz compared to  $f = 1$  Hz. It is known that pulsations cause the lag phenomenon between velocity and pressure and that its significance relies on the  $Wo$  number, which is directly proportionate to pulsation frequency (Chun et al., 1996). Since the flow structure is more complex in cavities than in pipes, the lag phenomenon applies to the flow structure.

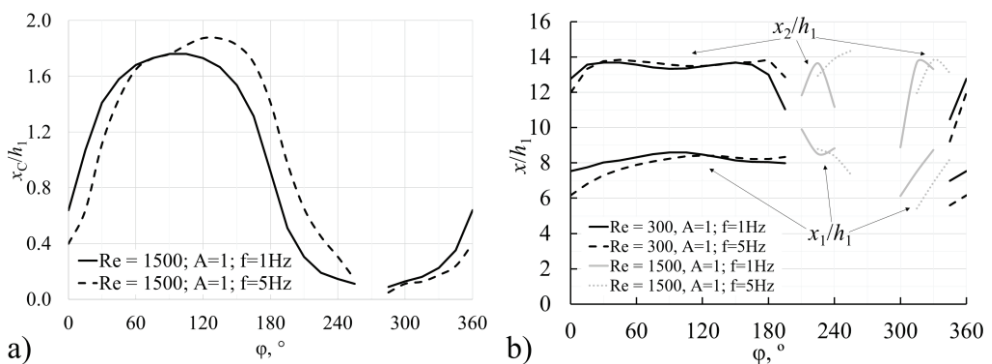
Experimentally measured relative recirculation zone length values, statistically approximated at every instantaneous  $Re_{hl}$  value from the experimental results, are presented in Fig. 23a. In the velocity phase angle range of  $180^\circ < \varphi < 360^\circ$ , the  $x_R/h_1$  values coincide almost perfectly with  $x_R/h_1$  values of stationary flow at different

instantaneous  $Re$ . In this range, flow is described as quasi-steady. However, differences occur in the range of  $0^\circ < \varphi < 150^\circ$ . For instance, at  $\varphi = 90^\circ$ , instantaneous  $Re_{h1}$  corresponds to  $Re_{h1} \sim 600$ . As can be seen from measured time-averaged recirculation zone length values (Fig. 14), flow reattachment is absent at this  $Re$ ; however, flow reattachment is observed in instantaneous flow fields (Fig. 23a). At this velocity acceleration phase ( $0^\circ < \varphi < 150^\circ$ ), the short pulsation period confines the recirculation zone from reaching its maximum value. Therefore, the flow is non-quasi-steady in this velocity phase angle range. Also, the reduced  $x_R/h_1$  is closely related to the increased growth rate of the shear layer. In Fig. 23b, the  $Re_{h1}$  number during the pulse cycle varies from 0 to 3000. It is beyond the capabilities of the  $\mu$ PIV system's measurement range; therefore, the experimental results are not presented.

### 3.2.4.2. Pulsation frequency impact on the corner and upper vortices in a closed-type cavity

Numerically simulated corner and upper vortex length variation graph and velocity streamlines of pulsatile flow during the pulsation cycle are given in Fig. 24 and Fig. 25 to visualise and highlight the impact of pulsation frequency on the development of recirculative regions.

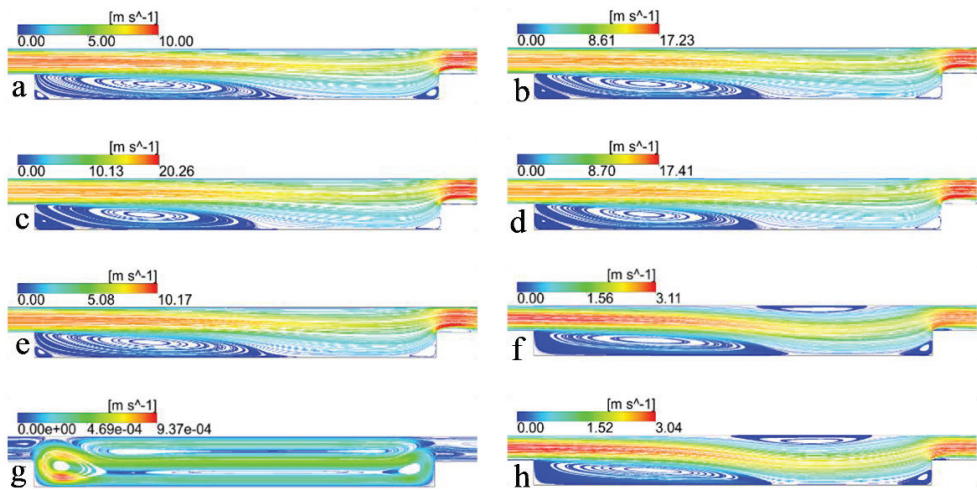
The development of corner vortex in closed-type cavity during the pulsation cycle is given in Fig. 24a. At the acceleration phase, pulsatile flow case with  $f = 5$  Hz shows slower corner vortex growth (velocity phase angle-wise) compared to case with  $f = 1$  Hz, however when the flow reaches deceleration phase ( $90^\circ < \varphi < 270^\circ$ ),  $f = 5$  Hz case shows higher  $x_C/h_1$  values. This phenomenon can be explained by the effects of flow inertia caused by pulsations, similarly as in the case of the recirculation zone (Fig. 23). Corner vortex is absent at  $\varphi = 270^\circ$ ; therefore, the  $x_C/h_1$  values are not given in the graphs.



**Fig. 24** Numerically simulated dependency of the relative length of the corner and upper vortices on velocity phase angle at different pulsation frequencies: a) corner vortex; b) upper vortex



The presence of an upper vortex is determined by an adverse pressure gradient generated by a sudden channel expansion. As can be seen from Fig. 24b, the upper vortex presence and length rely on  $Re$ . Values  $x_1$  and  $x_2$  show the beginning and the end of the upper vortex, respectively. Upper vortices are visible in Fig. 25 (at  $\varphi = 225^\circ$  and  $315^\circ$ ). The upper vortex is absent at the velocity angles corresponding to low instantaneous  $Re$ . As the upper vortex appears, the most notable length changes are observed at the velocity acceleration phase ( $300^\circ < \varphi < 30^\circ$ ), where rapid zone growth occurs and at the velocity deceleration phase ( $200^\circ < \varphi < 240^\circ$ ), before the upper vortex disappearance. The minimum instantaneous  $Re$ , which is required to form it, is approximately 200. In the first part of the cycle ( $0^\circ < \varphi < 180^\circ$ ), the location and length of the vortex remain constant. A comparison of the recirculation zone and upper vortex length dependencies on  $Re_{hl}$  shows that both zones have the same regularities. As the recirculation zone length increases, the upper vortex length also increases while keeping its position downstream of the shear layer reattachment point.

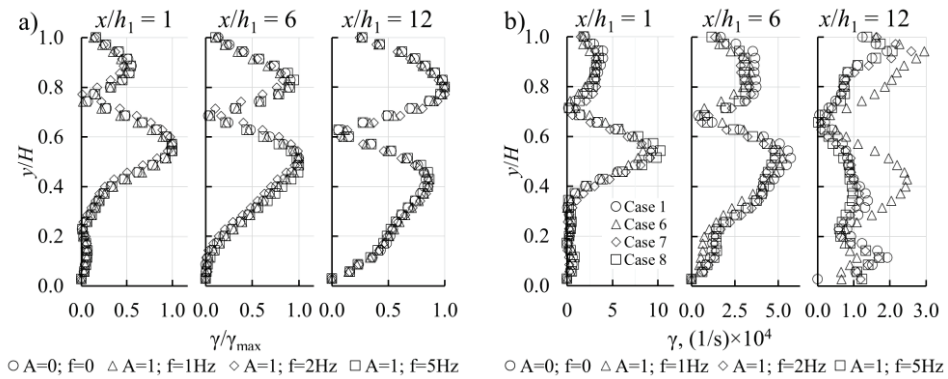


**Fig. 25** Velocity streamlines of the flow during different pulsation phases at  $Re = 1500$ ;  $f = 1$  Hz and  $A = 1$ : a)  $\varphi = 0^\circ$ ; b)  $\varphi = 45^\circ$ ; c)  $\varphi = 90^\circ$ ; d)  $\varphi = 135^\circ$ ; e)  $\varphi = 180^\circ$ ; f)  $\varphi = 225^\circ$ ; g)  $\varphi = 270^\circ$ ; h)  $\varphi = 315^\circ$

### 3.2.4.3. Pulsation frequency impact on shear rate distribution in a closed-type cavity

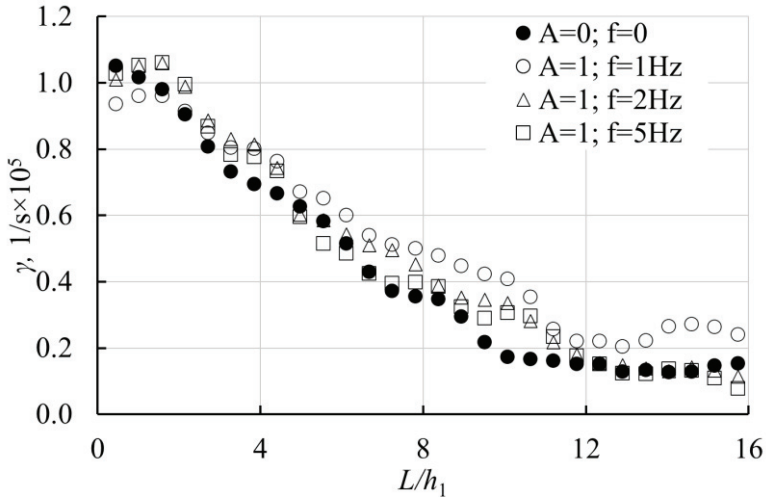
In Fig. 26a, no effect of pulsatile flow in general on the flow in the laminar flow regime is seen (at  $Re_{hl} = 300$ ); however, a significant impact can be observed at  $Re_{hl} = 1500$  (Fig. 26b). The shape of shear rate profiles corresponds to velocity gradients distribution in the flow. The highest gradients are observed in the interlayer between the recirculated flow and separated shear layer ( $y/H = 0.4-0.6$ ). These layers move with different velocities, and due to instabilities in the shear layer, mixing efficiency

increases in this region. Another shear rate peak is observed in the vicinity of the upper wall of the channel. It is induced by boundary layer interaction with the main flow and instabilities in the separated shear layer. As  $Re_{h1}$  increases up to 1500 (Fig. 26b), the recirculation zone structure changes from a steady to periodically recurring vortex system (Fig. 16); hence, more instabilities are formed in the interlayer between the recirculation zone and the main flow. Also, increased shear rate values are observed along the cavity in the transitional flow regime. In general, these values rapidly decrease downstream, in both laminar and transitional flow regimes, as instabilities generated at the upstream part of the cavity rapidly dissipate along the cavity. As can be seen, the pulsations do not affect vertical shear rate distribution in the laminar flow regime, and the influence is insignificant at the transitional flow regime in the recirculation zone ( $x/h_1 = 1-6$ ). However, horizontal shear rate profiles indicate increased velocity gradients along the cavity as pulsation frequency increases (Fig. 27).



**Fig. 26** Experimentally obtained vertical shear rate profiles at different closed-type cavity locations at a)  $Re_{h1} = 300$ ; b)  $Re_{h1} = 1500$

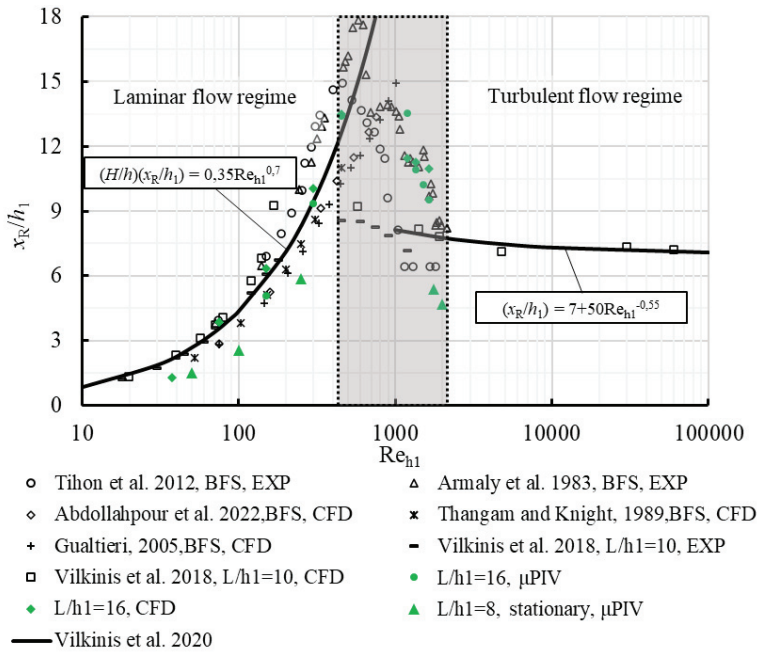
The influence of pulsations on vertical shear rate profiles is observed only at  $x/h_1 = 12$ , between the separated shear layer reattachment point and FFS (Fig. 26b). This effect is not observable in the laminar flow regime because the recirculation zone is stable; while in the transitional flow regime, reattachment length changes within certain limits over time, even in stationary flow (Vilkinis et al., 2018). In a transitional flow regime, this intrinsic pulsation resonates with added external velocity pulsations. Also, at certain velocity phase angles, the recirculation zone, upper vortex, and vortex near FFS periodically interact with each other, increasing instabilities.



**Fig. 27** Experimentally obtained shear rate profile along the closed-type cavity at  $y/H = 0.5$  and  $Re_{h1} = 1500$

### 3.2.5. Recirculation zone length dependency on $Re$ comparison with other studies

Fig. 28 shows a comparison of recirculation zone length dependency on  $Re_{h1}$  over BFSs and present cavities. Every data series given in Fig. 28 is obtained in channels with  $ER = 2$  for a fair comparison with the results of the present work. The results obtained from the literature are scattered; however, the fundamental regularities apply and can be defined. Almost linear dependence of the recirculation zone on  $Re$  is observed when the flow is in a laminar flow regime. The maximum recirculation zone length is reached in the transitional flow regime. Eventually, in the transitional flow regime, the recirculation zone length begins to decrease as the  $Re$  increases due to the instabilities introduced by the transitional flow itself. In the turbulent flow regime, the recirculation zone length stabilises at its asymptotic value and is no longer dependent on  $Re$ . The presence of FFSs does not impact the given dependencies; therefore, the results of the present work are distributed between the results in channels with BFSs. The dependency determined by Vilkinis et al. (Vilkinis et al., 2020) perfectly describes the regularities of other studies as well as results from the present work. Even though the regularities of recirculation zone length dynamics coincide, the discrepancies are observed between the results of other studies and present work due to the presence of FFS, which confines the recirculation zone from growing further; therefore, the  $x_R/h_1$  values are lower in cavities compared to channels with BFS.



**Fig. 28** The comparison of recirculation zone length dependency on Re with other studies

### 3.3. Passive flow control

#### 3.3.1. Adjustment of cavity geometrical parameters

The results and analysis presented in section 3.3.1, as well as in all its subsections, are also presented in the publication<sup>3</sup>.

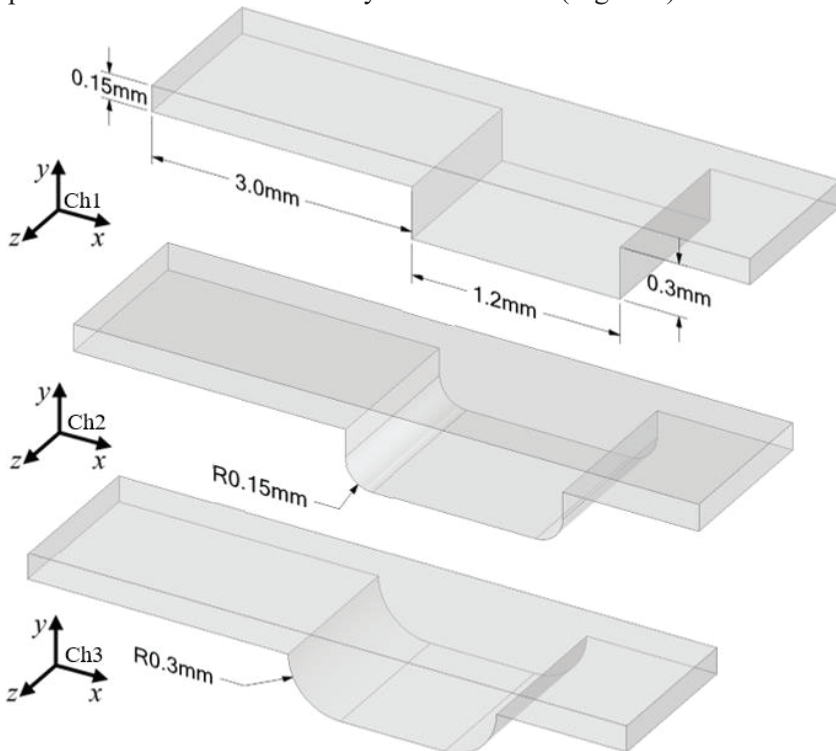
In various aero and hydrodynamic applications, the velocity distribution is important in understanding and optimising various fluid dynamics phenomena. For example, in a controlled environment of wind tunnels, the even distribution of velocity is a fundamental aspect influencing the behaviour of fluids and is a main factor impacting measurement accuracy. The velocity distribution can be passively controlled by altering the geometry of the channel. In this section, a few problems related to practical applications are addressed. Firstly, the impact of cavity inner corner curvature influence on velocity distribution and flow structure is addressed. This problem naturally occurs due to the limitations of the experimental channel manufacturing method, where inner cavity corners are half-rounded with the corner radius and step height ratio of  $R/h_1 = 0.5$  (see Table 1). It is necessary to determine the impact of such geometry alterations to analyse separated fluid dynamics

<sup>3</sup> Šereika J., Vilkinis P., Pedišius N. Analysis of Cavity Corner Geometry Effect on Recirculation Zone Structure. *Applied Sciences*. 2022, Vol. 12, Iss. 12, 6288, p. 1-12. ISSN 2076-3417.

accurately. Secondly, the study of cavity outlet/inlet hydraulic diameter ratio impact on longitudinal velocity distribution is purposed to study the velocity distribution inside a wind tunnel for airflow velocity reproduction. It was noticed that in the measurement chamber, the velocity distribution was significantly affected by its geometrical parameters, thus naturally forming the need for a study where the influence would be determined. The even velocity distribution would potentially increase the accuracy of the measurement.

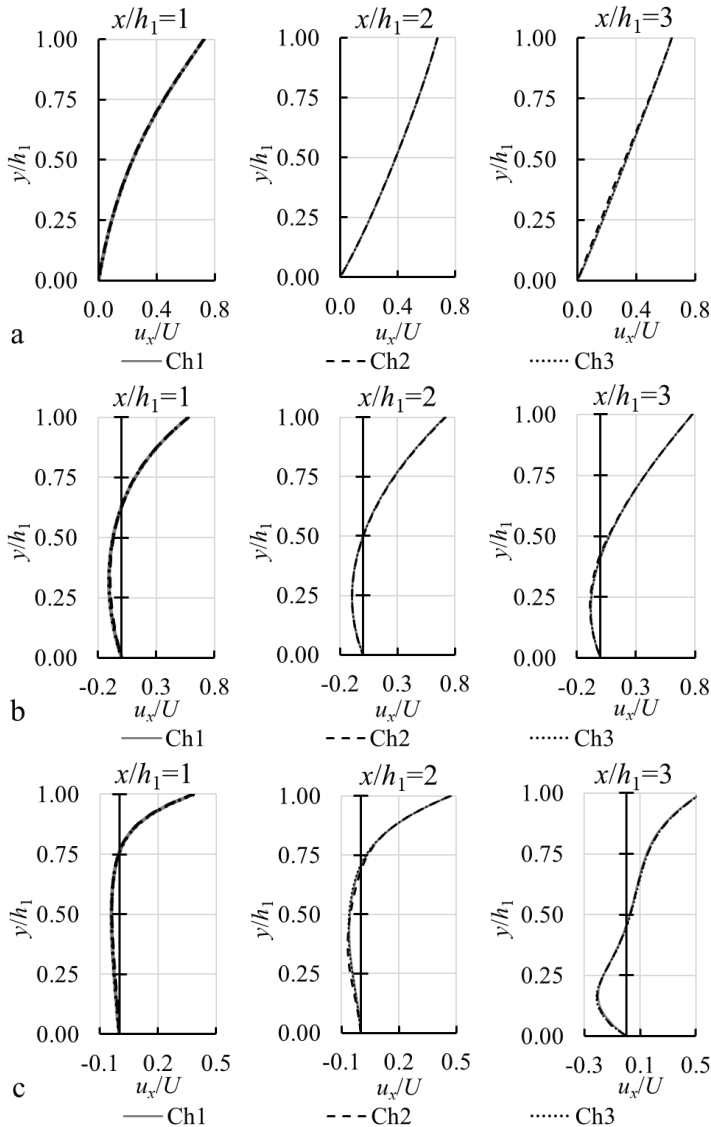
### 3.3.1.1. Cavity inner corner curvature influence on the velocity distribution

Numerical simulations were performed in three different configurations of open-type cavities (Fig. 29). Ch1 is a cavity with sharp inner corners, whereas channels Ch2 and Ch3 have inner corner curvature of  $R = 0.15$  mm and  $0.30$  mm, respectively. These distinct values of  $R$  were chosen to cover the full range of  $R/h_1$ , ranging from  $R/h_1 = 0$  (Ch1) to  $R/h_1 = 1$  (Ch3), while Ch2 is the intermediate point between them ( $R/h_1 = 0.5$ ). All investigated geometries were three-dimensional, with channel width  $b = 0.9$  mm, ensuring the aspect ratio of  $AR = 3$ . Open-type cavity channels were simulated with a top symmetry plane, thus imitating the experimental channel given in Table 1a. The numerical simulation results with Ch2 were compared with experiments to ensure the validity of simulations (Fig. 12a)



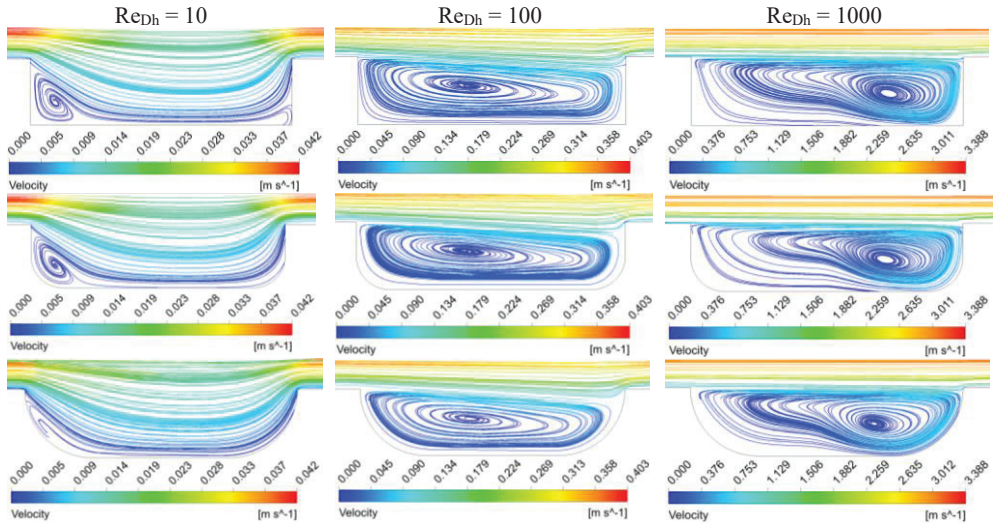
**Fig. 29** Open-type cavities with a different curvature radius of inner corners

Fig. 30 shows the relative velocity distribution inside of cavities. Velocity profiles are obtained in the middle plane of the cavity at  $x/h_1 = 1, 2,$  and  $3$ . The comparison between different cavity inner corner radii of curvature cases shows that the velocity distribution coincides almost perfectly between the investigated channels and does not depend on the curvature radius of inner cavity corners. The discrepancies between different  $R$  cases are unobservable even when the corner is fully rounded (Ch3).



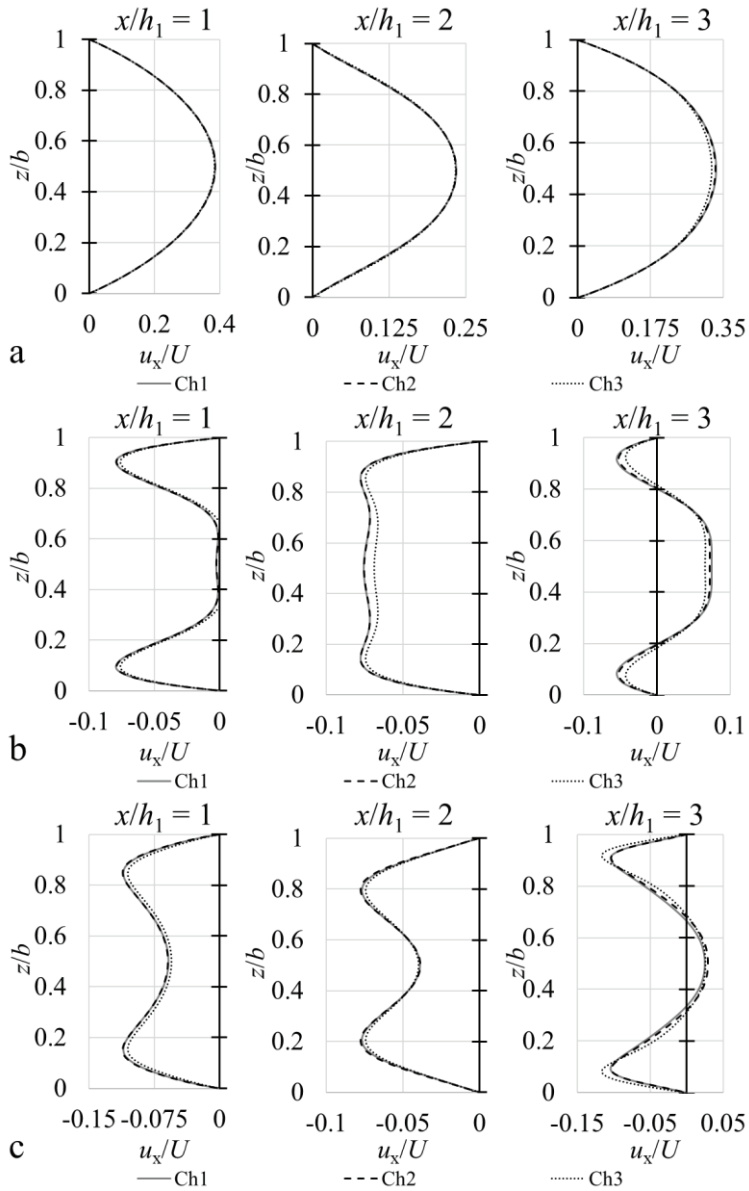
**Fig. 30** Numerically obtained  $u_x$  profiles in open-type cavities with different step configurations at a)  $Re_{Dh} = 10$ ; b)  $Re_{Dh} = 100$ ; c)  $Re_{Dh} = 1000$

Velocity streamlines taken in the middle plane of cavities ( $z/b = 0.5$ ) also show an almost perfect match between Ch1, Ch2 and Ch3 (Fig. 31). The only difference is the size of the recirculation zone in Ch3 at  $Re_{Dh} = 10$ . A fully rounded cavity inner corner causes smoother fluid flow over it compared to Ch1, decreasing the adverse pressure gradient caused by a sudden channel expansion. However, this difference occurs only at  $Re_{Dh} = 10$  and does not influence the further development of the flow as it passes along the cavity.



**Fig. 31** Velocity streamlines in Ch1, Ch2 and Ch3

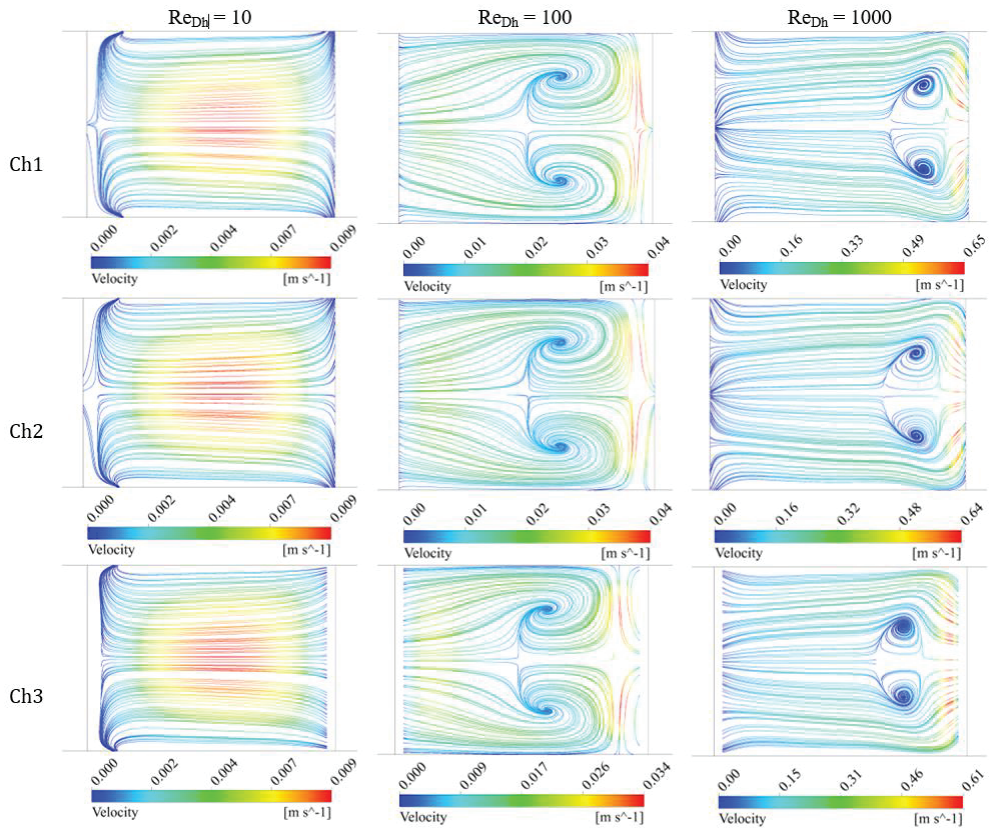
For a further comparison, velocity distribution in the  $x$ - $z$  plane was analysed (Fig. 32). The profiles are obtained at the height of  $y/h_1 = 0.5$ . Similarly, as in Fig. 30, the  $x$ - $z$  axis velocity distribution in open-type cavities with different inner step curvature coincide almost perfectly. Ch3 configuration had the most influence, as it showed a slightly decreased velocity in the channel centre at  $x/h_1 = 3$  (Fig. 32). However, the discrepancies between velocity distribution were only marginal.



**Fig. 32**  $x$ - $z$  axis velocity profiles at a)  $Re_{Dh} = 10$ ; b)  $Re_{Dh} = 100$ ; c)  $Re_{Dh} = 1000$

To study the velocity distribution and highlight the impact of inner corner curvature, the  $x$ - $z$  axis velocity streamlines are presented in Fig. 33. At  $Re_{Dh} = 10$ , the flow velocity distribution is identical in Ch1, Ch2 and Ch3. A slightly different formation of lateral vortices is observed at  $Re_{Dh} = 1000$ , whereas the cores of the vortices are positioned closed together in Ch3. Otherwise, all three open-cavity inner corner configurations seem to coincide perfectly.



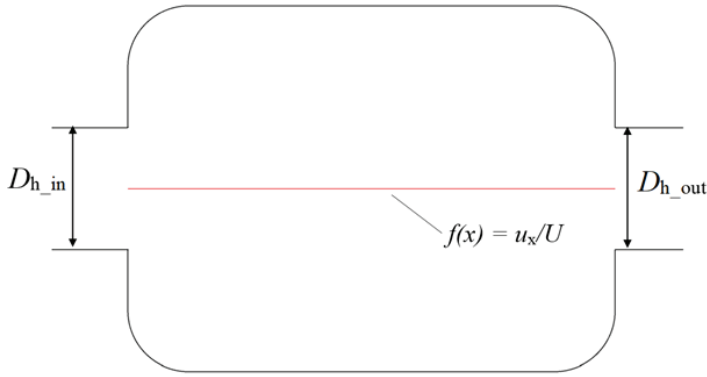


**Fig. 33**  $x$ - $z$  plane velocity streamlines in Ch1, Ch2 and Ch3

From  $x$ - $y$  and  $x$ - $z$  plane velocity distribution analysis in cavities with different inner corner configurations, it is evident that the impact of corner curvature has only marginal effects on the flow structure. As the three distinct values of  $R/h_1$  were investigated, the velocity distribution was shown to be almost identical in the range of  $R/h_1 = 0 - 0.5$  with slight discrepancies in the range of  $R/h_1 = 0.5 - 1$ , meaning that the curvature of inner cavity corners does not influence the flow; therefore, the flow structure is determined by other parameters, such as  $L/h_1$ , ER, Re, etc.

### 3.3.1.2. Cavity outlet/inlet hydraulic diameter ratio impact on the longitudinal velocity distribution

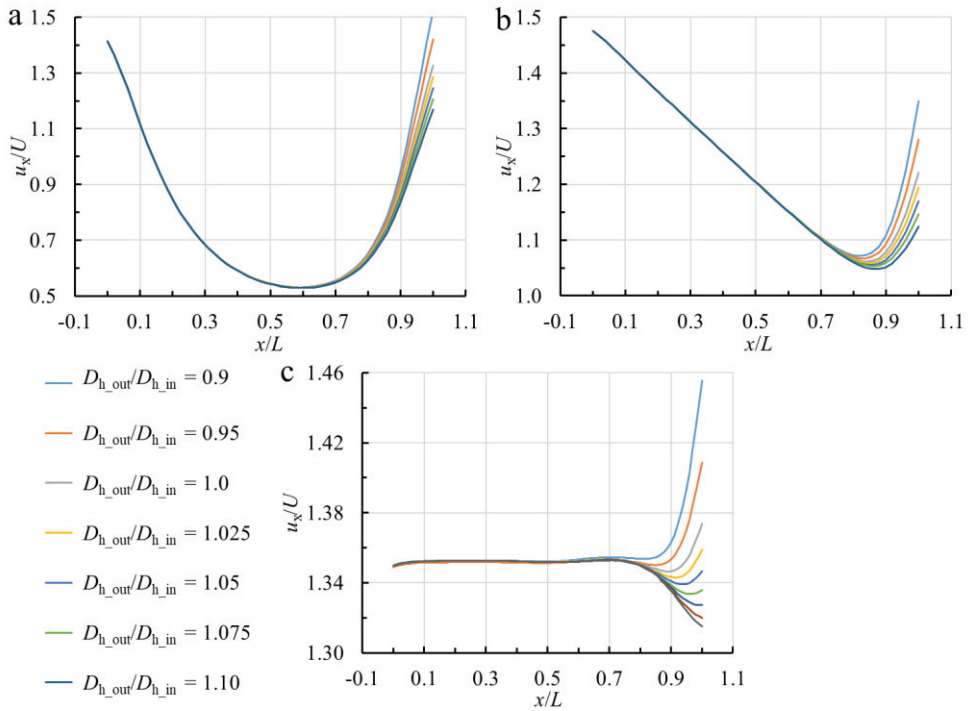
Fig. 34 represents the geometry that was used in numerical simulations. To investigate the impact of the outlet/inlet hydraulic diameter on longitudinal velocity distribution, the inlet diameter  $D_{h\_in}$  was kept constant, whereas the outlet hydraulic diameter was changed. Longitudinal velocity distribution is a characteristic that describes the stable fluid flow, where the flow without any sudden velocity deviations is considered to be stable.



**Fig. 34** The scheme of an open-type cavity ( $L/h_1 = 4$ ) with the location of the longitudinal velocity profile

Longitudinal velocity distribution in the middle of an open-type cavity at  $Re_{Dh} = 10 - 1000$  is given in Fig. 35, which represents three different flow cases depending on its structure:  $Re_{Dh} = 10$  – the separated shear layer is reattached on the cavity bottom,  $Re_{Dh} = 100$  – the separated shear layer reattachment is absent, and the centre of recirculation zone is located near the BFS and  $Re_{Dh} = 1000$  – the separated shear layer reattachment is absent, and the recirculation zone centre is shifted towards FFS. The regularities of velocity distribution in the cavity are directly related to its geometrical parameters, as the decrease of velocity is seen when the channel cross section increases and the increase of velocity as the area decreases at  $Re_{Dh} = 10 - 100$ . The velocity in channels with different  $D_{h\_out}/D_{h\_in}$  ratios coincides almost perfectly when  $x/L < 0.8$ , indicating that the outlet/inlet hydraulic diameter does not influence the flow structure inside an open-type cavity until  $x/L > \sim 0.8$ . At that point, the velocity is inversely proportionate to  $D_{h\_out}$ . The highest velocity is achieved at the lowest investigated  $D_{h\_out}/D_{h\_in}$  ratio, while the lowest is achieved at the highest  $D_{h\_out}/D_{h\_in}$ . This insight applies to both investigated  $Re_{Dh}$  cases.

At  $Re_{Dh} = 10 - 100$ , the separated shear layer does not reattach on the cavities' bottom wall in both upper and lower cavities; therefore, the flow after entering the sudden expansion of the channel is restricted by the shear layers. From Fig. 31, an inclined shear layer positioning can be observed at  $Re_{Dh} = 10 - 100$ ; therefore, the main flow core expands as the fluid moves towards the outlet of the cavity, which causes the velocity to decrease as it is seen in Fig. 35. This effect does not apply to  $Re_{Dh} = 1000$ , as in this case due to higher velocity of the main flow, the centre of recirculation zone is shifted towards the FFS, thus, determining the straight horizontal location of the separated shear layer, which restricts the main flow core from expanding. This ensures the constant flow velocity until  $x/L = \sim 0.8$  at  $Re_{Dh} = 1000$  (Fig. 35c).



**Fig. 35** Longitudinal velocity distribution in the middle of the open-type cavity with a different outlet to inlet hydraulic diameter ratio, at a)  $Re_{Dh} = 10$ ; b)  $Re_{Dh} = 100$ ; c)  $Re_{Dh} = 1000$

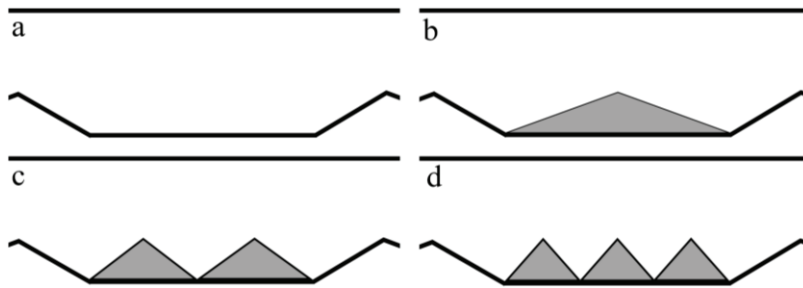
### 3.3.2. Implementation of roughness elements

The results and analysis presented in section 3.3.2, as well as in all its subsections, are also presented in the publication<sup>4</sup>.

The implementation of passive flow control is a viable alternative for controlling the recirculation zone dynamics and impacting the whole velocity distribution. Roughness elements confine the recirculation zone from the formation of large vortices, thus influencing the flow structure. By controlling the flow structure, it is possible to enhance the stability and ensure the gradual velocity distribution, thus controlling the separated flow behaviour. Ensuring flow stability and uniform velocity distribution is an important problem in ultrasonic flow meters, where the measurement accuracy depends on the ultrasonic transit time, which can vary due to unstable flow behaviour and have a negative impact on measurement accuracy. The geometry chosen for the study of roughness elements imitates the channel of modern ultrasonic

<sup>4</sup> Vilkinis P., Šreika J., Pedišius N., Zygmantas G. Experimental study of flows over triangular riblets in cavity-like geometry. *Experimental Thermal and Fluid Science*. New York: Elsevier, 2022, Vol. 134, 110621, p. 1-9. ISSN 0894-1777.

flow meters, where the sudden change in the cross-section is due to the influence of the inclined steps, which are created as obstacles rather than channel expansions (Rincón et al., 2022, 2023, 2024). Such geometry of a cavity results in unstable flow and uneven velocity distribution that can be controlled passively by implementing the roughness elements. In this section, the implementation of roughness elements is investigated and discussed by means of studies of recirculation zone dynamics, the influence of different roughness element configurations on velocity distribution, statistical parameters, and pressure loss characteristics. To study the effects of roughness elements on the separated flow dynamics, four different roughness element configurations have been chosen: a plain cavity and three cases of roughness elements installed on the bottom of the channel, including 1-3 triangular roughness elements (Fig. 36).



**Fig. 36** Schematic representation of experimental channel with different number of roughness elements: a – 0; b – 1; c – 2; d – 3

### 3.3.2.1. Roughness element impact on velocity distribution inside a cavity

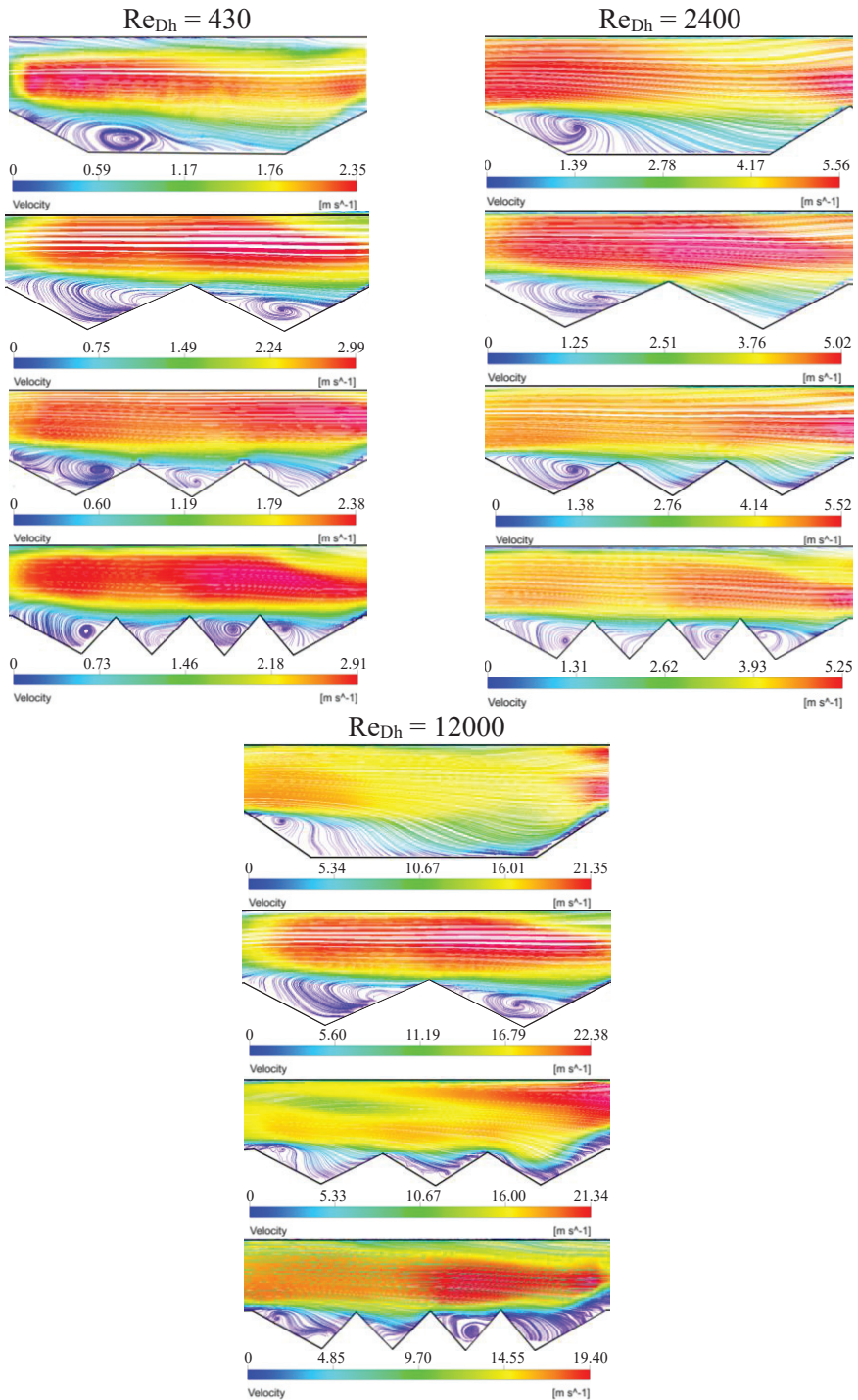
Experimentally obtained mean velocity streamline fields at  $Re_{Dh} = 430$ , 2400, and 12000 are presented in Fig. 37. In the plain cavity case ( $\lambda = 8.8$ ), flow field measurements depict a recirculation zone at the bottom of the cavity. At  $Re_{Dh} = 430$  and 2400, a well-defined clockwise flow recirculation region is formed, occupying  $\sim 0.3$ – $0.5$  of the cavity length. At  $Re_{Dh} = 12000$ , the vortex core is shifted upstream, its size decreases, and the whole vortex is located on the cavity's inclined wall.

Afterwards, the cavity is divided into several subcavities by introducing triangle-shaped obstacles on the bottom wall. Obstacle height is equal to the depth of the cavity, and its length depends on the number of obstacles presented. In the case of one triangle-shaped roughness element presence, two triangle cavities of  $\lambda = 4.7$  are formed. In the case of  $Re_{Dh} = 430$ , vortices are formed in both cavities, while the vortex in the first cavity is visibly larger. At  $Re_{Dh} = 2400$ , the first subcavity is fully occupied with a recirculation zone, whose core is located near the cavity's trailing wall. The recirculation zone in the second subcavity is not formed. The shear layer again separates from the vertex of the roughness element; however, velocity and pressure gradients are insufficient to create a vortex. In the case of  $Re_{Dh} = 12000$ , the

recirculation zone is again divided into two vortices. In the second subcavity, the recirculation zone visibly shifted towards the cavity's bottom. Based on the streamlines with one roughness element, it is evident that due to known instabilities of the transitional flow regime, the recirculation zone cannot be divided into two vortices at  $Re_{Dh} = 2400$ , while the opposite situation is observed in laminar and turbulent flow regimes.

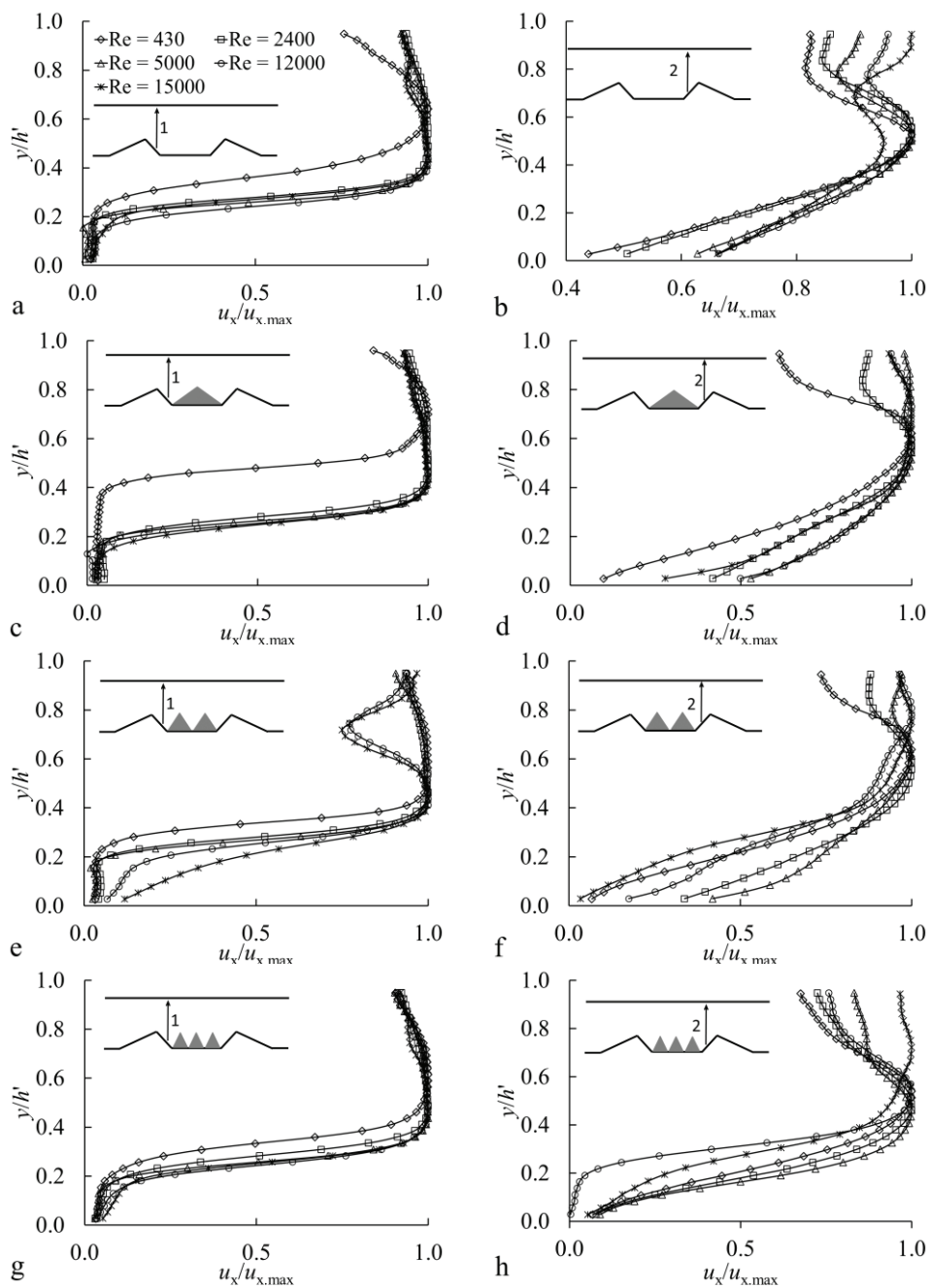
Further increasing the number of roughness elements on the bottom wall increases the number of subcavities as their size decreases. In the case of three formed subcavities, their size decreases to  $\lambda = 3.3$ . At  $Re_{Dh} = 430$ , the vortices are formed only in the first two subcavities, while the vortex in the third one is absent. In the transitional flow regime ( $Re_{Dh} = 2400$ ), the vortex is present only in the first subcavity for the same reason as in  $\lambda = 4,7$  case. At  $Re_{Dh} = 12000$ , high curvature streamlines near the leading edge are observed in the the first two subcavities, showing high velocity gradients and the beginning of vortex formation. The shear layer separated from the vertex of previous obstacle bridges above the subcavity.

In the case of three triangle-shaped roughness elements, subcavities size decreases to  $\lambda = 2.8$ . At the lowest and the highest  $Re_{Dh}$  numbers investigated, vortical structures in the subcavities are not well-defined in the mean flow; however, high curvature streamlines are presented, indicating disturbed flow in the subcavities. Recirculation zones are presented in all cavities at  $Re_{Dh} = 2400$ . As the size of roughness elements decreases (their number increases), the distance between vertices decreases as well, and the flow cannot reattach itself. Therefore, stagnant vortices are formed in the subcavities.



**Fig. 37** Velocity streamlines in cavities with different roughness element configurations at  $Re_{Dh} = 430 - 12000$

For further analysis, the roughness element impact on velocity distribution is experimentally investigated. In the plain cavity (Fig. 38a and b), changes in velocity profiles are observed mainly in the first part of the cavity (path 1). The distinct case of  $Re_{Dh} = 430$  can be explained by the dynamics of the recirculation zone on the bottom. At  $Re_{Dh} = 430$ , the recirculation zone is still in its development stage. After  $Re_{Dh}$  increases, recirculation zone size and velocity distribution become constant; thus, velocity profiles also become uniform. In Profile 2, discrepancies in profiles are observed on the inclined FFS. Differences in the velocity distribution are determined by a different streamline curvature at the step depending on  $Re$ . A similar situation is observed in the case of two  $\lambda = 4.7$  subcavities (Fig. 38 c and d). Vortex in the first subcavity is not yet fully developed at low  $Re_{Dh}$  numbers; therefore, discrepancies compared with profiles obtained at higher  $Re_{Dh}$  numbers are observed. The influence of the separated boundary layer from the upper wall is observed in  $\lambda = 3.3$  cavities (Fig. 38 e and f) in Profile 1. The effect is visible as local velocity reduction (at  $y/h' = 0.6-0.8$ ) at high  $Re_{Dh}$  numbers in the vicinity of the upper wall. In the second part of the measuring domain, velocity profiles are disturbed by the separated shear layer from the second vertex of the roughness elements. High velocity gradients are present above this vertex; therefore, the velocity distribution is not uniform near leading and trailing ramps. As the number of roughness elements further increases and subcavities' size decreases (Fig. 38 g and h), velocity profiles in Profile 1 no longer depend on  $Re_{Dh}$ . Only slight discrepancies are observed between velocity profiles. However, discrepancies increase in the second part of the measuring domain. These discrepancies are caused by the reattached shear layer from the upper wall, as shown in Fig. 39 g and h. Instabilities in the separated boundary layer depend highly on  $Re_{Dh}$ ; therefore, discrepancies between velocity profiles are observed.

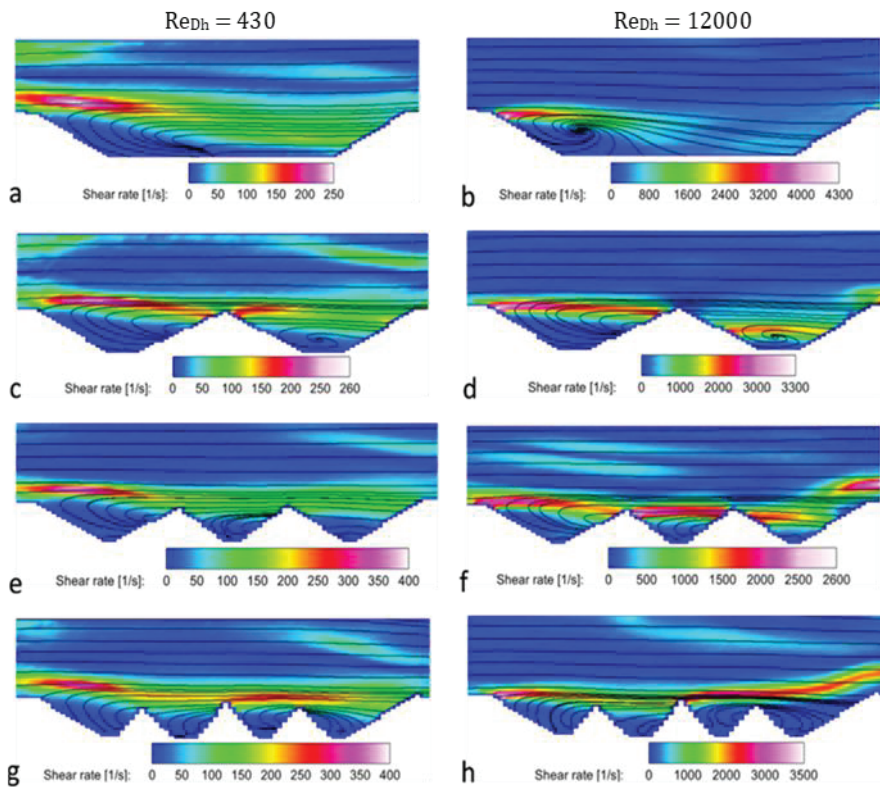


**Fig. 38** Velocity profiles measured in cavities with the configuration of roughness elements; a) and b)  $\lambda = 8.8$ ; c) and d)  $\lambda = 4.7$ ; e) and f)  $\lambda = 3.3$ ; g) and h)  $\lambda = 2.8$ , at  $Re_{Dh} = 430 - 15000$



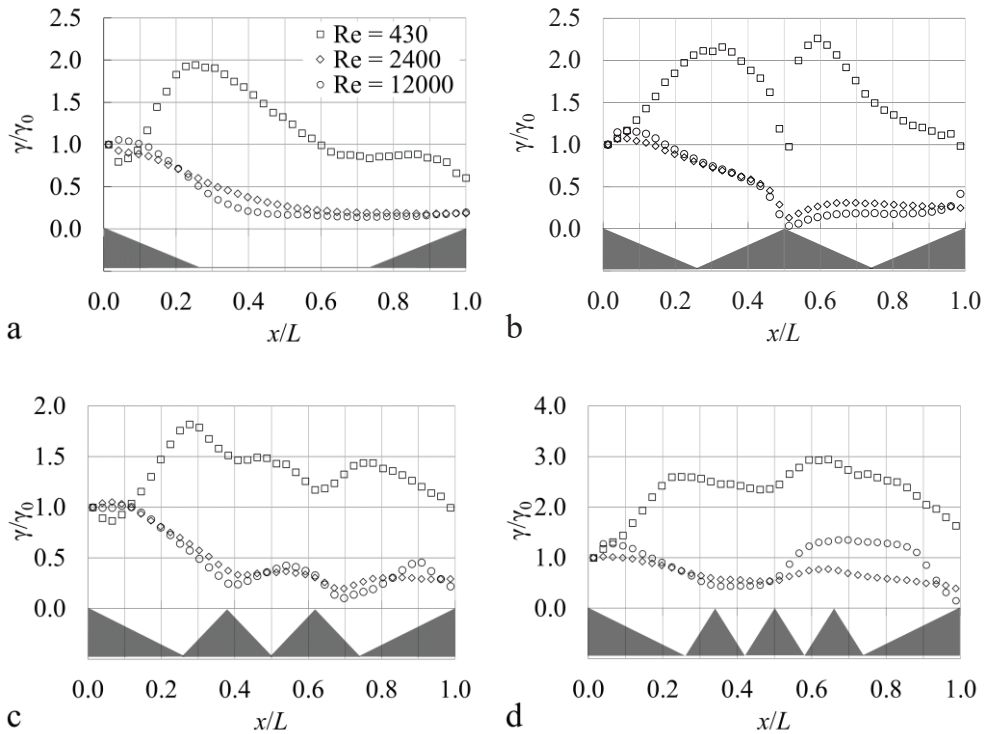
### 3.3.2.2. Impact of roughness elements on shear rate distribution

Shear rate reveals at which rate fluid layers move past each other; therefore, a higher shear rate means that higher velocity gradients are present and more momentum in the form of shear stress is transferred to the upper layer of fluid. As shown in experimentally obtained shear rate scalar maps presented in Fig. 39, the maximum shear rate is observed at the edge of the leading edge of the plain cavity, regardless of the number of roughness elements downstream. At this location, the shear layer separates, and the highest velocity gradients are present. As the number of roughness elements increases, the shear layer separates from every roughness element vertex. In the cases of high  $Re_{Dh}$  numbers, increased shear rate values are observed along the upper wall. Also, as the number of subcavities increases, the boundary layer separates from the upper wall. Separation occurs around the middle part of the measurement domain, and the effect is the strongest in the case of  $\lambda = 2.8$ . As the  $Re_{Dh}$  number increases, the location of separation is shifted upstream. This separation causes velocity profile discrepancies, as seen in Fig. 38 e.



**Fig. 39** Shear rate scalar maps in the cases of a), b) plane cavity; c), d)  $\lambda = 4.7$ ; e), f)  $\lambda = 3.3$ ; g), h)  $\lambda = 2.8$ , at  $Re_{Dh} = 430$  and  $Re_{Dh} = 12000$

Horizontal shear rate profiles along the cavity are presented in Fig. 40. Profiles are experimentally measured starting from the leading edge of the first cavity and finishing at the last cavity's trailing edge. In the case of the plane cavity (Fig. 40 a), a profile is measured along the entire cavity. Shear rate values are normalised by the shear rate value at the leading edge of the cavity ( $x/L = 0$ ).



**Fig. 40** Shear rate  $\gamma/\gamma_0$  profiles along measured cavities: a) plain cavity; b)  $\lambda = 4.7$ ; c)  $\lambda = 3.3$ ; d)  $\lambda = 2.8$ , at  $Re_{Dh} = 430 - 12000$

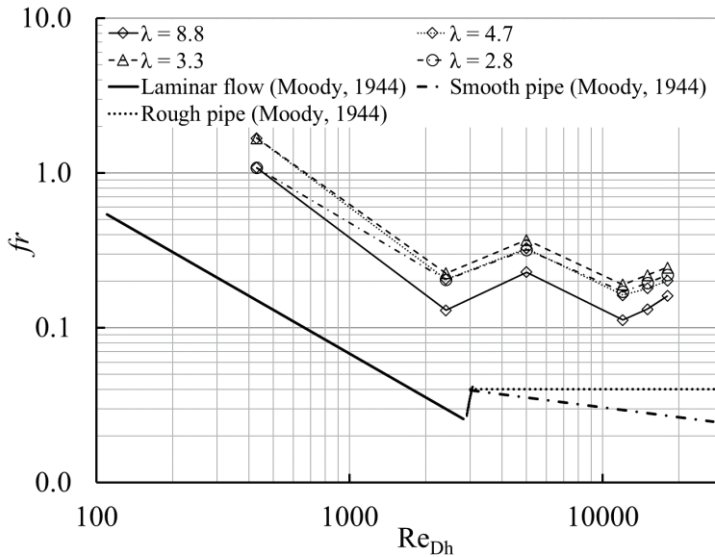
As can be seen from all roughness element configuration cases presented, apparent differences are observed in profiles measured in laminar and turbulent flow regimes. Higher relative shear rate values are measured in the laminar flow regime ( $Re_{Dh} = 430$ ); also, peak values of shear rates are located at a certain distance in the cavity. This is because laminar vortices are elongated along the cavity; thus, the strongest mixing and the location of high velocity gradients between the separated shear layer and recirculating zone occurs further downstream. After the transition to the turbulent flow regime, peak shear rate values are located at the shear layer separation point ( $x/L = 0$ ) due to turbulent boundary layer separation at the leading edge of the cavity. Shear rate profiles measured at  $Re_{Dh} = 2400$  and  $12000$  are practically identical along the cavity. In the cases of  $\lambda = 4.7$  and  $3.3$  (Fig. 40 b and c), shear rate minimum values are observed above the vertices of roughness elements. In

these cases, subcavities are relatively wide, and form recirculation contour reattaches at the wall of the roughness element ahead. Therefore, a zone with small velocity gradients is created in the vicinity of roughness element vertices. However, in the case of three roughness elements presented ( $\lambda = 2.8$ ) (Fig. 40 d), the streamwise vortices stay above the roughness elements as explained in the study by Choi et al. (Choi et al., 1993). Thus, in the time-averaged velocity fields, the stagnation zone around roughness element vertices disappears.

### **3.3.2.3. Pressure drop characteristics and friction factor dependence of roughness element configuration**

Analysis of pressure drop is intended to determine the variation of pressure losses depending on filling the cavity with roughness elements at different flow regimes. As seen in Fig. 41, the major contribution to the pressure loss is determined by the ramps in the channel forming the plain cavity. High ramps occupying one-third of channel height ( $s/H = 1/3$ ) cause a sharp narrowing of channel cross-section and corresponding high friction factor values. It can be assumed that the friction factor in the laminar flow regime is consistent with known fundamental solutions. In this case, pressure losses are caused by accelerating the flow in front of the cavity and decelerating it behind it. However, the variation of the pressure loss and friction factor depending on  $Re_{Dh}$  remains similar to its change in rough pipes (Moody, 1944), though, at the same time, the transition from laminar to fully developed turbulent flow is more prolonged.

The effect of filling the cavity with roughness elements is much more complicated, although, in terms of size, it is smaller than the impact of ramps alone. In all cases, the smallest friction factor values are found for the case of the plain cavity. Any insertion of roughness elements into the cavity increases the pressure losses up to a certain threshold level. When parameter  $\lambda$  changes from 8.8 (plain cavity) to 4.7 (1 roughness element) and 3.3 (2 elements), the friction factor increases consistently for the flow separation from every vertex of roughness elements and the formation of vortices between individual roughness elements. This last phenomenon is similar to that which occurs in the case of flow over a separate open-type cavity.



**Fig. 41** Friction factor dependence on  $Re_{Dh}$  for different roughness element configurations

However, further increasing roughness elements number up to 3, when  $\lambda = 2.8$ , pressure losses decrease. In this case, critical spacing between roughness elements is reached. As Choi et al. (Choi et al., 1993) explained, specific spacing of roughness elements reduces viscous drag by restricting the location of streamwise vortices. Therefore, only the tip region of the roughness elements is exposed to a high wall-shear rate layer, thus reducing pressure losses. Bechert et al. (Bechert et al., 1997) supplemented this statement, assuming that roughness elements impede the fluctuating turbulent crossflow, thus reducing momentum transfer and shear stresses. A logical conclusion can be drawn that by increasing the number of roughness elements (decreasing subcavities size), pressure losses will further decrease, approaching their asymptotical values.

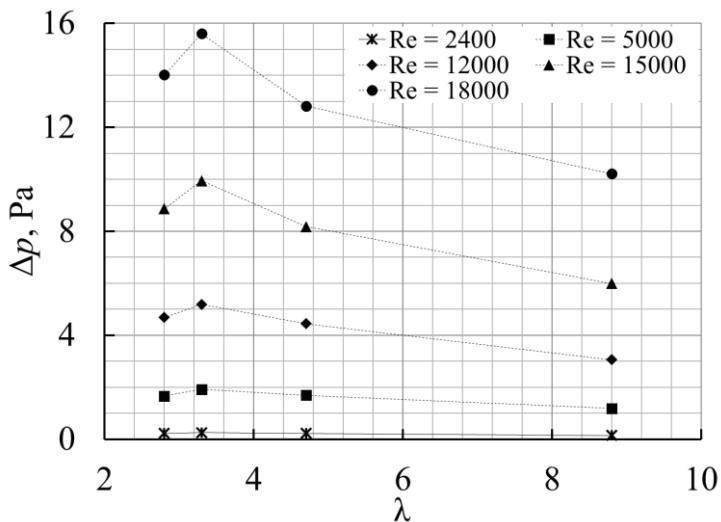
The data presented in Fig. 41 and Fig. 42 also show that in a turbulent flow regime, friction factor and pressure drop values vary more consistently with the values of the parameter  $\lambda$  than in a laminar flow regime. It should be noted that  $\lambda = 8.8, 2.8$ , and fully covered cavity cases provide very close friction factor values in the laminar flow regime ( $Re \leq 2400$ ). When  $Re_{Dh}$  reaches 2400, the transition from laminar to transitional flow regime occurs, as observable in the friction factor trend (Fig. 41). At this point, a friction factor increase is observed. The increase is more abrupt and significant compared to the case of rough pipe (Moody, 1944).

As shown in Fig. 42, in all  $Re_{Dh}$  numbers investigated, peak pressure drop and friction factor are observed when  $\lambda = 3.3$  (two roughness elements installed). As  $\lambda$  increases (the number of subcavities decreases), pressure drop decreases up to 12% depending on  $Re$ ; also, the decline rate increases as  $Re_{Dh}$  increases. At  $Re_{Dh} \leq 2400$ ,

pressure drop and friction factor are nearly constant for all roughness element configurations.

Depending on roughness element configurations, pressure drop regularity may be explained based on recirculation bubble behaviour in different subcavities sizes. It may be stated that in the case of the plain cavity, a recirculation zone is formed behind the ramp, and the separated shear layer reattaches at a certain distance on the bottom wall. As roughness elements are presented and the distance between them reaches a critical value, there are no conditions for the formation of reattachment to the cavity bottom. Whether or not a separated flow is reattached to the bottom wall depends on the distance between roughness elements. As more roughness elements are presented, the distance between them decreases, causing the formation of a situation analogous to flow over a conventional open-type cavity, where the interaction of vortices in the cavity with external flow becomes weak.

In the present case, the subcavity depth is constant; however, the length of it is changing. As explained, the pressure drop is determined by recirculation zone interaction with the main flow. The size and intensity of the recirculation zone, in this case, is determined by flow velocity and subcavity length. Therefore, the length of the subcavity may be considered as a critical parameter determining pressure losses along the roughness elements. As explained, after the cavity length-to-depth ratio ( $\lambda$ ) reaches the critical value, the changes of interaction between the recirculation zone and main flow reduce pressure losses. A relative cavity length-to-depth ratio should be considered a crucial parameter determining pressure losses if all other parameters are constant.



**Fig. 42** Pressure drop dependence on different configurations of roughness elements at different  $Re_{Dh}$

## CONCLUSIONS

By means of flow visualisation and measurements of its statistical parameters, the factors of active and passive flow control methods determining the uniformity and stability of velocity distribution and internal flow structure were experimentally and numerically analysed in open-, transitional-, and closed-type cavities. After investigating three flow control methods, namely pulsatile flow, implementation of roughness elements, and alteration of cavity geometrical parameters, the following conclusions are made:

1. In laminar and transitional flow regimes, the recirculation zone length and flow structure are decided by pulsation amplitude and frequency:
  - 1.1. In laminar and transitional flow regimes, the recirculation zone length is reduced by pulsatile flow. In a laminar flow regime, the intensity of this effect is inversely proportionate to pulsation amplitude. The highest reduction of the recirculation zone length was achieved ~45% in the transitional-type cavity at  $Re_{h1} = 250$  and  $A = 0.15$ .
  - 1.2. The influence of pulsation frequency in the investigated range of  $f = 0.5 - 5$  Hz did not exceed 6 %. Since the magnitude of this effect was lesser than the measurement uncertainty – the pulsation frequency to recirculation zone length is considered negligible.

In the turbulent flow regime, the effect of the pulsations becomes insignificant as the recirculation zone length becomes independent of the flow parameters and reaches its asymptotical value.

2. The discrepancies of recirculation zone length values in cases with different pulsation frequencies at acceleration and deceleration phases are determined by different recirculation zone responses to the pulsation period. A pulsatile flow case with  $f = 5$  Hz is observed to have a 5% delayed development of the recirculation zone (~15° phase angle-wise) compared to the case with  $f = 1$  Hz. The same regularities apply to the development of the corner vortex during the pulsation cycle.
3. In a transitional flow regime, pulsations tend to increase turbulence intensity within the cavity due to the magnified interactions of periodically recurring vortices. However, in turbulent flow regimes, turbulence intensity within the cavity is determined by the velocity fluctuations caused by turbulent flow itself, as the velocity fluctuations caused by pulsations are negligible. Therefore, the almost identical turbulence intensity distribution is observed in every investigated pulsatile parameter case.
4. The configuration of cavity inner corners, expressed by the ratio  $R/h_1$ , has no impact on the flow dynamics and structure; however, the outlet-to-inlet hydraulic diameter ratio significantly impacted it. The longitudinal velocity distribution is determined by the separated shear layer as it restricts the main flow core from expanding and ensures uniform distribution of its velocity until

$x/L = 0.8$ . When  $x/L > 0.8$ , the longitudinal velocity is inversely proportionate to  $D_{h\_out}/D_{h\_in}$ . As the ratio increases by 10%, the longitudinal velocity at the cavity outlet decreases up to 13% and vice versa.

5. Decreasing the length between roughness elements increases pressure losses until the critical size of subcavities between roughness elements is reached ( $\lambda = 3.3$ ). Before the critical size is reached ( $\lambda > 3.3$ ), the shear layer separates from the vertices of roughness elements, and the recirculation zone is formed behind them. Exceeding the critical size of subcavities, the large vortices are not formed, causing the pressure losses to reduce by up to 12%. As the size of subcavities decreases, the flow is less affected by the shear layer separated from roughness elements vertices; therefore, the fluid flows through the cavity with lesser energy losses.

## 4. SANTRAUKA

### ĮVADAS

Srauto atitrūkimo procesai kanaluose su staigiais skerspjūvio pokyčiais dažnai sutinkami energetikos inžinerijoje (Chen et al., 2018). Atitrūkusio srauto reiškinys analizuojamas srautų dinamikos, šilumos mainų, kietųjų dalelių pagavimo tyrimų srityse (Faure, 2014, Shen et al., 2015, 2017, Wang et al., 2022), kuriose išryškintos tos pačios problemos – srauto nestabilumas, turbulentiškumas, atitrūkstančių sukurių sistemos ir panašūs nepageidaujami procesai, kurie reikalauja kontrolės, siekiant užtikrinti fluidų sistemų našumą, pagerinti energijos perdavimo efektyvumą ir stabilizuoti šilumos mainų procesus. Srauto valdymo metodų poreikis atsiranda dėl neišvengiamo fluideo elgsenos sudėtingumo, todėl pastarieji susilaukia daug tyrėjų dėmesio ir yra sparčiai tobulinami (Joshi et al., 2016).

Srauto atitrūkimo procesą lemiantys veiksniai dažniausiai tiriami panaudojant srautų vizualizacijos metodą (PIV), kuris leidžia atlikti tikslius srauto struktūros matavimus, nedarant jokio poveikio tekančiam fluidui. Srautų vizualizacijos metodai praktikoje dažnai derinami su skaitiniais modeliavimo metodais, kurie leidžia praplėsti tyrimų galimybes ir tokiu būdu suteikia galimybę nuodugnai ištirti srauto struktūrą bei dinamiką lemiančius veiksnius. Kompleksinis skaitinio modeliavimo ir srautų vizualizacijos metodų taikymas taip pat dažnai sutinkamas tiriant srauto valdymo metodų efektyvumą lemiančius veiksnius (Wong et al., 2008, Vanierschot et al., 2014, Bardera et al., 2021, Fan et al., 2022).

Pastaruoju metu plačiai tyrinėjami įvairūs aktyvūs srauto valdymo metodai, įskaitant sintetinius purkštukus, elektromagnetinį forsavimą, priverstines srauto osciliacijas, pulsacinį srautą ir kt. (Chen et al., 2022). Literatūroje nurodoma, jog vienas iš efektyviausių srauto valdymo metodų yra pulsuojančių srauto sąlygų taikymas, kai varijuojamas tekančio fluideo slėgis (McEvoy et al., 2019). Pagal atliktą literatūros analizę galima teigti, jog pulsuojančio srauto įtaka šilumos mainams – dažnai sutinkama tyrimų tema, tačiau buvo pastebėtas trūkumas tyrimų, susijusių su pulsuojančio srauto įtaka atitrūkusio srauto struktūrai ir dinamikai.

Praktikoje, siekiant kontroliuoti srautą, dažniausiai pirmenybė teikiama pasyviems srauto valdymo metodams dėl šiems metodams būdingo paprastumo. Vienas pagrindinių metodų pasyviai valdyti srautą – panaudoti periodiškai atsikartojantį reljefą imituojančias dvimates kliūtis, kurios literatūroje vadinamos šiurkštumo elementais (Zhang et al., 2010). Pastarųjų panaudojimas pasižymi galimybe valdyti atitrūkusį srautą, geometriškai jį apribojant, tokiu būdu išvengiant nepageidautinos srauto elgsenos. Srauto charakteristikos gali būti kontroliuojamos keičiant kanalo geometrinius parametrus, tokiu būdu didinant srauto stabilumą (Bravo et al., 2000, Bentaleb et al., 2012, Das et al., 2016).

Tyrimai, atlikti kontroliuojamo atitrūkusio fluideo srauto tematikoje, suteikia neabejotinai reikalingas fundamentines žinias, kurios suteikia galimybę, eliminuojant



nepageidautiną srauto elgseną, pagerinti fluidų sistemų našumą bei sumažinti energijos nuostolius.

### **Tyrimo objektas**

Atitrūkusio srauto dinamika ir struktūra kanaluose su staigiais skerspjūvio pokyčiais.

### **Darbo tikslas**

Darbo tikslas – eksperimentiniais ir skaitiniais metodais ištirti pulsacijomis, šiurkštumo elementais ir geometriniais parametrais valdomą srautą, kartu nustatant parametrus lemiančius recirkuliacinės zonos dinamiką ir atitrūkusio srauto struktūrą kavernoje.

### **Darbo uždaviniai**

Darbo tikslui pasiekti iškelti šie uždaviniai:

1. Nustatyti pulsacijų dažnio ir amplitudės įtaką laike vidutiniam recirkuliacinės zonos ilgiui kavernoje, esant skirtingiems tekėjimo režimams.
2. Nustatyti recirkuliacinės zonos formavimosi ir vystymosi dėsningumus pulsacinio ciklo metu kavernoje.
3. Nustatyti pulsuojančio srauto įtaką srauto turbulentiniam intensyvumui kavernoje.
4. Nustatyti kavernos geometrinių parametru, tokių kaip vidinio kampo konfigūracija ir ištekėjimo/įtekėjimo hidraulinių diametru santykio, įtaką greičio pasiskirstymui kavernoje.
5. Nustatyti šiurkštumo elementų ir kavernos geometrinių parametru įtaką greičio pasiskirstymui ir slėgio nuostoliams kavernoje.

### **Ginamieji teiginiai**

1. Pulsuojantis srautas trumpina recirkuliacinės zonos ilgį laminariniame ir pereinamajame tekėjimo režimuose, o šio efekto intensyvumas, laminariniame tekėjimo režime, yra atvirkščiai proporcingas pulsacijų amplitudei.
2. Recirkuliacinės zonos vystymąsi pulsacinio ciklo metu nulemia recirkuliacinės zonos atsakas į pulsacijos periodą, kuriam mažėjant matomas recirkuliacinės zonos vystymosi vėlavimas.
3. Pulsuojančio srauto sukeltos greičio fluktuacijos yra reikšmingos srauto turbulentiškumui iki kol pasiekiamas turbulentinis tekėjimo režimas.
4. Kavernos vidinių kampų užapvalinimas srauto struktūrai ir dinamikai įtakos nedaro, tačiau didelę įtaką turi kavernos ištekėjimo ir įtekėjimo hidraulinių diametru santykis, kurio įtaka išilginiam greičiui kavernos centre pasireiškia fluidui artėjant prie kavernos priekinio laipto.
5. Slėgio nuostoliai kavernoje atvirkščiai proporcingi atstumui tarp šiurkštumo elementų iki tol, kol pasiekiamas kritinis atstumas tarp jų.

## **Mokslinis naujumas**

Papildytos fundamentinės žinios apie srauto valdymo metodus, leidžiančios nusakyti srauto valdymo įtaką vidutinei atitrūkusio srauto struktūrai, nustatyti papildomų sukurių, t.y. viršutinių ir kampinių sukurių, dinamikos dėsninumus, apibrėžti srauto valdymo efektyvumą lemiančius veiksnius ir nustatyti greičio fluktuacijų kilmę, esant skirtingiems tekėjimo režimams.

## **Praktinė vertė**

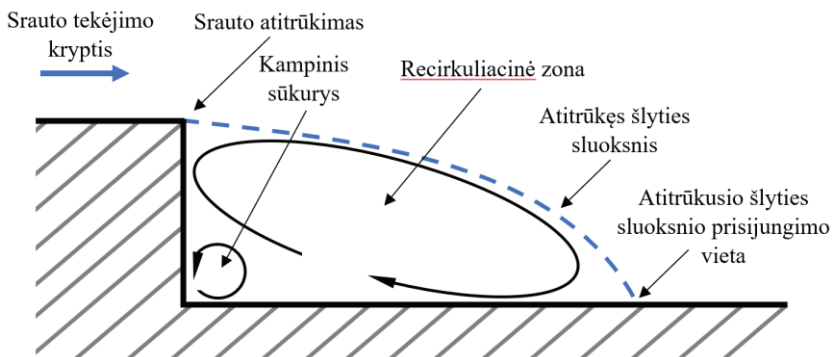
Aktyvių srauto valdymo tyrimų praktinę vertę sudaro potencialas padidinti fluidų sistemų efektyvumą, dėl kurio pagerėtų termoinžinerinių procesų našumas ir sumažėtų energijos suvartojimas. Šiuo darbu taip pat papildytos žinios apie pasyvius srauto valdymo metodus, kurie potencialiai gali dar labiau sumažinti išlaidas, susijusias su įvairiomis inžinerinėmis sistemomis, kadangi šie metodai nereikalauja išorinių energijos šaltinių. Be to, atitrūkusio ir pulsuojančio srauto kombinacija dažnai pasitaiko biomedicinos srityje, kur fundamentinės žinios apie srauto valdymą neabejotinai reikalingos, siekiant tobulinti mikrofluidines sistemas

## **Mokslinė sklaida**

Disertacijoje pateikti rezultatai buvo publikuoti 4 moksliniuose žurnaluose, kurie turi citavimo indeksą ir yra referuojami “Clarivate Analytics” “Web of Science” duomenų bazėse. Rezultatai taip pat pristatyti 3 tarptautinėse konferencijose.

#### 4.1. Literatūros apžvalga

Literatūroje srauto atitrūkimo procesas dažniausiai tiriamas kanaluose su atgaliniu laiptu, dėl itin paprastos geometrijos ir plataus pritaikymo fundamentiniuose ir inžineriniuose uždaviniuose (43 pav.). Atgalinio laipto aptekėjimo tyrimai neapsiriboja vien atitrūkusio srauto reiškiniiais. Srautas tokio tipo kanale pasižymi ir sudėtingais tekėjimo režimų pokyčių procesais, įvairiais nestabilumais ir sudėtinga atitrūkstančių sukurių sistema, esant pereinamajam ir turbulentiniam tekėjimo režimams (Chen et al., 2018).



43 pav. Atgalinį laiptą aptekančio srauto struktūros schema

Staigūs kanalo skerspjūvio pokyčiai sukelia slėgio gradientą, kuris nulemia recirkuliacinės zonos susidarymą. Literatūroje recirkuliacinės zonos ilgio kitimo dėsningumai priklausomai nuo tekėjimo režimo yra žinomi (Armalý et al., 1983, Tihon et al., 2012). Esant laminariniam tekėjimo režimui, recirkuliacinės zonos ilgis tiesiogiai priklauso nuo  $Re$ . Esant mažiems  $Re$ , recirkuliacinės zonos ilgio beveik tiesinę priklausomybę nuo  $Re$  nulemia pagrindinio ir atitrūkusio srauto tarpusavio sąveika. Pereinamojo tekėjimo režimo metu, recirkuliacinės zonos ilgis pradeda trumpėti dėl šlyties sluoksnyje atsirandančių nestabilumų, kurie atsiranda dėl pereinamajam ir turbulentiniam tekėjimo režimams būdingos atitrūkstančių sukurių sistemos susidarymo, kai už atgalinio laipto periodiškai susidaro sukuriai, kurie pasiekę tam tikrą dydį atitrūksta ir juda srauto kryptimi (Vilkinis et al., 2018). Pasiekus turbulentinį tekėjimo režimą, recirkuliacinės zonos ilgis pasiekia asimptotinę vertę ir nebe priklauso nuo  $Re$ .

Šie recirkuliacinės zonos ilgio kitimo dėsningumai galioja ir fluido srauto tekėjimams kavernoje, kai srautas papildomai veikiamas priekinio laipto (Vilkinis et al., 2020). Pagal kavernos ilgio ir laipto aukščio santykį priimta klasifikuoti kavernas į tris grupes: atviro tipo ( $L/h_1 < 6-8$ ), pereinamojo tipo ( $8 < L/h_1 < 12$ ) ir uždarojo tipo ( $L/h_1 > 12$ ) (Tracy et al., 1997). Priekinis kavernos laiptas įneša į srautą papildomų nestabilumų, kuris gali būti valdomas aktyviais ir pasyviais metodais.

Kaip vienas efektyvesnių aktyvių srauto valdymo metodų, išskiriamos srauto pulsacijos (McEvoy et al., 2019). Yra žinoma, jog pulsuojantis srautas pagerina šilumos perdavimo procesus dėl sukeliama intensyvesnio fluido maišymosi kanaluose (Brereton et al., 2006, Persoons et al., 2012, Ward et al., 2015). Pulsuojantis srautas pasižymi didesniu šlyties greičiu ant kanalo sienos, kas indikuoja apie intensyvesnį atgalinį srautą recirkuliacinėje zonoje (Valencia, 1997, Valencia et al., 1997). Taip pat, pulsacijos daro įtaką ir atitrūkusio srauto struktūrai, sutrumpindamos už atgalinio laipto susidariusios recirkuliacinės zonos ilgį (Tihon et al., 2010, 2012). Užtikrinant specifines pulsacijų parametrų vertes galima paveikti ir recirkuliacinės zonos vystymąsi, tačiau iki šiol tokie tyrimai buvo atlikti tik kanaluose su atgaliniu laiptu ir atviro tipo kavernoze (Ibrahim et al., 1994, Valencia et al., 1997, Zhang et al., 2022).

Alternatyvus srauto valdymo būdas yra panaudojant šiurkštumo elementus. Šis pasyvus srauto valdymo metodas pasižymi stipriu poveikiu srauto struktūrai ir šilumos mainų procesams (Zhang et al., 2010, 2018, Pelević et al., 2016). Literatūroje nurodoma, jog du pagrindiniai parametrai apsprendžiantys šiurkštumo elementų įtaką srautui yra atstumas tarp šiurkštumo elementų ir jų aukštis (Hu et al., 2003, Rawool et al., 2006, Coleman et al., 2007, Lalegani et al., 2018). Tačiau aukštesni ir tankiau išdėstyti šiurkštumo elementai pasižymi didesniais slėgio nuostoliais, todėl siekiant to išvengti reikalingas specifinis atstumas tarp šiurkštumo elementų, kuris užtikrina optimalias tekėjimo sąlygas (Hu et al., 2003, Rawool et al., 2006, Lalegani et al., 2018).

Siekiant užtikrinti tolygesnį greičio kavernoze pasiskirstymą, yra taikomos įvairios geometrijos modifikacijos. Kavernos tipo kanaluose keičiant laiptų užapvalinimą, išreiškiamą santykiniu dydžiu  $R/h_1$ , gali būti pasiektas stabilesnis tekėjimas, pasižymintis mažesnėmis slėgio osciliacijomis (Bentaleb et al., 2012). Fluido srautas tolygiau apteka apvalintus kampus, taip užtikrinant stabilesnį srauto atitrūkimą ir mažesnius Reinoldso įtempius (Bravo et al., 2000, Kumar, 2017). Turbulentinio tekėjimo metu, apvalinto kampo aptekėjimas lemia intensyvesnius šilumos mainų procesus (Kumar et al., 2018).

Atlikus literatūros analizę pastebėta, jog atitrūkusio srauto dinamika dažniausiai tiriama kanaluose su atgaliniu laiptu arba atviro tipo kavernoze, kur pagrindinis dėmesys skiriamas įvairiems nestabilumams arba šilumos mainams. Tiriant fluido srauto valdymo metodus, autoriai daugiausia dėmesio skiria veiksniams susijusiems su šilumos mainų intensyvinimo uždaviniu, o srauto struktūros ir statistinių srauto parametrų pokyčiams skiriama nepakankamai dėmesio. Taip pat, atlikus literatūros analizę pastebėta, jog valdomo fluido srauto tyrimų kavernoze yra nedaug, o pastarieji atlikti tik atviro tipo kavernoze. Tai sukelia natūralų poreikį tyrimams kitų tipų kavernoze, kur skiriasi priekinio laipto įtaka, priklausomai nuo santykinio kavernos ilgio.

Atsižvelgus į atliktą literatūros analizę, suformuotas pagrindinis šio darbo tikslas – eksperimentiniais ir skaitiniais metodais ištirti srauto valdymo metodų įtaką

srauto dinamikai ir struktūrai kavernoje ir nustatyti srauto valdymo efektyvumą lemiančius veiksnius. Šiuo darbu papildytos fundamentinės žinios apie srauto valdymą, panaudojant pulsacijas, šiurkštumo elementus ir kavernos geometrinius parametrus. Ištirta šių srauto valdymo metodų įtaka srauto struktūrai ir recirkuliacinės zonos ilgio kitimo dėsningumams ir pateikti šių metodų efektyvumą lemiantys parametrai. Atskleistos recirkuliacinės zonos vystymosi tendencijos pulsacinio ciklo metu yra susietos su vidutine atitrūkusio srauto struktūra, tokiu būdu paaiškinant viršutinių ir kampinių sūkurių, atsiradimo priežastis ir dėsningumus. Nustatyta pulsacijų įtaka srauto turbulentiškumui kavernoje, kuris atskleidžia greičio fluktuacijų atsiradimo priežastis, esant pereinamajam ir turbulentiniam tekėjimo režimams. Nustatytos greičio pasiskirstymo ir slėgio nuostolių kavernoje priklausomybės nuo šiurkštumo elementų išdėstymo, kurios suteikia galimybę apibrėžti pasyvaus fluidų valdymo metodo efektyvumą lemiančius veiksnius. Ištirta geometrinių parametrų įtaka greičio pasiskirstymui kavernoje, apibrėžiant pastarųjų įtaką ir pateikiant priklausomybes.

## **4.2. Tyrimų metodika ir įranga**

### **4.2.1. Eksperimentiniai tyrimo metodai**

Fluido srauto greičio vektorių laukai buvo išmatuoti naudojant srautų vizualizacijos metodą (angl. Particle Image Velocimetry, toliau tekste PIV). Tai optinis metodas, skirtas fluido srautui vizualizuoti. Šio darbo eksperimentiniams matavimams buvo naudojami du PIV eksperimentiniai įrenginiai, mikro ir makro skalėse. Abejuose įrenginiuose veikimo principas toks pats – lazerio sužadintų indikacinių dalelių poslinkis fiksuojamas kamera, taip išmatuojant fluido srauto greičio vektorių laukus. Įrenginiuose naudojamas lazeris ir kamera, sinchronizatoriaus pagalba, suderinti taip, kad veiktų 15 Hz dažniu. Kaip galutinis matavimo rezultatas gaunamas greičio vektorių laukas iš kurio vėliau skaičiuojami papildomi parametrai. Vidutiniai greičio vektorių laukai buvo gaunami 200-220 kadru vidurkio. Eksperimentų metu aplinkos temperatūra buvo užtikrinta  $20 \pm 1^\circ\text{C}$ .

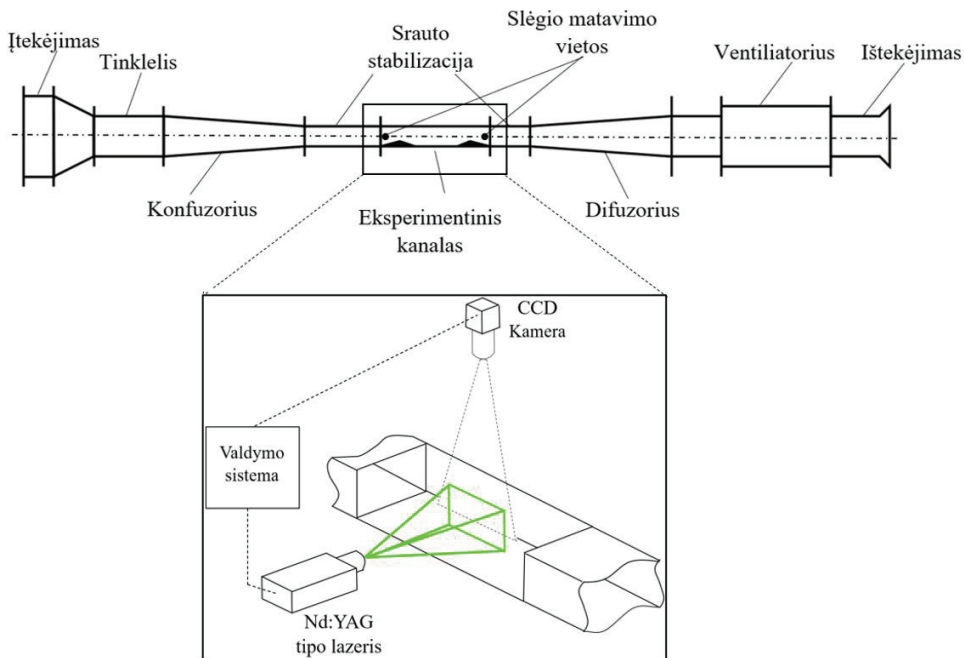
#### **4.2.1.1. PIV įrenginys**

Disertacinio darbo metu naudotas PIV įrenginys (44 pav.) susideda iš Nd:YAG tipo lazerio Dual Power 200-15 (Dantec Dynamics) ir FlowSense EO 4 Mpx CCD kameros (Dantec Dynamics). Eksperimentų metu gautoms nuotraukoms apdoroti buvo naudojamas DynamicStudio programinis paketas (Dantec Dynamics). Eksperimentams naudojamos indikacinės dalelės buvo sugeneruotos iš cukraus tirpalo, naudojant dalelių generatorių Jet Atomizer 9306 (TSI). Šio įrenginio sugeneruotų dalelių tankis –  $1,58 \times 10^3 \text{ kg/m}^3$ , o vienos dalelės diametras  $0,3 \mu\text{m}$ . Oro sraute esančios kietosios dalelės relaksacijos periodas buvo  $4 \times 10^{-7} \text{ s}$ , kuris užtikrina Stokso skaičių  $\text{Stk} \ll 1$  ir lėmė tolygų kietųjų dalelių judėjimą pagal srauto linijas. Fluido srautas buvo sukurtas naudojant ventiliatorių, o greitis naudojamas  $\text{Re}$

skaičiavimams išmatuotas termoanemometru Testo 435, kurio matavimo ribos (0 – 20 m/s), o matavimo neapibrėžtis (14,3 – 0,5 %).

Vaizdų analizė buvo atlikta panaudojant adaptyviosios koreliacijos algoritmą, kur maksimalus ir minimalus dalelių poslinkiui sugeneruoto tinklelio lango dydis buvo  $473,6 \times 177,6 \mu\text{m}$  ir  $177,6 \times 88,8 \mu\text{m}$ , atitinkamai.

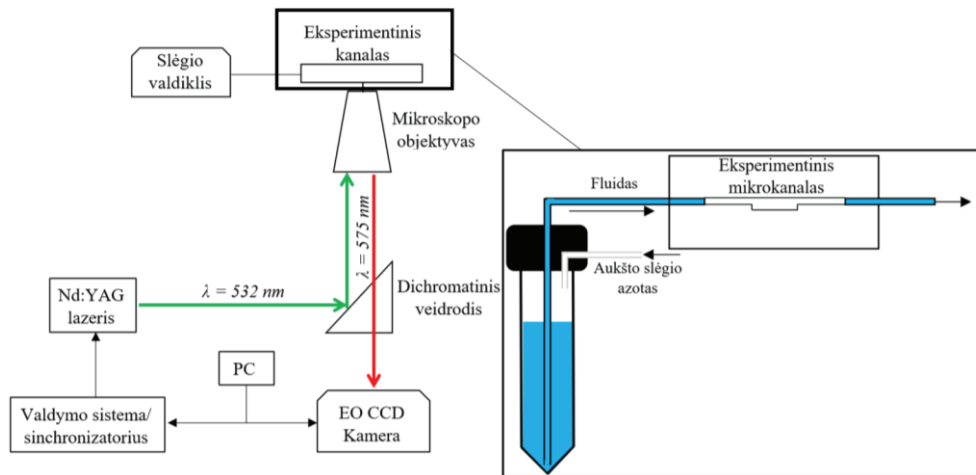
Eksperimentiniai slėgio matavimai buvo atlikti naudojant FCO12 slėgio matuoklį (Furness Controls), kurio matavimo ribos 0-20 Pa, o matavimo neapibrėžtis neviršija 0,5%. Slėgis buvo matuojamas prieš ir už eksperimentinio kanalo, taškuose esančiuose 460 mm atstumu vienas nuo kito.



44 pav. PIV įrenginio schema

#### 4.2.1.2. $\mu$ PIV įrenginys

$\mu$ PIV įrenginyje (45 pav.) kaip darbinis fluidas buvo naudojamas dejonizuotas vanduo su fluorescencinėmis dalelėmis, kurių diametras  $1 \mu\text{m}$ . Fluido srautas buvo sukurtas panaudojant OB1 MK3 slėgio valdiklį (Elveflow), kurio dėka eksperimentinio kanalo įtekėjime buvo sukurtas slėgis iki 8 bar(g).  $\mu$ PIV įrenginys taip pat susideda iš Nd:YAG tipo lazerio ir 4 Mpx FlowSense kameros, kuri įtaisyta prie Leica DM ILM invertuoto mikroskopo (Leica Microsystems). Kameros pikselio dydis  $7,4 \times 7,4 \mu\text{m}$ .



45 pav.  $\mu$ PIV įrenginio schema

#### 4.2.1.3. Matavimų neapibrėžtis

Greičio matavimų neapibrėžtis buvo nustatyta įvertinus slėgio valdiklio ar ventiliatoriaus generuojamo srauto, kanalo skerspjūvio matmenų, koreliacijos skaičiavimo dėl pasirinkto laiko tarp kadrių porų ir greičio matavimo atsikartojamumo neapibrėžties dedamąsias. Įvertinus pastarąsias, išplėstinė greičio matavimų neapibrėžtis neviršijo 7%.

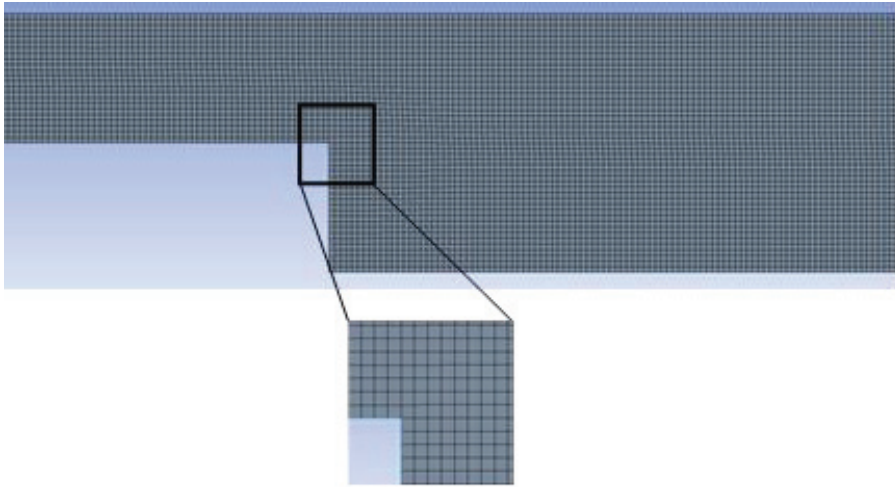
Atitrūkusio šlyties sluoksnio prisijungimo taškas nustatomas pagal minimalią  $u_{x,rms}$  vertę žemiausioje y ašies padėtyje. Ilgis nuo atgalinio laipto iki prisijungimo taško sudaro recirkuliacinės zonos ilgį. Matavimų neapibrėžtį sudarė dedamosios dėl dalelių poslinkio matavimų tinklelio rezoliucijos, greičio matavimo, atitrūkstančių sūkurių sistemos ir matavimų atsikartojamumo, kuris laminariniame tekėjimo režime neviršijo 2,3%, o turbulentiame – 8,9%. Įvertinus visas neapibrėžties dedamąsias, gauta išplėstinė recirkuliacinės zonos ilgio matavimo neapibrėžtis neviršijo 15%.

#### 4.2.2. Skaitinis modeliavimas

Skaitinis modeliavimas buvo atliktas naudojant Ansys Fluent 2019 R2 programinį paketą. Skaičiavimai atlikti naudojant  $k-\epsilon$  ir Reynolds Stress-Omega modelius 2D ir 3D geometrijose. Pulsuojančio srauto atveju buvo naudotas uRANS metodas, leidžiantis modeliuoti srauto elgseną laike.

Siekiant užtikrinti tikslus skaičiavimus, reikalingas smulkus tinklelis, tačiau modeliavimas itin smulkaus tinklelio geometrijose labai padidina reikalaujamų resursų kiekį, todėl reikalinga atlikti tinklelio testą. Šis testas atliekamas sugeneruojant skirtingo dydžio tinklelio akutes ir atliekant skaičiavimus stebint kokia daroma tinklelio įtaka stebimam parametru. Atlikus skaičiavimus su skirtingais tinkleliais nustatomas optimalus tinklelio akutės dydis. 46 pav. pavaizduotas grubus tinklelis, siekiant parodyti sugeneruoto tinklelio struktūros principą. Visais atvejais

skaičiavimai atliekami panaudojant SIMPLE algoritmą ir antro laipsnio diskretizavimo schemas.



46 pav. Struktūrizuoto tinklelio pavyzdys 2D uždarąjo tipo kaverneje

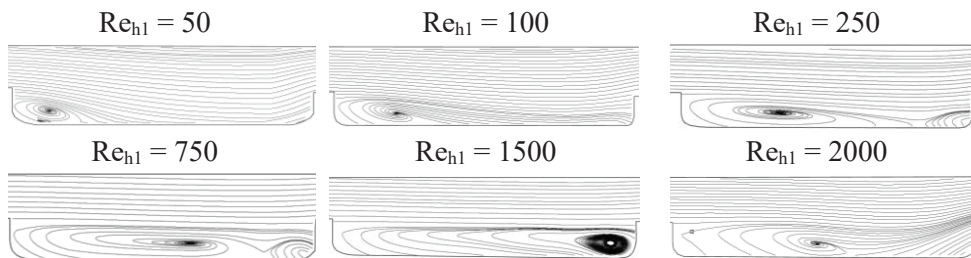
#### 4.3. Tyrimų rezultatai

Šiame skyriuje bus pateikiami, analizuojami ir aptariami visi šio darbo eksperimentiniai ir skaitiniai rezultatai. Šis skyrius suskirstytas į dvi pagrindines dalis, susijusias su aktyviais ir pasyviais srauto valdymo metodais. Aktyvus srauto valdymo metodas realizuojamas panaudojant srauto pulsacijas. Keičiant pulsuojančio srauto parametrus, tiriama recirkuliacinės zonos dinamika ir stebimi statistiniai srauto parametrai, tokie kaip šlyties greitis, turbulentinis intensyvumas ir sūkuringumas, tokiu būdu nustatant srauto valdymą lemiančius veiksnius. Pasyvus srauto valdymas šiame darbe realizuojamas panaudojant šiurkštumo elementus ir keičiant kavėrų geometrinius parametrus, tokius kaip vidinių kampų forma ar įtekėjimo/ištekėjimo hidraulinių diametrų santykis. Panaudojant šiurkštumo elementus, už atgalinio laipto susidaranti recirkuliacinė zona yra suskirstoma į keletą atskirų sūkurių taip apribojant srauto struktūrą nuo didelių sūkurių atsiradimo. Šiurkštumo elementų įtaka srautui tiriama per srauto ir šlyties greičio pasiskirstymą, ir analizuojant slėgio nuostolių priklausomybę nuo  $Re$  ir atstumo tarp šiurkštumo elementų. Taip pat, šiame skyriuje pateikiama geometrinių kavėros parametrų analizė, kurios metu apibrėžta kavėros vidinių kampų formos įtaka srauto struktūrai ir įtekėjimo/ištekėjimo hidraulinių diametrų įtaka išilginio greičio pasiskirstymui kavėroje.



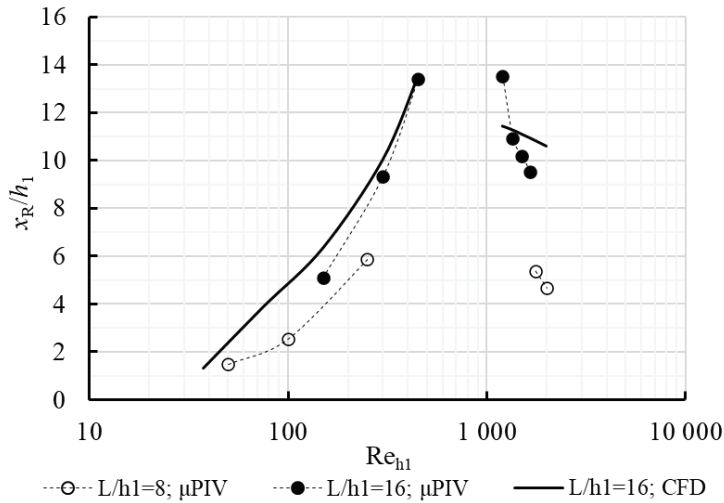
### 4.3.1. Recirkuliacinės zonos dinamika, esant stacionariam tekėjimui kavernoje

Pereinamojo tipo kavernoje vidutinės fluido srauto linijos pateikiamos siekiant pavaizduoti recirkuliacinės zonos dinamiką kavernoje priklausomai nuo tekėjimo režimo (47 pav.).



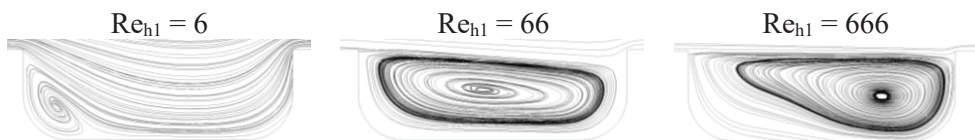
**47 pav.** Srauto linijos pereinamojo tipo kavernoje, esant stacionariam tekėjimui

Laminarinio tekėjimo režimo metu, esant  $Re_{h1} = 50 - 100$ , matomas srauto atitrūkimas dėl slėgio gradientu, kurį sukelia staigus kanalo skerspjūvio išplatėjimas. Atitrūkęs šlyties sluoksnis prisijungia prie kavernos dugno ir matoma už atgalinio laipto susidariusi recirkuliacinė zona. Esant laminariniam tekėjimo režimui, recirkuliacinės zonos ilgis tiesiogiai priklauso nuo  $Re_{h1}$ , todėl esant  $Re_{h1} = 100$ , matoma ~40% ilgesnė recirkuliacinė zona lyginant su  $Re_{h1} = 50$  atveju. Esant  $Re_{h1} = 250$ , atitrūkęs šlyties sluoksnis nebeprisijungia prie kavernos dugno ir recirkuliacinė zona užpildo visą kaverną. Tai indikuoja apie pereinamąjį tekėjimo režimą. Toliau didėjant  $Re_{h1}$  šlyties sluoksnis pakartotinai prisijungia tik esant  $Re_{h1} = 1750$  (48 pav.). Kai pasiekiamas turbulentinis tekėjimo režimas, recirkuliacinės zonos ilgis pasiekia asimptotinę vertę ir nebeprisijungia nuo  $Re_{h1}$ . Recirkuliacinės zonos ilgio kitimo dėsningumai sutampa pereinamojo ir uždarojo tipo kavernoje (48 pav.). Pagrindinis skirtumas tarp šių dėsningumų yra  $Re_{h1}$  ribos, kuriose matomas pilnas kavernos užpildymas recirkuliacine zona. Pereinamojo tipo kavernoje šios ribos yra nuo  $Re_{h1} = 250$  iki  $Re_{h1} = 1750$ , tuo tarpu uždarojo tipo kavernoje –  $Re_{h1} = 450 - 1200$ . Šis skirtumas atsiranda dėl pereinamojo tipo kavernoje arčiau esančio priekinio laipto, kuris apriboja recirkuliacinę zoną ir neleidžia pasiekti didesnių ilgio verčių. Uždarojo tipo kavernoje, dėl mažesnės priekinio laipto įtakos, recirkuliacinė zona pasiekia didesnes ilgio vertes dėl ko pereinamas tekėjimo režimas pasiekiamas vėliau. Pasiekus pereinamojo tekėjimo režimą, recirkuliacinės zonos ilgis pradeda trumpėti dėl šlyties sluoksnyje atsirandančių nestabilumų.



**48 pav.** Recirkuliacinės zonos ilgio priklausomybė nuo  $Re_{h1}$  pereinamojo ir uždarojo tipo kavernoje su  $L/h_1 = 8$  ir  $L/h_1 = 16$ , atitinkamai

49 pav. pavaizduotos skaitinio modeliavimo metodu gautos srauto linijos atvirojo tipo kavernoje. Šio tipo kavernoje recirkuliacinės zonos ilgis tampa necharakteringu dydžiu, nes atitrūkęs šlyties sluoksnis prisijungia prie kavernos dugno tik esant labai mažiems  $Re_{h1}$ . Laminariniam tekėjimo režime recirkuliacinei zonai būdinga stabili elgsena, kuri pasireiškia stabiliu greičio pasiskirstymu kavernoje. Esant  $Re_{h1} = 66$ , šlyties sluoksnis neprisijungia prie kavernos dugno ir pagrindinis srautas prateka virš kavernos. Esant  $Re_{h1} = 666$ , matomas recirkuliacinės zonos centro pasislinkimas link priekinio laipto. Kaip ir pereinamojo bei uždarojo tipo kavernoje, toliau augant  $Re_{h1}$  srauto struktūra kavernoje nesikeičia.



**49 pav.** Srauto linijos esant stacionariam tekėjimui atvirojo tipo kavernoje ( $L/h_1 = 4$ )

### 4.3.2. Aktyvus srauto valdymas

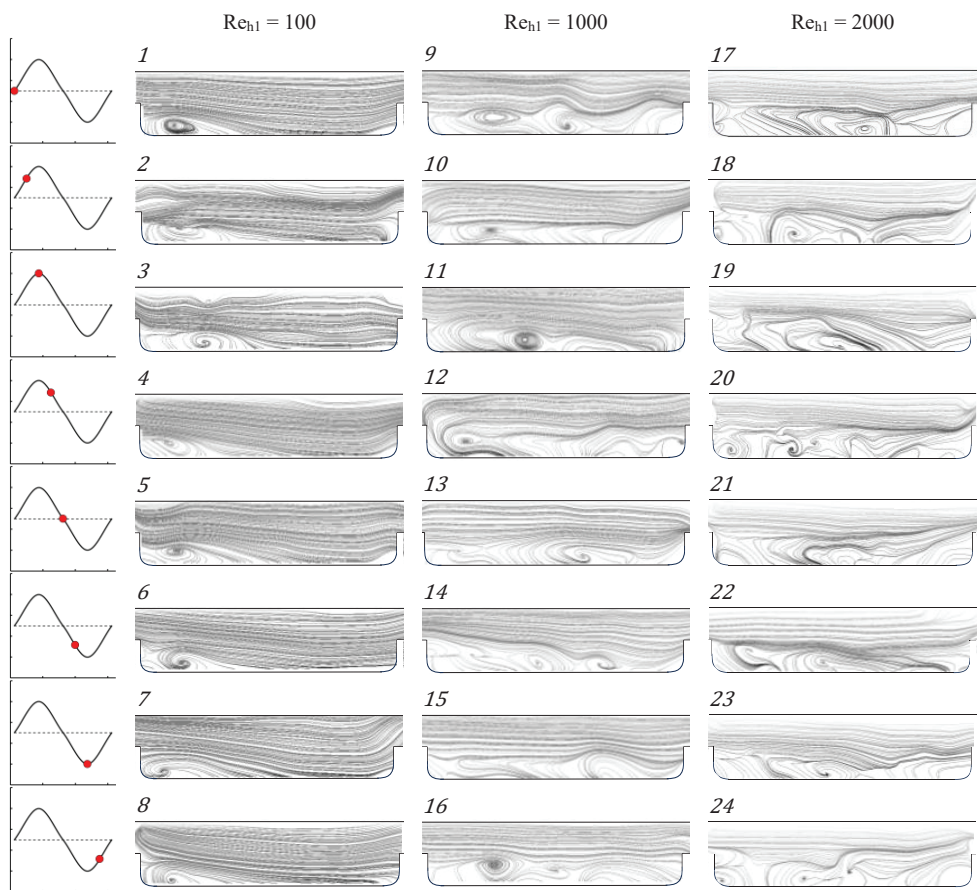
Šioje dalyje analizuojama recirkuliacinės zonos dinamika pereinamojo ir uždarojo tipo kavernoje, priklausomai nuo pulsacijų dažnio ir amplitudės. Viso šiame darbe tirti 7 pulsuojančio srauto atvejai ir 1 stacionarus (1 lentelė.). Atvejis Nr. 1 atitinka stacionarų tekėjimą, todėl pulsacijų dažnis ir amplitudė nenurodyti.

**1 lentelė.** Tiriamųjų tekėjimo atvejų parametrų vertės

Atvejo Nr.	$A$	$f$ , Hz	$L/h_1$
1	-	-	8; 16
2	0,15	0,5	8
3	0,15	1,0	8
4	0,60	0,5	8
5	0,60	1,0	8
6	1,00	1,0	16
7	1,00	2,0	16
8	1,00	5,0	16

#### 4.3.2.1. Recirkuliacinės zonos elgsena pulsacijų ciklo metu

Pulsacijų ciklo metu recirkuliacinės zonos dinamika priklauso nuo tekėjimo režimo. 50 pav. pateikiamas eksperimentiškai išmatuotų greičio srauto linijų pasiskirstymas pereinamojo tipo kavernoje, esant skirtingoms pulsacijų ciklo fazėms. Laminariniam tekėjimo režime ( $Re_{h1} = 100$ ), dėl pulsacijų ciklo metu varijuojančio greičio, recirkuliacinės zonos ilgis kinta priklausomai nuo pulsacijų ciklo fazės. Taip pat, recirkuliacinės zonos centras pulsacijų ciklo greitėjimo (esant  $0^\circ < \varphi < 90^\circ$  ir  $270^\circ < \varphi < 360^\circ$ ) ir lėtėjimo (esant  $90^\circ < \varphi < 270^\circ$ ) fazėse keičia lokaciją judant srauto kryptimi, kai greitis didėja ir prieš srautą, kada greitis mažėja. Nors recirkuliacinė zona dėl pastoviai kintančio greičio juda ir keičia formą, tačiau pats sukūrys išlieka stabilus. Pasiekus pereinamąjį tekėjimo režimą, pastebimas kitoks recirkuliacinės zonos vystymosi mechanizmas, kai recirkuliacinė zona yra užpildoma periodiškai nuo atgalinio laipto atitrūkstančiais sukūriais. Apatiniame kavernos kampe tarp atgalinio laipto ir pirminio sukūrio pradeda formuotis naujas sukūrys, kuris laikui bėgant didėja ir tuo pačiu stumia pirminį sukūrį pasroviui. Antriniam sukūriui pasiekus kritinį dydį, pirminis pasislenka pasroviui iki kol dėl susidariusių įtempių pirminis sukūrys išsprūsta iš po šlyties sluoksnio ir išlekia iš kavernos. Pereinamojo tekėjimo režimo metu, tam tikrose pulsacijų ciklo fazėse, viename kadre pastebimi du atitrūkę sukūriai (50 pav. 14 ir 16), o pasiekus turbulentinį tekėjimo režimą – trys (50 pav. 20 ir 24). Tai indikuoja apie turbulentinio tekėjimo metu esantį didesnę sukūrių atitrūkimo dažnį. Taip pat, turbulentinis tekėjimo režimas išsiskiria chaotiškesnėmis srauto linijomis, kurios yra dėl tekėjimo režimo atsirandančių greičio fluktuacijų pasekmė.

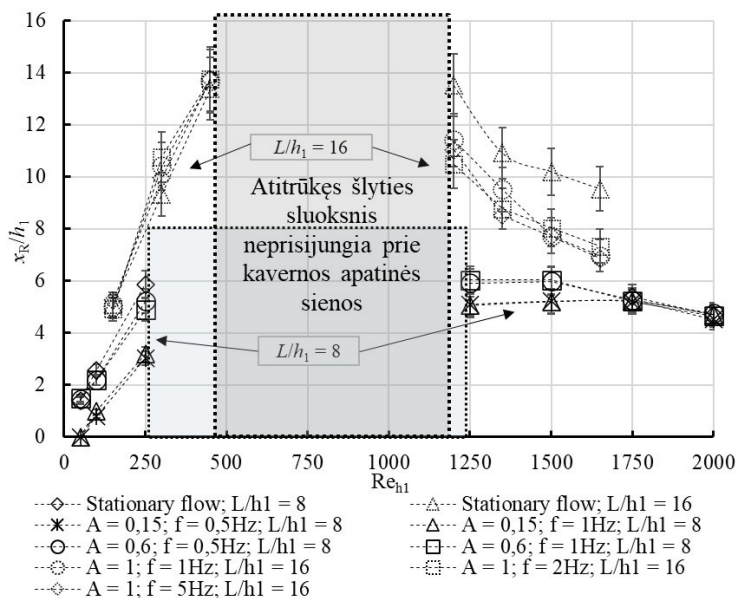


**50 pav.** Srauto linijos pulsacinio ciklo metu pereinamojo tipo kavernoje, esant  $A = 0,60$  ir  $f = 0,5$  Hz

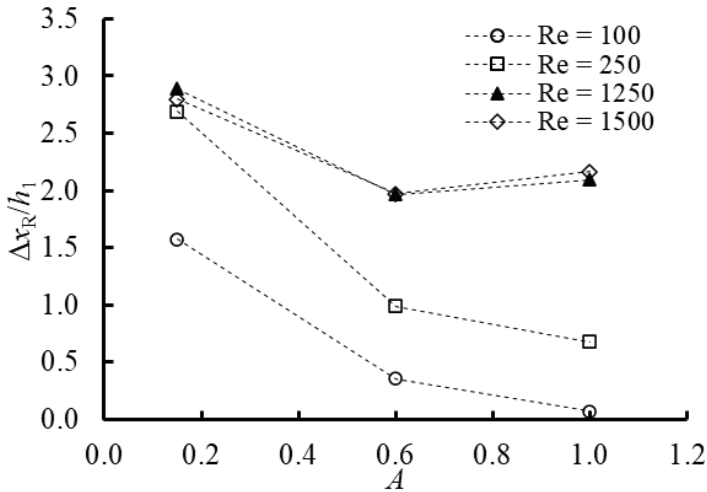
#### 4.3.2.2. Pulsacijų amplitudės įtaka recirkuliacinės zonos dinamikai

Iš 51 pav. pateiktų eksperimentiškai išmatuotų recirkuliacinės zonos ilgio priklausomybių nuo  $Re_{h1}$  galima matyti pulsacijų amplitudės įtaką recirkuliacinės zonos ilgiui. Esant  $Re_{h1} = 50 - 250$ , matomos mažesnės recirkuliacinės zonos ilgio vertės nei stacionaraus tekėjimo metu, dėl pulsacijų metu atsirandančių mažų sukurių šlyties sluoksnyje, kurie nulemia spartesnį šlyties sluoksnio augimą dėl ko sutrumpėja recirkuliacinė zona (Chun et al., 1996). Iš pateiktų rezultatų matosi, jog didesnis trumpėjimo efektas pasiekiamas, esant mažesnei pulsacijų amplitudei ( $A = 0,15$ ). Esant  $A = 0,15$ , tekėjimas pulsacijos ciklo metu išlieka tame pačiame režime, todėl recirkuliacinė zona ilgėja ir trumpėja beveik tiesiškai su ciklo metu didėjančiu ir mažėjančiu greičiu. Kai pulsacijų amplitudė  $A = 0,60$ , dėl sparčiai didėjančio greičio pulsacijų ciklo metu, pasiekiamas pereinamasis tekėjimo režimas, kurio metu recirkuliacinė zona užpildo visą kaverną ir atitrūkęs šlyties sluoksnis nebeprisijungia

prie kavernos apatinės sienos. Dėl šios priežasties pulsuojančio srauto atvejai su didesne amplitude pasižymi didesnėmis recirkuliacinės zonos ilgio vertėmis. Dėl tos pačios priežasties, pereinamojo tipo kavernoje, atitrūkusio šlyties sluoksnio prisijungimas prie apatinės kavernos sienos pereinamajame tekėjimo režime stebimas anksčiau, palyginus su stacionariu tekėjimo atveju (pulsuojančio srauto atvejais  $Re_{h1} = 1250$ , stacionaraus -  $Re_{h1} = 1750$ ). Šie dėsningumai matomi ir uždarojo tipo kavernoje, kai  $Re_{h1} > 1200$ . Pagrindinis skirtumas tarp šių dviejų geometrijų, jog uždarojo tipo kavernoje, esant laminariniam tekėjimo režimui, pulsacijos su  $A = 1,0$  nerodo jokio poveikio recirkuliacinės zonos ilgiui. Skirtumai tarp stacionaraus ir pulsuojančio srauto recirkuliacinės zonos ilgių, esant  $Re_{h1} = 150 - 450$ , menki ir neviršija eksperimentinių matavimų neapibrėžties. Lyginant eksperimentinių matavimų rezultatus dviejų tipų kavernoje, pastebėta recirkuliacinės zonos ilgio pokytis, lyginant stacionarų ir pulsuojantį srautą, yra atvirkščiai proporcingas pulsacijų amplitudei, esant laminariniam tekėjimo režimui (52 pav.). Pereinamajame tekėjimo režime, šis efektas nėra toks stiprus kaip laminariniame, tačiau tendencija panaši. Didžiausias recirkuliacinės zonos trumpėjimo efektas užfiksuotas pereinamojo tipo kavernoje pulsuojančio srauto atveju su  $A = 0,15$ ; esant  $Re_{h1} = 250$ , kur recirkuliacinės zonos ilgis buvo  $\sim 45\%$  trumpesnis už stacionaraus tekėjimo atvejų išmatuotą recirkuliacinės zonos ilgio vertę. Esant pulsuojančio tekėjimo atvejui su  $A = 0,60$ ; šis pokytis buvo  $\sim 17\%$ . Priešingai nei pulsacijų amplitudė, pulsacijų dažnis įtakos recirkuliacinės zonos ilgiui neturėjo, o recirkuliacinės zonos ilgių skirtumai, tarp skirtingo dažnio pulsuojančio srauto atvejų, neviršijo 6%.



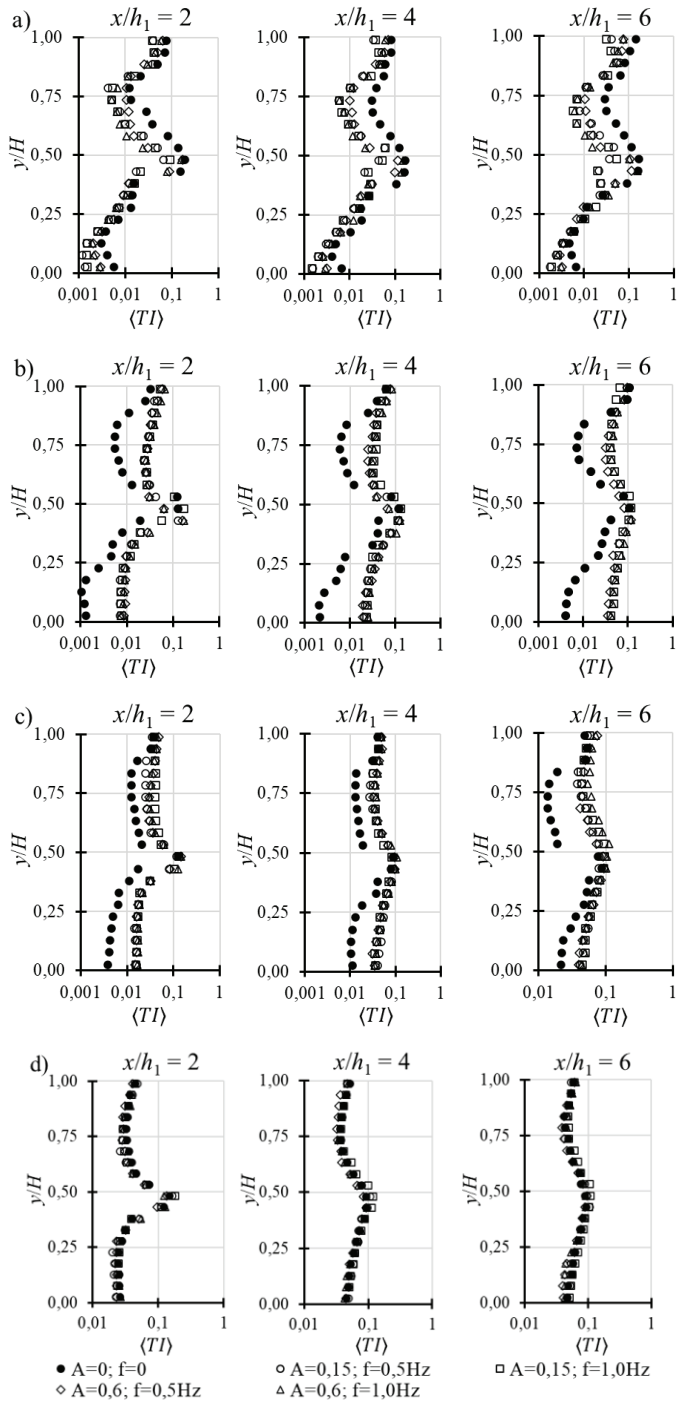
**51 pav.** Recirkuliacinės zonos ilgio priklausomybė nuo  $Re_{h1}$ , esant stacionariam ir pulsuojančiam tekėjimui, pereinamojo ir uždarojo tipo kavernoje



52 pav. Recirkuliacinės zonos pokyčio priklausomybė nuo amplitudės, esant pulsuojančiam tekėjimui

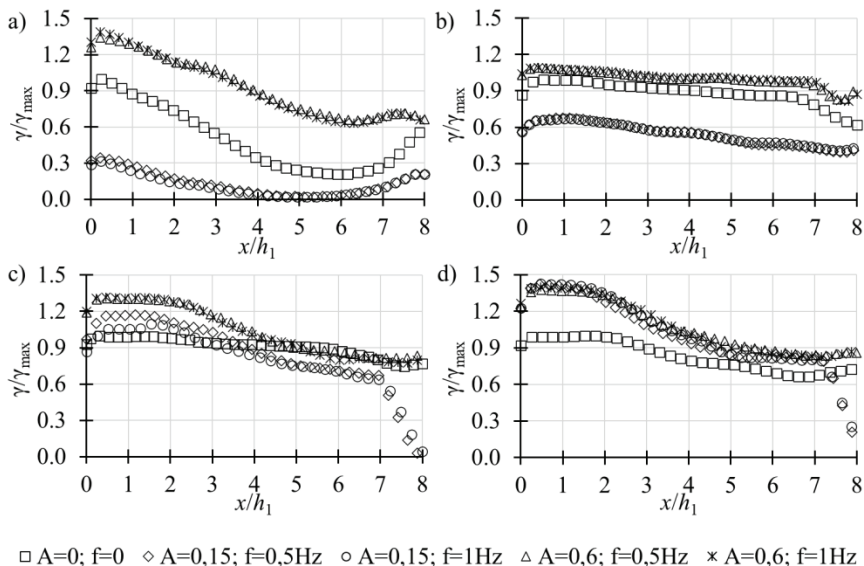
#### 4.3.2.3. Pulsacijų amplitudės įtaka statistiniams srauto parametrams

53 pav. pavaizduoti eksperimentiškai išmatuoti  $\langle TI \rangle$  profiliai skirtingose pereinamojo tipo kaveros lokacijose. Esant  $Re_{hl} = 500$ , matomos mažesnės  $\langle TI \rangle$  vertės pagrindiniame sraute pulsuojančio srauto atvejais. Pulsacijų ciklo metu, kai  $\frac{u(t_i)}{\langle u(t_i) \rangle} < 1$  (esant  $180^\circ < \varphi < 360^\circ$ ), stebimas atitrūkusio šlyties sluoksnio prisijungimas ant kaveros apatinės sienos, dėl ko gaunamas trumpesnis šlyties sluoksnis, kuris lemia stabilesnį tekėjimą. Taip pat, esant  $Re_{hl} = 500$ , srautas yra pereinamajame tekėjimo režime, kuris pasižymi atsirandančiomis greičio fluktuacijomis, todėl pulsacijų ciklo lėtėjimo fazėse (esant  $90^\circ < \varphi < 270^\circ$ ), kai srautas pereina į laminarinį tekėjimo režimą šios fluktuacijos išnyksta. Dėl šių priežasčių pulsuojantis tekėjimas pasižymi mažiausiomis  $\langle TI \rangle$  vertėmis. Kai  $Re_{hl} = 1000 - 1500$  (53 pav. b ir c), matomas visai kitoks  $\langle TI \rangle$  išsidėstymas kavernoje, kada pulsuojantis tekėjimas priešingai nei esant  $Re_{hl} = 500$ , didina  $\langle TI \rangle$  vertes kavernoje. Pulsacijų ciklo metu varijuojantis greitis įneša energiją į pereinamajam ir turbulentiniam tekėjimui būdingą periodiškai atitrūkstančių sukurių sistemą, taip sukeldamas papildomas greičio fluktuacijas ir padidinant  $\langle TI \rangle$  vertes. Turbulentiniame tekėjimo režime, esant  $Re_{hl} = 2000$ , matomas vienodas  $\langle TI \rangle$  išsidėstymas kavernoje, kuris indikuoja, jog  $\langle TI \rangle$  nulemiamas greičio fluktuacijų atsirandančių dėl tekėjimo režimo, o greičio fluktuacijos atsirandančios dėl srauto pulsacijų tampa nereikšmingos, todėl  $\langle TI \rangle$  nuo pulsacijų parametru nepriklauso.



53 pav.  $\langle TI \rangle$  profiliai, esant a)  $Re_{h1} = 500$ ; b)  $Re_{h1} = 1000$ ; c)  $Re_{h1} = 1500$ ; d)  $Re_{h1} = 2000$

Eksperimentiškai išmatuoti išilginiai šlyties greičio profiliai pateikti 54 pav. skirti parodyti fluído maišymąsi atitrūkusiame šlyties sluoksnyje. Visi 54 pav. pateikiami profiliai išmatuoti išilgai kavernos laipto aukštyje  $h_1$ . Parametras  $\gamma_{\max}$  atitinka maksimalų šlyties greitį stacionaraus tekėjimo atveju. Šlyties greičio pasiskirstymas kavernoje tiesiogiai priklauso nuo recirkuliacinės zonos ilgio, kadangi ilgesnė recirkuliacinė zona pasižymi ilgesniu atitrūkusio šlyties sluoksniu, kuris pasižymi didesniais šlyties įtempiais. Esant  $Re_{h1} = 100 - 500$ , recirkuliacinės zonos ilgis priklauso nuo pulsacijų amplitudės, todėl pulsuojančio srauto atvejais kai  $A = 0,15$ , matomos mažiausios šlyties greičio vertės. Tačiau priešingas efektas matomas pulsuojančio srauto atveju su  $A = 0,60$ , kuris pasižymi aukštesnėmis šlyties greičio vertėmis, nei stacionaraus tekėjimo atveju, nepaisant to, jog recirkuliacinės zonos ilgis trumpesnis. Didelės amplitudės pulsacijos sutrikdo recirkuliacinę zoną, tokiu būdu sumažinant srauto stabilumą ir suintensyvinant srauto maišymąsi kavernoje, dėl ko gaunamos didesnės šlyties greičio vertės. Esant  $Re_{h1} = 1500$ , stacionaraus tekėjimo atveju recirkuliacinė zona užpildo visą kaverną, todėl matomas tolygus šlyties greičio pasiskirstymas išilgai kavernos, priešingai nei pulsuojančio tekėjimo atvejais, kur atitrūkęs šlyties sluoksnis prisijungia prie kavernos apatinės sienos, todėl matomos didesnės šlyties greičio vertės pirmoje kavernos dalyje ( $x/h_1 < 4$ ). Antroje kavernos dalyje ( $x/h_1 > 4$ ) matomas šlyties greičio sumažėjimas dėl toje vietoje žemyn pasislinkusio šlyties sluoksniu. Turbulentinio tekėjimo metu, esant  $Re_{h1} = 2000$ , matomas bendrinė pulsacijų įtaka šlyties sluoksniui, kada pulsacijos suintensyvina įtempius šlyties sluoksnyje ir tokiu būdu padidina šlyties greičio vertes, nepriklausomai nuo pulsacijų parametru.

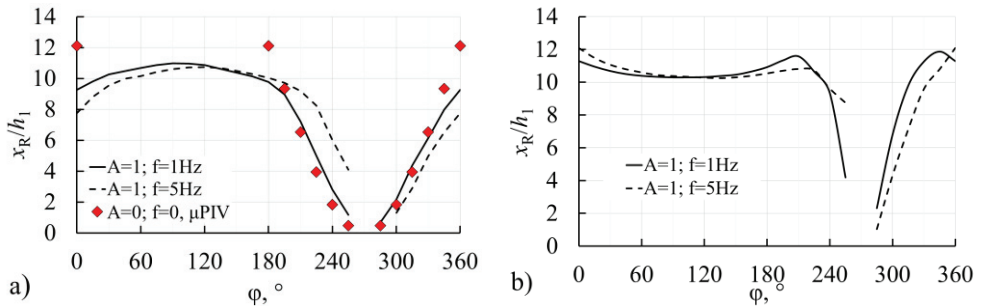


**54 pav.** Išilginio šlyties greičio horizontalūs profiliai pereinamojo tipo kavernoje, esant a)  $Re_{h1} = 100$ ; b)  $Re_{h1} = 500$ ; c)  $Re_{h1} = 1500$ ; d)  $Re_{h1} = 2000$



#### 4.3.2.4. Pulsacijų dažnio įtaka srauto struktūrai

Siekiant atlikti recirkuliacinės zonos vystymosi pulsacijų ciklo metu analizę, skaitinio modeliavimo metodu buvo gauta recirkuliacinės zonos ilgio priklausomybė nuo fazės kampo  $\varphi$  (55 pav.). Pulsacijų ciklas pagal greitį skirstomas į dvi dalis: greitėjimo (esant  $0^\circ < \varphi < 90^\circ$  ir  $270^\circ < \varphi < 360^\circ$ ) ir lėtėjimo (esant  $90^\circ < \varphi < 270^\circ$ ). Iš gautų rezultatų pastebimas skirtingas recirkuliacinės ilgio kitimo dėsningumas, esant skirtingiems  $Re_{hl}$ . Esant  $Re_{hl} = 300$ , pulsacijų ciklo greitėjimo dalyje, recirkuliacinės zonos ilgis auga dėl laminariniam tekėjimui būdingos recirkuliacinės zonos dinamikos. Tačiau, esant  $Re_{hl} = 1500$ , augant greičiui įvyksta tekėjimo režimo pasikeitimas ir srautas pasiekia turbulentinį tekėjimo režimą, kurio metu recirkuliacinė zona yra sutrumpėjusi. Šie skirtumai nulemia didesnes arba mažesnes santykinės recirkuliacinės zonos ilgio vertes greičio didėjimo fazėje, priklausomai nuo  $Re_{hl}$ . Pulsacijų ciklo metu, greičio lėtėjimo dalyje abiem  $Re_{hl}$  atvejais matomas spartus recirkuliacinės zonos trumpėjimas iki kol srautas kavernoje sustoja, todėl rezultatai esant  $\varphi = 270^\circ$  nėra duoti.

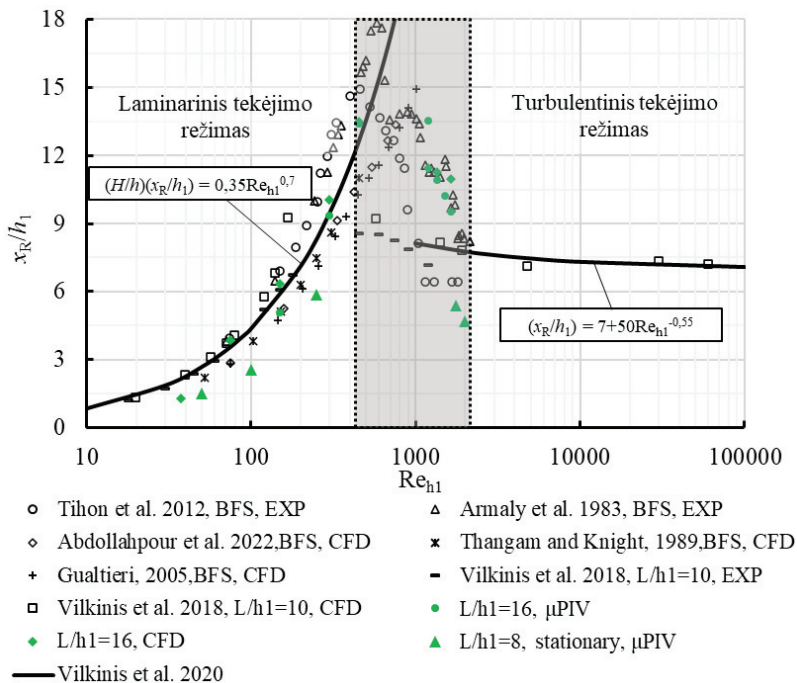


**55 pav.** Recirkuliacinės zonos ilgio priklausomybė nuo pulsacijų ciklo fazės kampo uždarojo tipo kavernoje, esant a)  $Re_{hl} = 300$ ; b)  $Re_{hl} = 1500$

Pulsacijų ciklo metu buvo pastebėta, jog recirkuliacinės zonos ilgio kitimo dėsningumai skiriasi priklausomai nuo pulsacijų dažnio, kada lyginami  $f = 1$  Hz ir  $f = 5$  Hz atvejais. Esant  $Re_{hl} = 300$ , pulsuojančio srauto atvejis su  $f = 1$  Hz, greitėjimo dalyje, pasižymi ilgesnėmis recirkuliacinės zonos ilgio vertėmis, tačiau kada pulsacijų ciklo metu greitis mažėja, matomos mažesnės recirkuliacinės zonos vertės, lyginant su  $f = 5$  Hz atveju. Esant aukštam pulsacijų dažniui, pulsacijos periodas yra trumpesnis, todėl greičio pokyčiai ciklo metu per tą patį laiko vienetą yra daug didesni, lyginant su  $f = 1$  Hz atveju, ir tai lemia skirtingą recirkuliacinės zonos vystymąsi. Dėl recirkuliacinės zonos atsako į pulsacijos periodą, jos ilgio kitimas uždeliamas  $10^\circ - 15^\circ$  fazės kampo, esant  $f = 5$  Hz, kas atitinka  $\sim 5\%$  viso pulsacijų ciklo. Šis efektas galioja ir esant  $Re_{hl} = 1500$ , tačiau poveikis pastebimai silpnesnis.

#### 4.3.2.5. Recirkuliacinės zonos ilgio priklausomybės nuo $Re$ palyginimas su kitų autorių darbais

56 pav. pateikiamos recirkuliacinės zonos ilgio priklausomybių nuo  $Re_{h1}$  palyginimas kanaluose su atgaliniu laiptu ir kavernoje. Siekiant korektiško palyginimo, visi pateikiami tyrimų rezultatai gauti atliekant eksperimentinius matavimus ir skaitinius modeliavimus kanaluose, kurių išsiplėtimo santykis  $ER = 2$ .



**56 pav.** Recirkuliacinės zonos ilgio priklausomybės nuo  $Re_{h1}$  palyginimas su kitų autorių darbais

Literatūroje pateikiami rezultatai išsiskleidę, tačiau pagrindiniai atitrūkusio srauto tekėjimo dėsningumai galioja ir gali būti apibrėžiami pagal grafike pateikiamas priklausomybes, galiojančias laminariniame ir turbulentiame tekėjimo režimuose (Vilkinis et al., 2020). Lyginant tekėjimą kavernoje, su tekėjimu aptekant atgalinį laiptą pastebimi tie patys, anksčiau aprašyti, recirkuliacinės zonos ilgio kitimo dėsningumai priklausomai nuo tekėjimo režimo. Lyginant santykinio ilgio vertes tame pačiame  $Re$ , galima matyti, jog kanaluose su atgaliniu laiptu recirkuliacinės zonos ilgio vertės ženkliai didesnės. Mažesnes  $x_R/h_1$  vertes uždaro ir pereinamojo tipo kavernų atvejais nulemia priekinio laipto daroma įtaka, kuri fiziškai apriboja recirkuliacinę zoną nuo ilgų verčių susidarymo, taip lemiant atitrūkusio šlyties sluoksnio prisijungimą arčiau atgalinio kavernos laipto. Taip pat, kai kanaluose su atgaliniu laiptu stebimos didžiausios  $x_R/h_1$  vertės, kavernoje nėra atitrūkusio šlyties

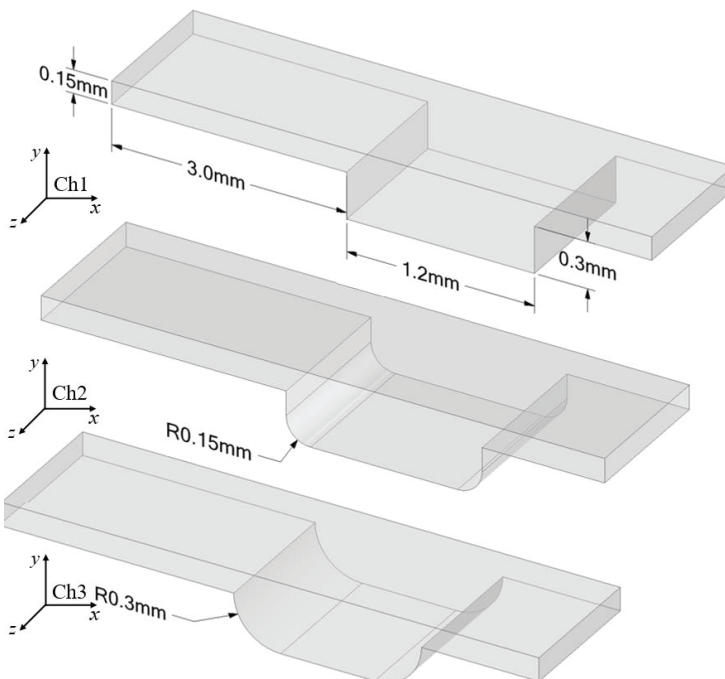
sluoksniu prisijungimo ant kavernos dugno ir visa kaverna yra užpildyta recirkuliacine zona. Didžiausias rezultatų išsisklaidymas stebimas pereinamajame tekėjimo režime, kai sraute atsiranda įvairūs nestabilumai. Atlikus rezultatų palyginimą su kitais autoriais, galima teigti, jog šiame darbe pateikiami rezultatai puikiai atitinka tendencijas ir nenukrypsta nuo literatūroje pateikiamų tyrimų rezultatų.

### 4.3.3. Pasyvus srauto valdymas

#### 4.3.3.1. Kavernos geometrinų parametrų įtaka srauto struktūrai

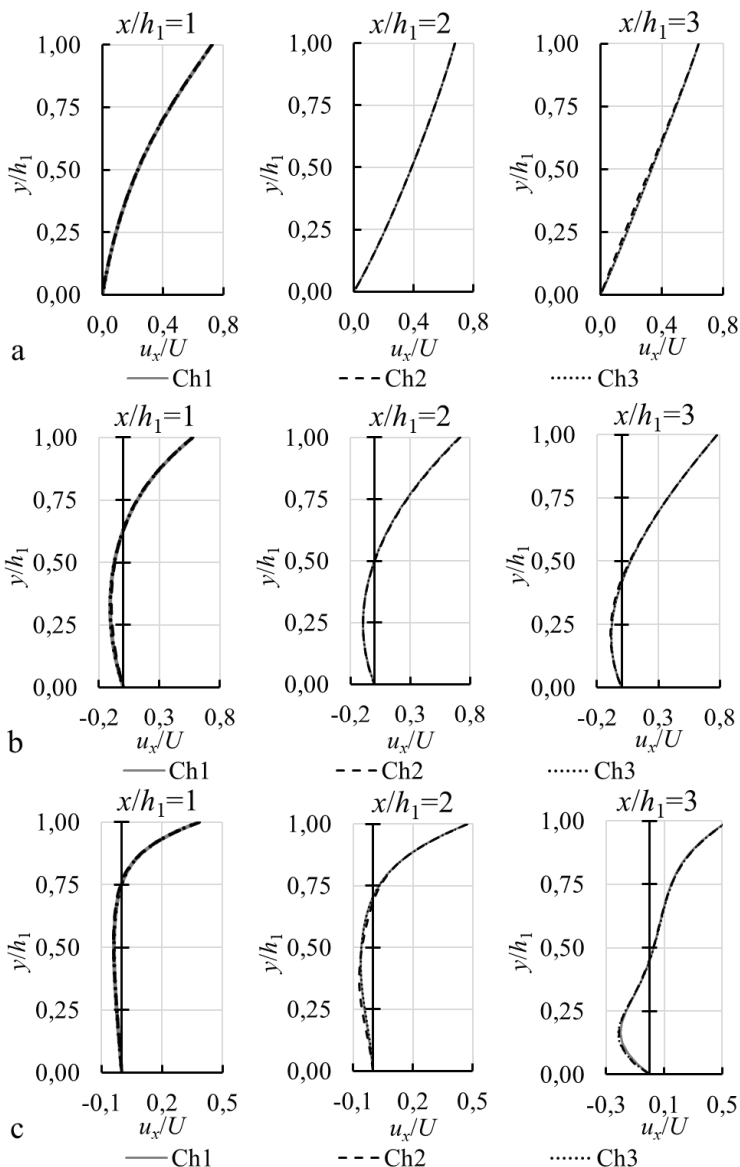
Šio darbo eksperimentiniuose matavimuose, dėl ribotų kanalų gamybos galimybių, buvo naudotos kavernos su apvalintais vidiniais kampais ( $R/h_1 = 0,5$ ). Literatūroje dažniausiai atliekami tyrimai kanaluose su stačiais kampais, todėl natūralu, jog reikalingas papildomas tyrimas, kuris leistų apibrėžti kavernos kampų įtaką srauto struktūrai.

57 pav. pateiktos trijų skirtingų atviro tipo kavernos vidinių kampų konfigūracijų geometrijos, kurios buvo naudotos skaitiniam modeliavimui (Ch1, Ch2 ir Ch3). Ch1 atvejis atitinka kavernos su stačiais kampais kanalą. Ch2 kanalo atveju –  $R/h_1 = 0,5$ , kuris atitinka šiame darbe naudojamų kavernų vidinių kampų formas. Galiausiai, Ch3 atitinka ribinį  $R/h_1 = 1$  atvejį, tam, kad tiriamojo parametro ribos būtų nuo minimalios iki maksimalios reikšmės.



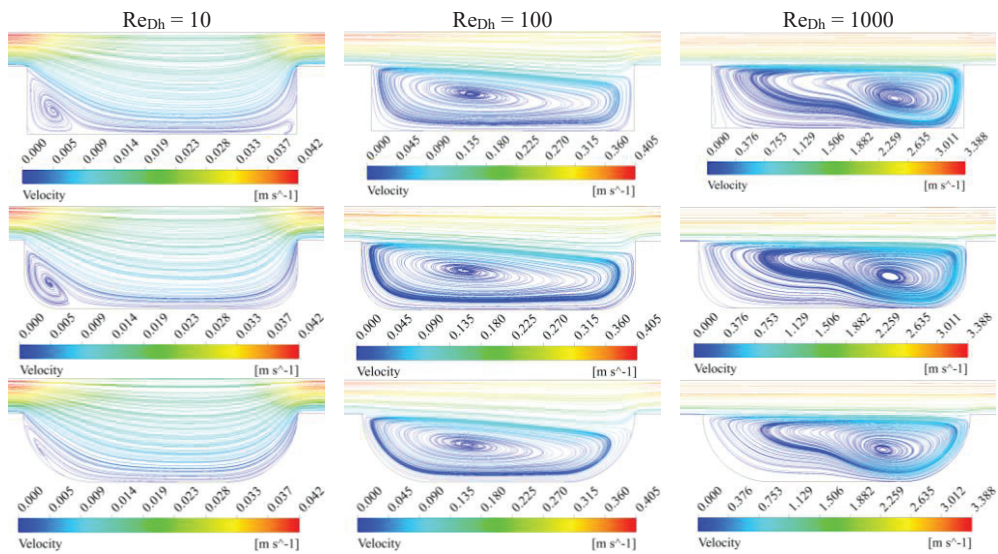
57 pav. Skaičiavimams naudotų trimačių atviro tipo kavernų geometrijos su skirtingai apvalintais vidiniais kampais

58 pav. Pateiktas santykinio greičio pasiskirstymas atviro tipo kavernoje, visose tirtose geometrijose (Ch1, Ch2 ir Ch3). Greičio profiliai paimti vidurinėje  $x$ - $y$  plokštumoje, esant  $z/b = 0,5$ . Atlikus greičio pasiskirstymo palyginimą kanaluose su skirtingais  $R/h_1$  santykiais, galima matyti, jog pasiskirstymai beveik idealiai sutampa ir nepriklauso nuo vidinių kavernos kampų formos. Verta pastebėti, jog greičio pasiskirstymas identiškas net ir ribiniame  $R/h_1$  atveju.



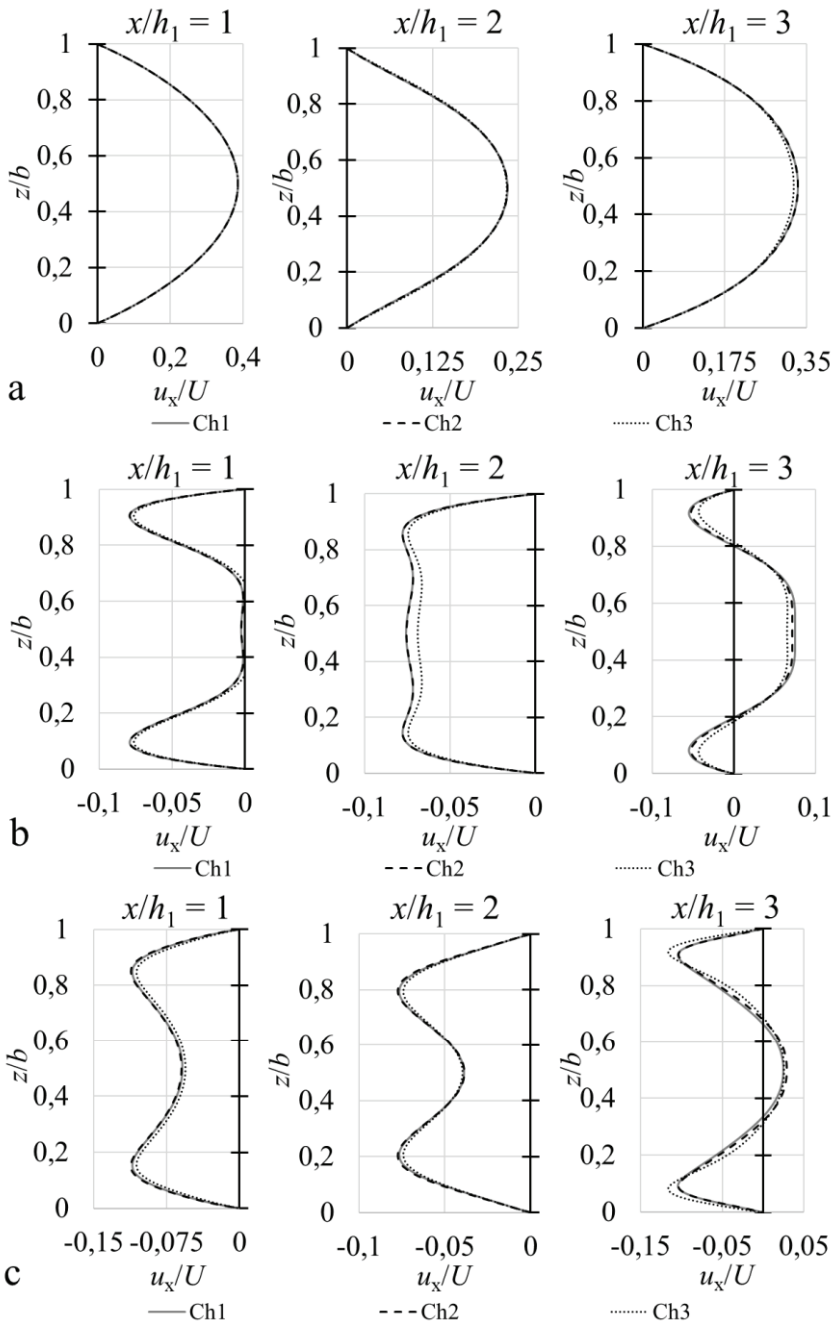
**58 pav.** Santykinio greičio profiliai  $x$ - $y$  ašyje atviro tipo kavernoje, esant a)  $Re_{Dh} = 10$ ; b)  $Re_{Dh} = 100$ ; c)  $Re_{Dh} = 1000$

59 pav. Pateikiamos greičio srauto linijos atviro tipo kavernoje taip pat rodo beveik identišką atitikimą tarp Ch1, Ch2 ir Ch3 atvejų. Vienintelis skirtumas – recirkuliacinės zonos dydis Ch3 kanale, esant  $Re_{Dh} = 10$ . Santykio  $R/h_1 = 1$  vertė lemia tolygesnį fluideo aptekėjimą per kavernos kampą, dėl ko sumažinamas slėgio gradientas atsirandantis dėl staigaus kanalo išplatėjimo, kuris ir apsprendžia susidariusios recirkuliacinės zonos dydį. Šis efektas matomas tik esant itin mažam  $Re_{Dh}$ , nes slėgio gradientas reikalingas susidaryti recirkuliacinei zonai yra nedidelis, todėl net ir minimalūs geometrijos pokyčiai gali turėti tam įtakos. Esant  $Re_{Dh} > 10$  šis efektas nebepastebimas ir tolesniam srauto vystymuisi įtakos nedaro.



**59 pav.** Greičio srauto linijos atviro tipo kavernoje, esant skirtingoms vidinių kavernos kampų konfigūracijoms

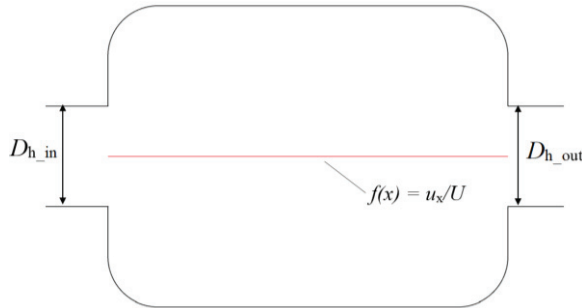
Tolimesnei analizei buvo lyginamas greičio pasiskirstymas  $x$ - $z$  plokštumoje (60 pav.). Profiliai išmatuoti santykiname aukštyje  $y/h_1 = 0,5$ , pateikiami siekiant parodyti srauto trimatiškumą kavernoje. Panašiai kaip ir 58 pav.  $x$ - $z$  plokštumos profiliai beveik tobulai sutampa tarp lyginamųjų Ch1, Ch2 ir Ch3 geometrijų. Didžiausia įtaka srauto struktūrai matoma esant Ch3 atvejui, kada matomas šiek tiek mažesnis srauto greitis kanalo centre. Neatitikimai tarp greičio pasiskirstymo nežymūs, todėl galima teigti, jog kavernos vidinių kampų užapvalinimas neturi įtakos srauto struktūrai.



**60 pav.** Santykinio greičio profiliai  $x$ - $z$  plokštumoje atviro tipo kavernoje, esant a)  $Re_{Dh} = 10$ ; b)  $Re_{Dh} = 100$ ; c)  $Re_{Dh} = 1000$

61 pav. pateikiama skaitiniam modeliavimui naudotos atviro tipo kavernos geometrija su skirtingais ištekėjimo hidrauliniiais diametrais. Taip pat, brėžinyje

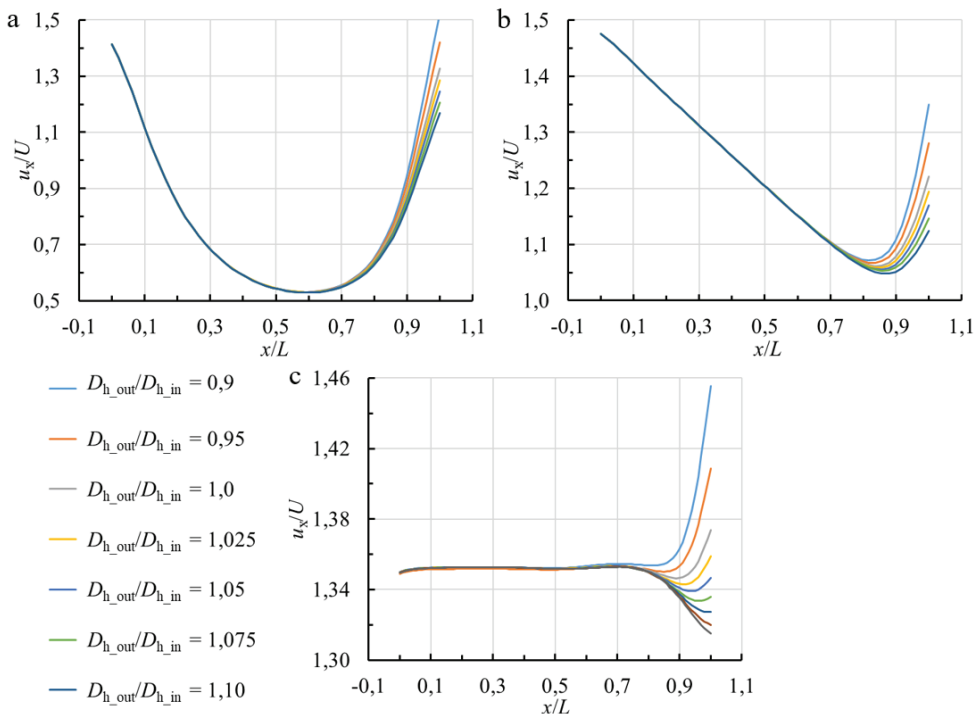
pateikta išilginio greičio profilio lokacija. Siekiant iširti ištekėjimo ir įtekėjimo hidraulinių diametrų santykio įtaką išilginio greičio pasiskirstymui, įtekėjimo hidraulinis diemtras ( $D_{h\_in}$ ) buvo pastovus, o keičiamas buvo  $D_{h\_out}$ . Išilginio greičio pasiskirstymas – parametras, leidžiantis aprašyti tekančio fluideo sistemos stabilumą, kada tekėjimas be didesnių greičio pokyčių išilgai tiriamojo kanalo gali būti laikomas kaip stabilus.



**61 pav.** Atviro tipo kaverna ( $L/h_1 = 4$ ) su išilginio greičio profilio lokacija

Greičio pasiskirstymas išilgai kavernos, esant  $Re_{Dh} = 10 - 1000$  pateiktas 62 pav. Šiame paveiksle pateikti trys tekėjimo atvejai pagal vidutinę tekėjimo struktūrą:  $Re_{Dh} = 10$  – atitrūkęs šlyties sluoksnis prisijungia prie kavernos dugno,  $Re_{Dh} = 100$  – atitrūkęs šlyties sluoksnis neprisijungia prie kavernos dugno, tačiau recirkuliacinės zonos centras arčiau atgalinio laipto ir  $Re_{Dh} = 1000$  – atitrūkęs šlyties sluoksnis neprisijungia prie kavernos dugno, o recirkuliacinės zonos centras pasislinkęs prie priekinio kavernos laipto. Greičio kitimo dinamika tiesiogiai susijusi su geometriniais pokyčiais kavernoje, kada matomas greičio mažėjimas esant staigiam kavernos skerspjūvio pokyčiui ir staigus didėjimas fluidui tekant link ištekėjimo iš kavernos, kai  $Re_{Dh} = 10 - 100$ . Greičio vertės visais tirtais  $Re_{Dh}$  atvejais idealiai sutampa kai  $x/L < \sim 0,8$ . Tai reiškia, jog ištekėjimo hidraulinio diametro pokytis pačiai srauto struktūrai kavernoje įtakos nedaro, tačiau esant  $x/L > 0,8$ , greitis tiesiogiai priklauso nuo  $D_{h\_out}$ . Didžiausias greitis kanalo ištekėjime matomas esant  $D_{h\_out}/D_{h\_in} = 0,9$ , o mažiausias – kai  $D_{h\_out}/D_{h\_in} = 1,1$ . Kadangi esant  $Re_{Dh} = 10 - 100$  atitrūkęs šlyties sluoksnis neprisijungia ant kavernos apatinės sienos tiek viršuje, tiek ir apačioje, į kaverną įtekantis fluidas apribojamas kanalo sienų, o kanalo išplatėjimo vietoje šis apribojimas vyksta viršutinio ir apatinio šlyties sluoksnio pagalba. Iš 59 pav. pateiktų srauto linijų esant  $Re_{Dh} = 10 - 100$  matyti, jog viršuje ir apačioje esančių šlyties sluoksnių apribotas pagrindinis srautas plečiasi, kai fluidas artėja prie priekinio kavernos laipto. Tai sukelia greičio lėtėjimą matomą 62 pav. Esant  $Re_{Dh} = 1000$ , dėl didesnio greičio, recirkuliacinės zonos centras pasislenka link priekinio laipto ir šlyties sluoksnis susidaro tiesioje horizontalėje tarp kavernos laiptų (59 pav.), todėl pagrindinis srautas nesiplečia ir greitis nemažėja iki kol fluidas pasiekia ištekėjimą iš kavernos. Tada išilginio greičio pasiskirstymas vėl tiesiogiai priklauso nuo ištekėjimo diametro ir

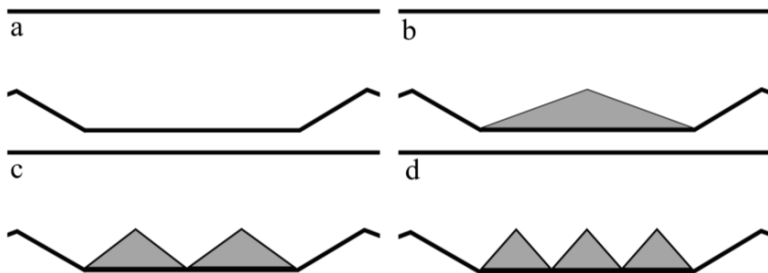
matomos aukščiausios vertės, esant  $D_{h\_out}/D_{h\_in} = 0,9$  ir mažiausios – esant  $D_{h\_out}/D_{h\_in} = 1,15$ .



**62 pav.** Išilginio greičio pasiskirstymas, esant skirtingiems ištekėjimo ir įtekėjimo hidraulinių diametrų santykiams, esant a)  $Re_{Dh} = 10$ ; b)  $Re_{Dh} = 100$ ; c)  $Re_{Dh} = 1000$

#### 4.3.3.2. Šiurkštumo elementų įtaka srauto struktūrai ir slėgio nuostoliams kanale

Siekiant ištirti šiurkštumo elementų įtaką atitrūkusio srauto dinamikai, pasirinktos keturios skirtingos šiurkštumo elementų konfigūracijos (63 pav.): kaverna be šiurkštumo elementų ir trys atvejai su 1-3 trikampės formos šiurkštumo elementais. Šiurkštumo elementų pagalba kaverna suskirstoma į keletą atskirų sūkurių, tokiu būdu apribojant recirkuliacinės zonos dydį.



**63 pav.** Kanalas su skirtingu skaičiumi šiurkštumo elementų: a) 0; b) 1; c) 2; d) 3



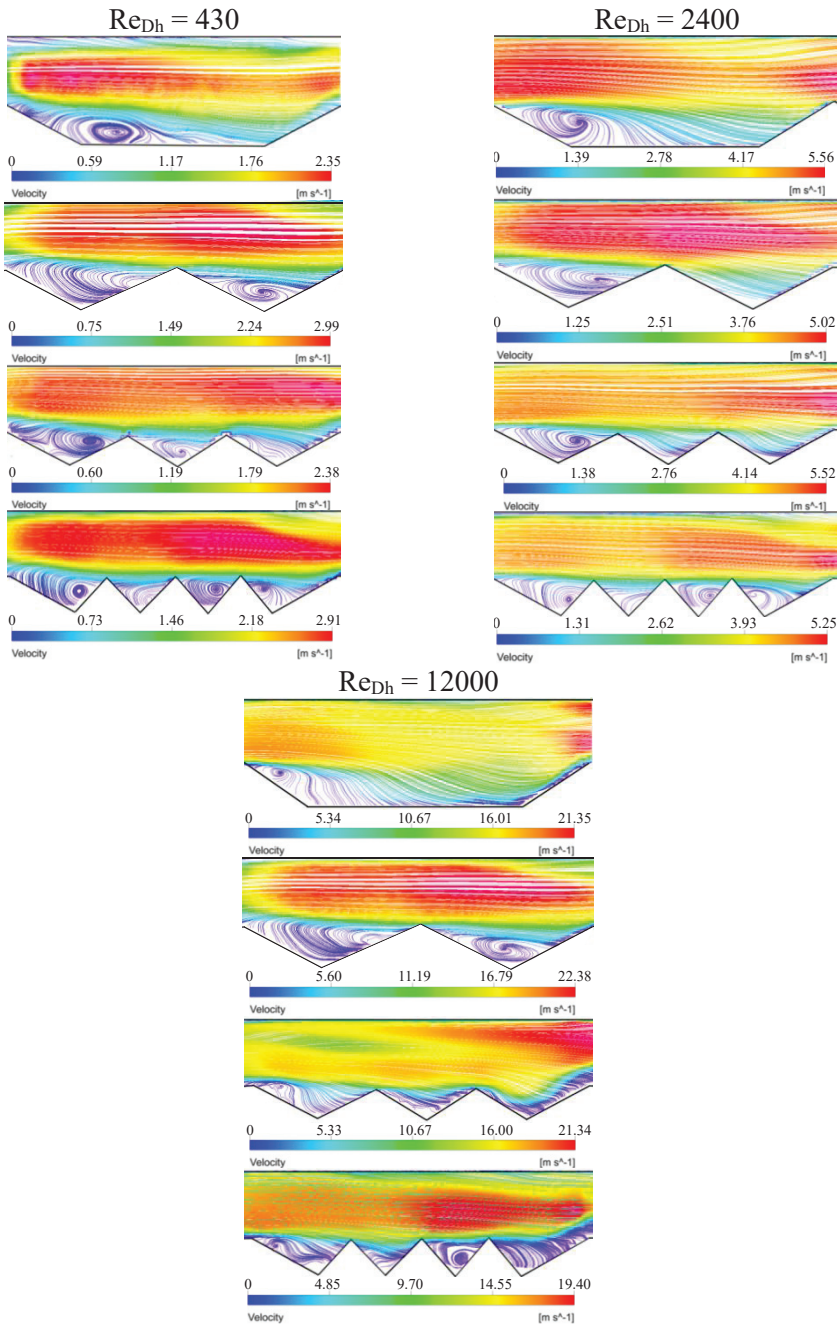
Vidutinio greičio pasiskirstymas kanale su skirtingu skaičiumi šurkštumo elementų pateiktas 64 pav. Tuščiaje kanale ( $\lambda = 8,8$ ) srautas atitrūksta nuo galinio kavernos laipto, todėl matoma recirkuliacinė zona, kuri užima 30% – 50% kavernos. Turbulentiniame tekėjimo režime, esant  $Re_{Dh} = 12000$ , recirkuliacinės zona sumažėja ir jos centras pasislenka srauto tekėjimui priešinga kryptimi.

Įtaisius vieną trikampės formos šurkštumo elementą ant kanalo dugno, kaverna suskirstoma į dvi dalis. Šiuo atveju santykinis atstumas tarp šurkštumo elementų  $\lambda = 4,7$ . Šurkštumo elementų aukštis identiškas kavernos laiptų aukščiui. Esant  $Re_{Dh} = 430$ , recirkuliacinė zona suskirstyta į du atskirus sūkurius, susidariusius šurkštumo elementu atskirtose kavernos dalyse. Pirmoje kavernos dalyje esantis sūkurys vizualiai pasislinkęs srauto tekėjimo kryptimi ir tai indikuoja apie sustiprintą atgalinį tekėjimą. Priešinga situacija matoma esant  $Re_{Dh} = 2400$ , kada sūkurys susidaro tik pirmoje kavernos dalyje, o antroje dalyje šlyties sluoksnis nuo šurkštumo elemento viršūnės neatitrūksta ir sūkurys nesusidaro, todėl srautas sklandžiai apteka antrą kavernos dalį. Esant  $Re_{Dh} = 12000$ , antroje kavernos dalyje vėl atsiranda sūkurys, kuris yra pasislinkęs kanalo apačios link. Pagal vidutinių greičio srauto linijų išsidėstymą kavernoje, esant įtaisytam vienam šurkštumo elementui, galima spręsti, jog dėl pereinamajam tekėjimo režimui būdingų nestabilumų, esant  $Re_{Dh} = 2400$ , recirkuliacinė zona negali būti padalinta į du atskirus sūkurius, priešingai nei laminariniame ir turbulentiniame tekėjimo režime.

Padidinus šurkštumo elementų skaičių iki 2, kaverna suskirstoma į tris dalis ir santykinis atstumas tarp šurkštumo elementų sumažėja iki  $\lambda = 3,3$ . Esant  $Re_{Dh} = 430$ , sūkuriai matomi tik pirmose dvejose kavernose dalyse, o trečioje dalyje sūkurys nesusidaro. Panašiai kaip ir vieno šurkštumo elemento atveju, esant  $Re_{Dh} = 2400$ , matoma mažiau sūkurių nei laminarinio tekėjimo atveju. Kai pasiekiamas turbulentinis tekėjimo režimas ( $Re_{Dh} = 12000$ ), matomos didelio kreivumo srauto linijos pirmose dvejose kavernos dalyse, kurios indikuoja apie aukštus greičio gradientus, tačiau pilnos formos sūkuriai nesusidaro nei vienoje iš kavernos dalių.

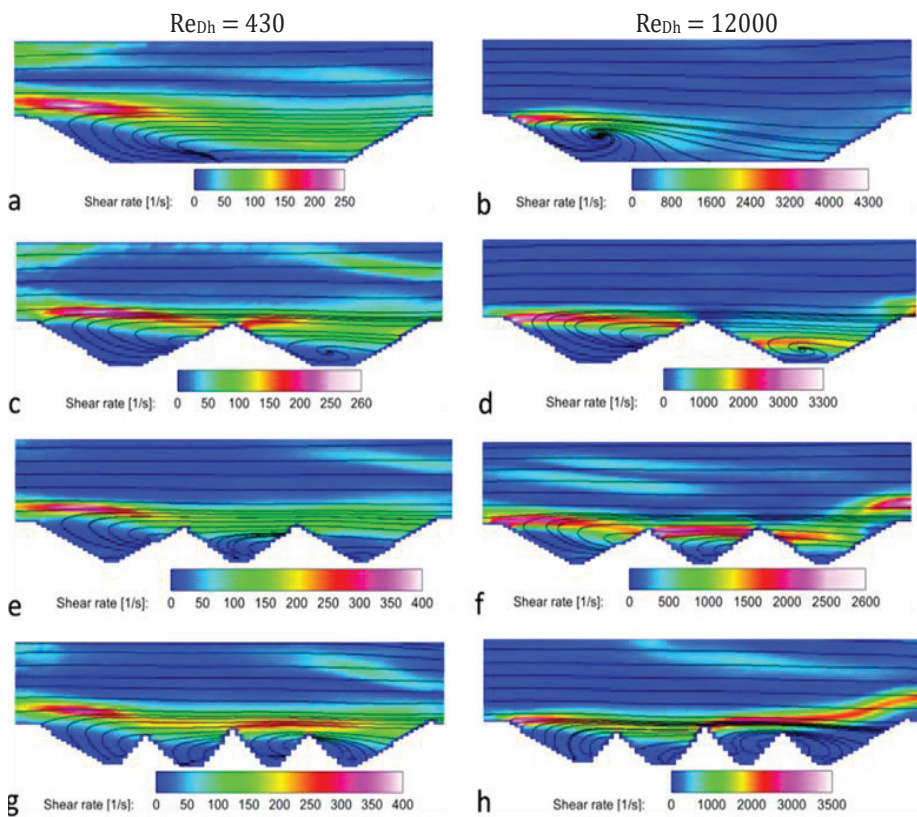
Santykinį atstumą tarp šurkštumo elementų sumažinus iki  $\lambda = 2,8$ , kaverna padalinama į keturias dalis, t.y. ant kavernos dugno įtaisomi 3 šurkštumo elementai. Toks kanalo užgriozdinimas įneša papildomo nestabilumo atitrūkusiam šlyties sluoksniui ir tai matosi iš chaotiškai išsidėsčiusių srauto linijų. Tačiau esant tokiai šurkštumo elementų konfigūracijai, recirkuliacinė zona visais tekėjimo režimų atvejais padalinama į keturis atskirus sūkurius, kas kaip vėliau bus parodyta, turi teigiamą poveikį slėgio nuostoliams kavernoje. Didėjant šurkštumo elementų skaičiui, mažėja atstumas tarp jų viršūnių. Tai neleidžia atitrūkusiam šlyties sluoksniui prisijungti prie kavernos dugno, dėl ko susidaro atskiri sūkuriai tarp šurkštumo elementų. Dėl išaugusių slėgio nuostolių, esant didesniai  $\lambda$ , sūkuriai susidaro tik pirmoje arba antroje kavernos dalyse. Kai ant kanalo dugno įtaisyta šurkštumo elementų skaičius didesnis, recirkuliacinė zona yra padalinama į 3-4

atskirus sūkurius, todėl slėgio nuostoliai kavernoje sumažėja. Detalesnė slėgio nuostolių analizė pateikiama 3.3.2.3 skyriuje.



64 pav. Vidutinio greičio srauto linijos kavernoje su skirtinga šiurkštumo elementų konfigūracija, esant  $Re_{Dh} = 430 - 12000$ .

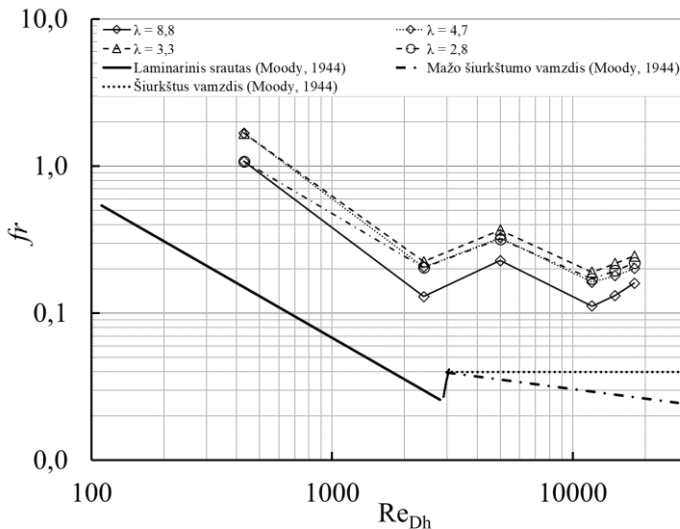
Šlyties greitis parodo, kaip fluido sluoksniai juda vienas kito atžvilgiu, todėl didžiausios šlyties greičio vertės indikuoja apie didelį greičio gradientą. Šlyties greičio pasiskirstymas pateiktas 65 pav. Didžiausios šlyties greičio vertės matomos virš atgalinio kavernos laipto. Taip pat, matoma, jog esant daugiau šiurkštumo elementų, šlyties sluoksnis nusidriekia išilgai tarp kavernos laiptų. Esant  $\lambda = 2,8$  matomas pasienio sluoksnio atsiskyrimas nuo viršutinės sienos, kuris turi neigiamos įtakos stabiliam greičio pasiskirstymui kavernoje.  $Re_{Dh}$  padidėjus nuo 430 iki 12000, matomas atsiskyrusio pasienio sluoksnio pokytis, kai šis tampa ilgesnis ir nusidriekia srauto tekėjimo kryptimi. Tolygiai išilgai kavernos susidaręs šlyties sluoksnis leidžia pagrindiniam srautui tekėti mažiau trikdomam, dėl ko sumažėja slėgio nuostoliai kanale (žr. 3.3.2.3 skyrių).



**65 pav.** Šlyties greičio pasiskirstymas, esant a, b -  $\lambda = 8,8$ ; c, d -  $\lambda = 4,7$ ; e, f -  $\lambda = 3,3$ ; g, h -  $\lambda = 2,8$

Kadangi trinties koeficientas tiesiogiai priklauso nuo slėgio nuostolių kavernoje, atlikta trinties koeficiento analizė skirta apibrėžti slėgio nuostolių priklausomybę nuo  $Re_{Dh}$  ir  $\lambda$ . Kaip galima pastebėti iš 66 pav. pateiktos trinties koeficiento priklausomybės nuo  $Re_{Dh}$ , tuščioje kavernoje pastebimi dėšningumai panašūs į

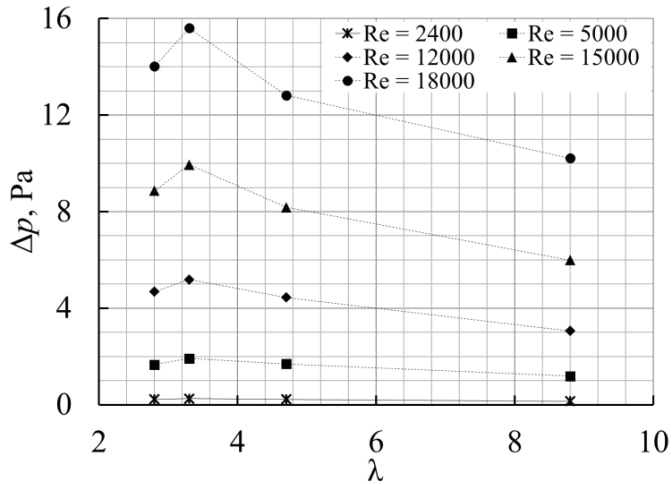
literatūroje pateikiamus dėsningumus apvalaus skerspūvio vamzdyje (Moody, 1944). Žinoma, dėl kanalo užgriozdinimo visos eksperimentinių matavimų metu gautos kreivės pasižymi didesnėmis trinties koeficiento reikšmėmis, palyginus su literatūroje pateikiamomis. Taip pat, galima pastebėti, jog srauto perėjimas iš laminarinio į turbulentinį tekėjimo režimą, vykstantis nuo  $Re_{Dh} = 2400$ , vyksta ilgiau  $Re_{Dh}$  atžvilgiu, lyginant su srautu vamzdyje.



**66 pav.** Trinties koeficiento priklausomybė nuo  $Re_{Dh}$ , esant skirtingai šiurkštumo elementų konfiguracijai kavernoje

Visais  $Re_{Dh}$  atvejais, didinant šiurkštumo elementų kiekį – trinties koeficientas didėja iki tol kol yra pasiekiamas kritinis atstumas  $\lambda$ , kuris šiuo atveju  $\lambda = 3,3$ . Atstumui tarp šiurkštumo elementui mažėjant nuo 8,8 iki 3,3, trinties koeficientas auga dėl 3.3.2.1 poskyryje aptarto sukurių susidarymo dėsningumo, kada sukuriai susidaro tiksliai pirmoje kavernos dalyje, o kitose dalyse sukurių nėra, todėl šlyties sluoksnis nenusidriekia išilgai kavernos ir pagrindinis srautas prateka su didesniais energijos nuostoliais. Priešingas atvejis matomas kai  $\lambda = 2,8$ , recirkuliacinė zona šiurkštumo elementų pagalba padalinama į keletą atskirų sukurių, šlyties sluoksnis nusidriekia nuo kavernos atgalinio laipto iki priekinio ir pagrindinis srautas prateka lengviau, todėl gaunami slėgio nuostoliai ir trinties koeficientas – mažesnis (67 pav.). Šis fenomenas sutinkamas atviro tipo kavernoje, kai atitrūkęs šlyties sluoksnis neprisijungia prie kavernos dugno, tokiu būdu pagrindinis srautas yra mažiau trikdomas ir prateka su mažesniais slėgio nuostoliais. Specifinis atstumas tarp šiurkštumo elementų, apriboja nuo didelių sukurių susidarymo ir taip sumažina pasipriešinimą, atsirandantį dėl klamos, dėl ko su šlyties sluoksniu sąveikauja tik šiurkštumo elemento viršūnė (Choi et al., 1993).

67 pav. pateikta slėgio nuostolių priklausomybė nuo šiurkštumo elementų skaičiaus, esant skirtingiems  $Re_{Dh}$ , kuriame galima matyti slėgio pokyčių sumažėjimą, kai pasiekiamas kritinis atstumas  $\lambda$ . Lyginant atvejus  $\lambda = 3,3$  ir  $\lambda = 2,8$  slėgio sumažėjimas  $Re_{Dh} = 18000$  atveju siekia 12 %. Didėjant  $Re_{Dh}$ , ribose  $430 < Re_{Dh} < 18000$ , matomas didesnis  $\Delta p$  pokytis. Kai  $Re_{Dh} < 2400$ , slėgio nuostoliai kavernoje pastovūs ir neviršija matavimų neapibrėžties.



67 pav. Slėgio nuostolių priklausomybė nuo atstumo tarp šiurkštumo elementų  $\lambda$

## IŠVADOS

Eksperimentiniais srauto vizualizacijos ir skaitinio modeliavimo metodais šiame darbe ištirti aktyvaus ir pasyvaus srauto valdymo įtaką srauto dinamikai ir struktūrai lemiantys veiksniai atviro, pereinamojo ir uždarojo tipo kavernoje. Srauto valdymas buvo realizuojamas panaudojant srauto pulsacijas, šurkštumo elementus ir kavernos geometrinių parametrų pokyčius. Iš gautų tyrimų rezultatų buvo padarytos šios išvados:

1. Esant laminariniam ir pereinamajam tekėjimo režimui, recirkuliacinės zonos ilgis ir srauto struktūra priklauso nuo pulsacijų amplitudės ir dažnio:
  - 1.1. Laminariniame ir pereinamajame tekėjimo režimuose pulsuojantis srautas trumpina recirkuliacinę zoną. Laminariniame tekėjimo režime šio efekto intensyvumas atvirkščiai proporcingas pulsacijų amplitudei. Didžiausias efektas pasiekiamas pereinamojo tipo kavernoje, esant  $Re_{Dh} = 250$ , kai recirkuliacinė zona, esant  $A = 0,15$ , sutrumpinama apie 45%.
  - 1.2. Pulsacijų dažnio įtaka tirtame  $f = 0,5-5$  Hz diapazone laike suvidurkintam recirkuliacinės zonos ilgiui neviršijo 6%. Kadangi šio efekto intensyvumas mažesnis už matavimų neapibrėžtį – pulsacijų dažnio įtaka recirkuliacinės zonos ilgiui gali būti laikoma nereikšminga.

Turbulentiniame tekėjimo režime, kai recirkuliacinė zona pasiekia asimptotinę vertę ir nebeprisilaiko nuo  $Re$ , pulsuojančio srauto įtaka taip pat tampa nereikšminga.
2. Pulsacijų ciklo lėtėjimo fazėje pastebimas recirkuliacinės zonos vystymosi vėlavimas, kuris lyginant ribinius  $f = 1$  Hz ir 5 Hz atvejus pasireiškia iki 70% ilgesnėmis  $x_R$  vertėmis, esant didesnio dažnio pulsuojančiam srautui toje pačioje ciklo fazėje. Priešingas atvejis stebimas pulsacijų ciklo metu greičiui kylant, kada  $f = 5$  Hz atvejis pasižymi iki 40% trumpesnėmis  $x_R$  vertėmis nei toje pačioje ciklo fazėje esančio  $f = 1$  Hz pulsuojančio srauto atvejis. Lyginant pulsacijų ciklus, esant  $f = 1$  Hz ir 5 Hz dažnio pulsacijoms, recirkuliacinės zonos vystymosi vėlavimas pasireiškia iki 5% ( $15^\circ$  fazinio kampo atžvilgiu).
3. Pulsuojantis srautas dėl papildomai sukeliama greičio fluktuacijų didina turbulentinį intensyvumą kavernoje, esant pereinamajam tekėjimo režimui. Turbulentinio tekėjimo režimo metu, turbulentiškumo pasiskirstymas kavernoje yra nulemiamas greičio fluktuacijų atsirandančių dėl paties tekėjimo režimo, todėl dėl pulsuojančio srauto atsirandančios greičio fluktuacijos tampa nereikšmingos ir srauto turbulentiškumas nuo pulsacinių parametrų nebeprisilaiko.
4. Kavernos vidinių kampų užapvalinimas, aprašomas santykiu  $R/h_1$ , srauto dinamikai ir struktūrai įtakos nedaro, tačiau išilginio greičio pasiskirstymas kavernoje apsprendžiamas kavernos ištekėjimo ir įtekėjimo hidraulinių diametrų santykiu. Išilginio greičio pasiskirstymą kavernos centre lemia atitrūkęs šlyties sluoksnis, kuris riboja pagrindinio srauto plėtimąsi ir užtikrina

tolygų greičio pasiskirstymą iki  $x/L = 0,8$ . Kai  $x/L > 0,8$  išilginis greitis tampa atvirkščiai proporcingas santykiui  $D_{h\_out}/D_{h\_in}$ . Santykiui padidėjus 10 %, išilginis greitis kavernoje ištekėjime virš priekinio laipto sumažėja iki 13 % ir atvirkščiai.

5. Slėgio nuostoliai kavernoje atvirkščiai proporcingi nuo atstumo tarp šiurkštumo elementų iki kol yra pasiekiamas kritinis atstumas  $\lambda = 3,3$ . Kai  $\lambda < 3,3$ , šlyties sluoksnis atitrūksta nuo šiurkštumo elementų viršūnių sudarydamas atskiras recirkuliacines zonas tarp jų. Pasiekus kritinį atstumą tarp šiurkštumo elementų, recirkuliacinė zona yra padalinama į atskirus mažus sūkurius, dėl kurių šlytis sumažėja, kartu iki 12 % sumažinant ir slėgio nuostolius.

## REFERENCES

1. ABBAS, Z., MANSOOR, M., HABIB, M., ir MEHMOOD, Z. Review: MEMS sensors for flow separation detection. *Microsystem Technologies*. 2023, 29(9), 1253–1280. ISSN 14321858.
2. ALAM, M. M. A review of cylinder corner effect on flow and heat transfer. *Journal of Wind Engineering and Industrial Aerodynamics*. 2022, 229(June), 105132. ISSN 01676105.
3. ARMALY, B. F., DURST, F., PEREIRA, J. C. F., ir SCHÖNUNG, B. Experimental and theoretical investigation of backward-facing step flow. *Journal of Fluid Mechanics*. 1983, 127(1), 473. ISSN 0022-1120.
4. BARDERA, R., MATÍAS, J. C., ir BARROSO, E. Experimental and numerical simulations of simple frigate with suction flow control over the deck. *Ocean Engineering*. 2021, 236(June), 109464. ISSN 00298018.
5. BARKLEY, D., GOMES, M. G. M., ir HENDERSON, R. D. Three-dimensional instability in flow over a backward-facing step. *Journal of Fluid Mechanics*. 2002, 473(473), 167–190. ISSN 00221120.
6. BEAUDOIN, J. F., CADOT, O., AIDER, J. L., ir WESFREID, J. E. Three-dimensional stationary flow over a backward-facing step. *European Journal of Mechanics, B/Fluids*. 2004, 23(1), 147–155. ISSN 09977546.
7. BECHERT, D. W., BRUSE, M., HAGE, W., VAN DER HOEVEN, J. G. T., ir HOPPE, G. Experiments on drag-reducing surfaces and their optimization with an adjustable geometry. *Journal of Fluid Mechanics*. 1997, 33859–87. ISSN 0022-1120.
8. BENTALEB, Y., LARDEAU, S., ir LESCHZINER, M. A. Large-eddy simulation of turbulent boundary layer separation from a rounded step. *Journal of Turbulence*. 2012, 131–28. ISSN 14685248.
9. BERGADÀ, J. M. ir BUGEDA, G. Flow Control, Active and Passive Applications. *Applied Sciences (Switzerland)*. 2023, 13(16), 10–12. ISSN 20763417.
10. BILGEN, E. ir OZTOP, H. Natural convection heat transfer in partially open inclined square cavities. *International Journal of Heat and Mass Transfer*. 2005, 48(8), 1470–1479. ISSN 00179310.
11. BISWAS, G., BREUER, M., ir DURST, F. Backward-facing step flows for various expansion ratios at low and moderate reynolds numbers. *Journal of Fluids Engineering, Transactions of the ASME*. 2004, 126(3), 362–374. ISSN 00982202.
12. BOSE, S. ir PATLE, S. D. Analysis of convective heat transfer over a square cylinder with rounded corners under steady flow regime at low Reynolds number. *Journal of Physics: Conference Series*. 2020, 1706(1), ISSN 17426596.
13. BRAVO, H. R. ir ZHENG, Y. H. Turbulent flow over step with rounded edges: Experimental and numerical study. *Journal of Hydraulic Engineering*. 2000, 126(1), 82–85. ISSN 07339429.
14. BRERETON, G. J. ir JIANG, Y. Convective heat transfer in unsteady laminar parallel flows. *Physics of Fluids*. 2006, 18(10), ISSN 10706631.
15. VAN BUREN, S., MIRANDA, A. C., ir POLIFKE, W. Large eddy simulation of enhanced heat transfer in pulsatile turbulent channel flow. *International Journal of Heat and Mass Transfer*. 2019, 144118585. ISSN 00179310.
16. CEGLIA, G., INVIGORITO, M., CHIATTO, M., GRECO, C. S., CARDONE, G., ir DE LUCA, L. Flow control on a 2D back-facing ramp by Synthetic Jets. 2020, 294–298.
17. CHAVAN, T., CHAKRABORTY, M., ir VAIDYANATHAN, A. Experimental and modal decomposition studies on cavities in supersonic flow. *Experimental Thermal*



- and Fluid Science*. 2022, 135(February 2021), 110600. ISSN 08941777.
18. CHEN, L., ASAI, K., NONOMURA, T., XI, G., ir LIU, T. A review of Backward-Facing Step (BFS) flow mechanisms, heat transfer and control. *Thermal Science and Engineering Progress*. 2018, 6(April), 194–216. ISSN 24519049.
  19. CHEN, W. L., HUANG, Y., CHEN, C., YU, H., ir GAO, D. Review of active control of circular cylinder flow. *Ocean Engineering*. 2022, 258ISSN 00298018.
  20. CHEN, Y. T., NIE, J. H., ARMALY, B. F., ir HSIEH, H. T. Turbulent separated convection flow adjacent to backward-facing step-effects of step height. *International Journal of Heat and Mass Transfer*. 2006, 49(19–20), 3670–3680. ISSN 00179310.
  21. CHENG, C. H. ir CHEN, C. L. Buoyancy-induced periodic flow and heat transfer in lid-driven cavities with different cross-sectional shapes. *International Communications in Heat and Mass Transfer*. 2005, 32(3–4), 483–490. ISSN 07351933.
  22. CHENG, J. Heat Transfer Enhancement of a Heated Block in the Channel With Cavity By Using Unsteady. *International Journal of Thermal Sciences*. 2005, 571–8. ISSN 12900729.
  23. CHENG, M. ir HUNG, K. C. Vortex structure of steady flow in a rectangular cavity. *Computers and Fluids*. 2006, 35(10), 1046–1062. ISSN 00457930.
  24. CHIATTO, M., HLEVCA, D., GRASSO, F., ir DE LUCA, L. Modal analysis of actively controlled flow past a backward facing ramp. 2020, (January),
  25. CHOI, H., MOIN, P., ir KIM, J. *Direct numerical simulation of turbulent flow over riblets*. *J. Fluid Mech*. 1993
  26. CHUN, K. B. ir SUNG, H. J. Control of turbulent separated flow over a backward-facing step by local forcing. *Experiments in Fluids*. 1996, 21(6), 417–426. ISSN 07234864.
  27. CHUNG, K. M., LEE, K. H., ir CHANG, K. C. Characteristics of cylindrical cavities in a compressible turbulent flow. *Aerospace Science and Technology*. 2017, 66160–164. ISSN 12709638.
  28. COLEMAN, S. E., NIKORA, V. I., MCLEAN, S. R., ir SCHLICKE, E. No Title. *Journal of Engineering Mechanics*. 2007, 133(2), 194–204. ISSN 0733-9399.
  29. DANDOIS, J., GARNIER, E., ir SAGAUT, P. Numerical simulation of active separation control by a synthetic jet. *Journal of Fluid Mechanics*. 2007, 57425–58. ISSN 0022-1120.
  30. DAS, S. ir COHEN, J. Effect of rear face geometry on the open cavity oscillatory flow at  $M=0.9$ . *8th AIAA Flow Control Conference*. 2016, (June), 1–12.
  31. DAVLETSHIN, I. A., ASLAEV, A. K., MIKHEEV, N. I., ir PAERELIY, A. A. Heat transfer in turbulent separation region of pulsating flow behind a backward-facing step. *Thermophysics and Aeromechanics*. 2019, 26(4), 519–529. ISSN 0869-8643.
  32. DAWOOD, A. S., KROUSH, F. A., ABUMANDOUR, R. M., ir ELDESOKY, I. M. Pulsatile nanofluid flow with variable pressure gradient and heat transfer in wavy channel. *Scientific Reports*. 2024, 14(1), 1–23. ISSN 20452322.
  33. DENG, Y., HE, C., WANG, P., ir LIU, Y. Unsteady behaviors of separated flow over a finite blunt plate at different inclination angles. *Physics of Fluids*. 2020, 32(3), ISSN 10897666.
  34. DESIKAN, S. L. N., PANDIAN, S., SIMHA, P. P., ir SAHOO, N. Experiments on flow past cavity and the application of modal decomposition techniques. *European Journal of Mechanics, B/Fluids*. 2022, 94293–298. ISSN 09977546.
  35. DINCAU, B., DRESSAIRE, E., ir SAURET, A. Pulsatile Flow in Microfluidic Systems. *Small*. 2020, 16(9), 1–18. ISSN 16136829.

36. DOL, S. S. Particle image velocimetry investigation of steady flow over a backwardfacing step. *EPJ Web of Conferences*. 2016, 1142018. ISSN 2100-014X.
37. DOL, S. S., SALEK, M. M., ir MARTINUZZI, R. J. Effects of Pulsation to the Mean Field and Vortex Development in a Backward-Facing Step Flow. *Journal of Fluids Engineering*. 2014, 136(1), 2–7. ISSN 0098-2202.
38. EZZATNESHAN, E. Study of unsteady separated fluid flows using a multi-block lattice Boltzmann method. *Aircraft Engineering and Aerospace Technology*. 2021, 93(1), 139–149. ISSN 17488842.
39. FAN, M., DONG, X., LI, Z., SUN, Z., ir FENG, L. Numerical and experimental study on flow separation control of airfoils with various leading-edge tubercles. *Ocean Engineering*. 2022, 252(March), 111046. ISSN 00298018.
40. FAURE, T. M., ADRIANOS, P., LUSSEYRAN, F., ir PASTUR, L. Visualizations of the flow inside an open cavity at medium range Reynolds numbers. *Experiments in Fluids*. 2007, 42(2), 169–184. ISSN 07234864.
41. FAURE, T. M., PASTUR, L., LUSSEYRAN, F., FRAIGNEAU, Y., ir BISCH, D. Three-dimensional centrifugal instabilities development inside a parallelepipedic open cavity of various shape. *Experiments in Fluids*. 2009, 47(3), 395–410. ISSN 07234864.
42. FAURE, T. M. Velocity field and parametric analysis of a subsonic, medium-Reynolds number cavity flow. *Experiments in Fluids*. 2014, 55(11), 1822. ISSN 0723-4864.
43. FISHLER, R., MULLIGAN, M. K., ir SZNITMAN, J. Mapping low-Reynolds-number microcavity flows using microfluidic screening devices. *Microfluidics and Nanofluidics*. 2013, 15(4), 491–500. ISSN 16134982.
44. GAO, W., SAMTANEY, R., ir PARSANI, M. Direct numerical simulation of transitional flow past an airfoil with partially covered wavy roughness elements. *Physics of Fluids*. 2022, 34(10), ISSN 10897666.
45. GHAEMI, S. Passive and active control of turbulent flows. *Physics of Fluids*. 2020, 32(8), 10–12. ISSN 10897666.
46. GOKTEPELI, İ. ir ATMACA, U. Numerical Modeling of Backward-Facing Step Flow Via Computational Fluid Dynamics. *Journal of Scientific Reports-A*. 2023, (054), 176–193.
47. GONG, S. C., LIU, R. G., CHOU, F. C., ir CHIANG, A. S. T. Experiment and simulation of the recirculation flow in a CVD reactor for monolithic materials. *Experimental Thermal and Fluid Science*. 1996, 12(1), 45–51. ISSN 08941777.
48. GRILLE GUERRA, A., MERTENS, C., LITTLE, J., ir VAN OUDHEUSDEN, B. Experimental characterization of an unsteady laminar separation bubble on a pitching wing. *Experiments in Fluids*. 2023, 64(1), 1–19. ISSN 14321114.
49. GUO, G. ir LUO, Q. Flowfield structure characteristics of the hypersonic flow over a cavity: From the continuum to the transition flow regimes. *Acta Astronautica*. 2019, 161(April), 87–100. ISSN 00945765.
50. H K VERSTEEG, W. M. An introduction to computational fluid dynamics : the finite volume method [OpenFOAM]. 2007, 500.
51. HAN, J., HE, L., XU, X., ir WU, Z. Experimental Investigation of a Roughness Element Wake on a Hypersonic Flat Plate. *Aerospace*. 2022, 9(10), ISSN 22264310.
52. HENDERSON, J., BADCOCK, K., ir RICHARDS, B. E. Subsonic and transonic transitional cavity flows. *6th Aeroacoustics Conference and Exhibit*. 2000
53. HILLEWAERE, J., DOOMS, D., VAN QUEKELBERGHE, B., DEGROOTE, J., VIERENDEELS, J., DE ROECK, G., LOMBAERT, G., ir DEGRANDE, G. Unsteady

- Reynolds averaged Navier-Stokes simulation of the post-critical flow around a closely spaced group of silos. *Journal of Fluids and Structures*. 2012, 3051–72. ISSN 08899746.
54. HU, Y., WERNER, C., ir LI, D. Influence of Three-Dimensional Roughness on Pressure-Driven Flow Through Microchannels. *Journal of Fluids Engineering, Transactions of the ASME*. 2003, 125(5), 871–879. ISSN 00982202.
  55. HUANG, H., BIAN, Y., LIU, Y., ZHANG, F., ARIMA, H., ir IKEGAMI, Y. Numerical and experimental analysis of heat transfer enhancement and pressure drop characteristics of laminar pulsatile flow in grooved channel with different groove lengths. *Applied Thermal Engineering*. 2018, 137(August 2017), 632–643. ISSN 13594311.
  56. IBRAHIM, M. ir HASHIM, W. Oscillating flow in channels with a sudden change in cross section. *Computers & Fluids*. 1994, 23(1), 211–224. ISSN 00457930.
  57. ISLAM, N. ir STEPHEN, S. J. Separation flow through asymmetric periodic tubes. *Partial Differential Equations in Applied Mathematics*. 2023, 7(March), 100511. ISSN 26668181.
  58. ISMAIL, M. S., BERBER, M. R., ALROWAILI, Z. A., ir POURKASHANIAN, M. Fully-developed laminar flow in trapezoidal ducts with rounded corners: a numerical solution and case study. *International Journal of Numerical Methods for Heat and Fluid Flow*. 2022, 32(8), 2682–2699. ISSN 09615539.
  59. ISSAKHOV, A., ZHANDAULET, Y., ABYLKASSYOMOVA, A., SAKYPBEKOVA, M., ir ISSAKHOV, A. Mixed convection in a channel with buoyancy force over backward and forward facing steps: The effects of inclination and geometry. *Case Studies in Thermal Engineering*. 2021, 26ISSN 2214157X.
  60. JIN, X., WANG, B., CHENG, X., WANG, Q., ir HUANG, F. Effects of corner rounding on aerothermodynamic properties in rarefied hypersonic flows over an open cavity. *Aerospace Science and Technology*. 2021, 110ISSN 12709638.
  61. JOSHI, S. N., WAGH, K. K., ir GUJARATHI, Y. S. A Review on Active and Passive Flow Control Techniques. *International Journal on Recent Technologies in Mechanical and Electrical Engineering*. 2016, 3(4), 1–6. ISSN 2349-7947.
  62. JULIAN, J., ANGGARA, R. A., ir WAHYUNI, F. The Influence of Fillet Step on Backward-Facing Step Flow Characteristics. *Infotekmesin*. 2023, 14(2), 318–326. ISSN 2087-1627.
  63. KHERBEET, A. S., MOHAMMED, H. A., MUNISAMY, K. M., ir SALMAN, B. H. The effect of step height of microscale backward-facing step on mixed convection nanofluid flow and heat transfer characteristics. *International Journal of Heat and Mass Transfer*. 2014, 68554–566. ISSN 00179310.
  64. KOURTA, A., THACKER, A., ir JOUSSOT, R. Analysis and characterization of ramp flow separation. *Experiments in Fluids*. 2015, 56(5), 1–14. ISSN 07234864.
  65. KUMAR, N. Numerical Simulation on Flow Behaviors over Backward Facing Rounded Step Applying Hybrid RANS-LES. *IJRAR-International Journal of Research and Analytical Reviews*. 2017, 5ISSN 2349-5138.
  66. KUMAR, R., KUMAR, A., ir GOEL, V. Effect of Rounded Corners on Heat Transfer and Fluid Flow Through Triangular Duct. *Journal of Heat Transfer*. 2018, 140(12), ISSN 15288943.
  67. LALEGANI, F., SAFFARIAN, M. R., MORADI, A., ir TAVOUSHI, E. Effects of different roughness elements on friction and pressure drop of laminar flow in microchannels. *International Journal of Numerical Methods for Heat and Fluid Flow*. 2018, 28(7), 1664–1683. ISSN 09615539.

68. LALITHA, K., VEERANNA, Y., THIMMAPPA SREENIVASA, G., ir ASHOK REDDY, D. Active and passive control of nanoparticles in ferromagnetic Jeffrey fluid flow. *Heat Transfer*. 2022, 51(1), 998–1018. ISSN 26884542.
69. LAOUIRA, H., MEBAREK-LOUDINA, F., HUSSEIN, A. K., KOLSI, L., MERAH, A., ir YOUNIS, O. Heat transfer inside a horizontal channel with an open trapezoidal enclosure subjected to a heat source of different lengths. *Heat Transfer - Asian Research*. 2020, 49(1), 406–423. ISSN 15231496.
70. LEONARDI, S., ORLANDI, P., SMALLEY, R. J., DJENIDI, L., ir ANTONIA, R. A. Direct numerical simulations of turbulent channel flow with transverse square bars on one wall. *Journal of Fluid Mechanics*. 2003, 491(491), 229–238. ISSN 00221120.
71. LI, X., LI, C., SU, W., ir WU, J. Experiment of influence of distributed roughness elements on hypersonic boundary layer instability. *Hangkong Xuebao/Acta Aeronautica et Astronautica Sinica*. 2024, 45(2), ISSN 10006893.
72. LIM, K. S., PARK, S. O., ir SHIM, H. S. A low aspect ratio backward-facing step flow. *Experimental Thermal and Fluid Science*. 1990, 3(5), 508–514. ISSN 08941777.
73. LIU, L., HAN, L., SHI, X., TAN, W., CAO, W., ir ZHU, G. Hydrodynamic separation by changing equilibrium positions in contraction–expansion array channels. *Microfluidics and Nanofluidics*. 2019, 23(4), 0. ISSN 16134990.
74. LIU, Y., LI, J., ir SMITS, A. J. Roughness effects in laminar channel flow. *Journal of Fluid Mechanics*. 2019, 8761129–1145. ISSN 0022-1120.
75. MA, X., TANG, Z., ir JIANG, N. Experimental study of self-sustained spanwise streaks and turbulent mixing in separated shear flow. *International Journal of Heat and Fluid Flow*. 2022, 96ISSN 0142727X.
76. MANNA, P. ir CHAKRABORTY, D. Numerical Investigation of Confinement Effect on Supersonic Turbulent Flow Past Backward Facing Step With And Without Transverse Injection. *Journal of Aerospace Sciences and Technologies*. 2023, 283–294. ISSN 0972-950X.
77. MARQUET, O., SIPP, D., ir JACQUIN, L. *Global optimal perturbations in a separated flow over a backward-rounded-step*. 2006
78. MCEVOY, J., ALIMOHAMMADI, S., ir PERSOONS, T. Experimental investigation of flow pulsation waveforms in rectangular mesochannels for high heat flux electronics cooling. *Experimental Thermal and Fluid Science*. 2019, 109ISSN 08941777.
79. MDMOLLA, M. ir PAUL, M. C. Large eddy simulation of pulsatile flow through a channel with double constriction. *Fluids*. 2017, 2(1), ISSN 23115521.
80. MOODY, L. F. Friction Factors for Pipe Flow. *Journal of Fluids Engineering, Transactions of the ASME*. 1944, 66(8), 671–678. ISSN 1528901X.
81. MOULINOS, I., MANOPOULOS, C., ir TSANGARIS, S. Computational Analysis of Active and Passive Flow Control for Backward Facing Step. *Computation*. 2022, 10(1), 12. ISSN 2079-3197.
82. MUFTUOGLU, A. ir BILGEN, E. Conjugate heat transfer in open cavities with a discrete heater at its optimized position. *International Journal of Heat and Mass Transfer*. 2008, 51(3–4), 779–788. ISSN 00179310.
83. MURUGAN, J. N. ir GOVARDHAN, R. N. Supersonic Flow Separation in Front of a Forward-Facing Step. *Journal of Aerospace Sciences and Technologies*. 2023, (February 2015), 563–573. ISSN 0972-950X.
84. MUSHYAM, A., BERGADA, J. M., ir NAVID NAYERI, C. A numerical investigation of laminar flow over a backward facing inclined step. *Meccanica*. 2016, 51(8), 1739–1762. ISSN 15729648.

85. NEUMANN, J. ir WENGLE, H. Coherent structures in controlled separated flow over sharp-edged and rounded steps. *Journal of Turbulence*. 2004, 5ISSN 14685248.
86. NISHIMURA, T., OKA, N., YOSHINAKA, Y., ir KUNITSUGU, K. Influence of imposed oscillatory frequency on mass transfer enhancement of grooved channels for pulsatile flow. *International Journal of Heat and Mass Transfer*. 2000, 43(13), 2365–2374. ISSN 00179310.
87. OYENIRAN, N. D., MIYAKE, T., TERASHIMA, H., SEKI, R., ISHIKO, K., ir NONOMURA, T. Unsteady Aerodynamics Around a Pitching Airfoil with Shock and Shock-Induced Boundary-Layer Separation. *AIAA Journal*. 2022, 60(12), 6557–6565. ISSN 0001-1452.
88. PELEVIĆ, N. ir VAN DER MEER, T. H. Heat transfer and pressure drop in microchannels with random roughness. *International Journal of Thermal Sciences*. 2016, 99125–135. ISSN 12900729.
89. PERSOONS, T., SAENEN, T., VAN OEVELEN, T., ir BAELEMANS, M. Effect of flow pulsation on the heat transfer performance of a minichannel heat sink. *Journal of Heat Transfer*. 2012, 134(9), ISSN 00221481.
90. POCHYLÝ, F., FIALOVÁ, S., ir ŠTEFAN, D. Effect of spiral vortices on the stability of vortex structures in the diffuser. *IOP Conference Series: Earth and Environmental Science*. 2019, 240(2), ISSN 17551315.
91. PRAKASH, M., KEDARE, S. B., ir NAYAK, J. K. Numerical study of natural convection loss from open cavities. *International Journal of Thermal Sciences*. 2012, 51(1), 23–30. ISSN 12900729.
92. RAFFEL, M., WILLERT, C. E., SCARANO, F., KÄHLER, C. J., WERELEY, S. T., ir KOMPENHANS, J. Particle Image Velocimetry: A Practical Guide. *Particle Image Velocimetry: A Practical Guide*. 2018, 1–32.
93. RAWOOL, A. S., MITRA, S. K., ir KANDLIKAR, S. G. Numerical simulation of flow through microchannels with designed roughness. *Microfluidics and Nanofluidics*. 2006, 2(3), 215–221. ISSN 16134982.
94. RINCÓN, M. J., RECLARI, M., YANG, X. I. A., ir ABKAR, M. Validating the design optimisation of ultrasonic flow meters using computational fluid dynamics and surrogate modelling. *International Journal of Heat and Fluid Flow*. 2023, 100(January), 109112. ISSN 0142727X.
95. RINCÓN, M. J., CASPERSEN, A., INGWERSEN, N. T., RECLARI, M., ir ABKAR, M. Flow investigation of two-stand ultrasonic flow meters in a wide dynamic range by numerical and experimental methods. *Flow Measurement and Instrumentation*. 2024, 96(April), 102543. ISSN 09555986.
96. RINCÓN, M. J., RECLARI, M., ir ABKAR, M. Turbulent flow in small-diameter ultrasonic flow meters: A numerical and experimental study. *Flow Measurement and Instrumentation*. 2022, 87(August), 102227. ISSN 09555986.
97. ROHACS, D., YASAR, O., KALE, U., EKICI, S., YALCIN, E., MIDILLI, A., ir KARAKOC, T. H. Past and current components-based detailing of particle image velocimetry: A comprehensive review. *Heliyon*. 2023, 9(3), e14404. ISSN 24058440.
98. ROVENSKAYA, O. I. Numerical analysis of surface roughness effects on the Poiseuille flow caused by a small pressure drop. *International Journal of Heat and Mass Transfer*. 2017, 110817–826. ISSN 00179310.
99. SALEK, M. M., DOL, S. S., ir MARTINUZZI, R. J. Analysis of Pulsatile Flow in a Separated Flow Region. *ASME 2009 Fluids Engineering Division Summer Meeting*. 2009. p. 1429–1438
100. SELIMEFENDIGIL, F. Numerical analysis of mixed convection in pulsating flow for

- a horizontal channel with a cavity heated from below. *Thermal Science*. 2016, 20(1), 35–44. ISSN 03549836.
101. SHEN, F., XU, M., WANG, Z., ir LIU, Z. M. Single-particle trapping, orbiting, and rotating in a microcavity using microfluidics. *Applied Physics Express*. 2017, 10(9), ISSN 18820786.
  102. SHEN, F., XIAO, P., ir LIU, Z. Microparticle image velocimetry ( $\mu$ PIV) study of microcavity flow at low Reynolds number. *Microfluidics and Nanofluidics*. 2015, 19(2), 403–417. ISSN 16134990.
  103. STOESSER, T. ir NIKORA, V. I. Flow structure over square bars at intermediate submergence: Large Eddy Simulation study of bar spacing effect. *Acta Geophysica*. 2008, 56(3), 876–893. ISSN 18956572.
  104. STOGIANNIS, I. A., PASSOS, A. D., MOUZA, A. A., PARAS, S. V., PĚNKAVOVÁ, V., ir TIHON, J. Flow investigation in a microchannel with a flow disturbing rib. *Chemical Engineering Science*. 2014, 11965–76. ISSN 00092509.
  105. TIAN, Y. ir CATTAFESTA III, L. N. *Adaptive Control of Separated Flow*. 2006
  106. TIHON, J., PĚNKAVOVÁ, V., HAVLICA, J., ir ŠIMČÍK, M. The transitional backward-facing step flow in a water channel with variable expansion geometry. *Experimental Thermal and Fluid Science*. 2012, 40112–125. ISSN 08941777.
  107. TIHON, J., LEGRAND, J., ir LEGENTILHOMME, P. Near-wall investigation of backward-facing step flows. *Experiments in Fluids*. 2001, 31(5), 484–493. ISSN 0723-4864.
  108. TIHON, J., PĚNKAVOVÁ, V., ir PANTZALI, M. The effect of inlet pulsations on the backward-facing step flow. *European Journal of Mechanics - B/Fluids*. 2010, 29(3), 224–235. ISSN 09977546.
  109. TRACY, M. B. ir PLENTOVICH, E. B. Cavity unsteady-pressure measurements at subsonic and transonic speeds. *NASA Technical Paper*. 1997, 3669(December 1997),
  110. VALENCIA, A. Pulsating Flow in a Channel With a Backward-Facing Step. *Applied Mechanics Reviews*. 1997, 50(11S), S232–S236. ISSN 0003-6900.
  111. VALENCIA, A. ir HINOJOSA, L. Numerical solutions of pulsating flow and heat transfer characteristics in a channel with a backward-facing step. *Heat and Mass Transfer*. 1997, 32(3), 143–148. ISSN 0947-7411.
  112. VANIERSCHOT, M., VERRIJSEN, T. A. J., VAN BUGGENHOUT, S., HENDRICKX, M., ir VAN DEN BULCK, E. Experimental and numerical analysis of an apparatus to apply controlled shear/elongation in fluid flows. *Chemical Engineering Science*. 2014, 11388–94. ISSN 00092509.
  113. VARUN KUMAR, R., NAGARAJA, K. V., ir CHANDAN, K. Unsteady incompressible flow over a backward-facing step using FEniCS. *Materials Today: Proceedings*. 2023, (March), ISSN 22147853.
  114. VELAZQUEZ, A., ARIAS, J. R., ir MONTANES, J. L. Pulsating flow and convective heat transfer in a cavity with inlet and outlet sections. *International Journal of Heat and Mass Transfer*. 2009, 52(3–4), 647–654. ISSN 00179310.
  115. VILKINIS, P. *Skysčio srauto dinamikos ir struktūros tyrimas kanaluose su struktūrizuotais paviršiais*. s.a. Kaunas: Technologija, 2019 m. ISBN 978-609-02-1669-9
  116. VILKINIS, P. ir PEDIŠIUS, N. Analysis of reattachment length dynamics in cavities. *Experimental Thermal and Fluid Science*. 2020, 119(November 2019), ISSN 08941777.
  117. VILKINIS, P., PEDIŠIUS, N., ir VALANTINAVIČIUS, M. Investigation of Flow Dynamics over Transitional-Type Microcavity. *Journal of Fluids Engineering*,

- Transactions of the ASME*. 2018, 140(7), 3–9. ISSN 1528901X.
118. WANG, J., MA, T., WANG, Z., WANG, R., SONG, H., YUAN, W., ir ZHENG, H. Three-dimensional flow structures and heat transfer characteristics of compressible flow over a cylindrical cavity. *Aerospace Science and Technology*. 2022, 122ISSN 12709638.
  119. WANG, R., ZUO, X., HE, Y., PI, W., ZHU, Y. P., WU, C., ir WEI, Y. Numerical study of the effects of aspect ratio and Reynolds number on the flow over a rectangular cylinder with rounded corners. *Ocean Engineering*. 2024, 297(September 2023), 117115. ISSN 00298018.
  120. WANG, Y., HU, Z., ir THOMPSON, D. Numerical investigations on the flow over cubes with rounded corners and the noise emitted. *Computers and Fluids*. 2020, 202ISSN 00457930.
  121. WARD, K. ir FAN, Z. H. Mixing in microfluidic devices and enhancement methods. *Journal of Micromechanics and Microengineering*. 2015, 25(9), ISSN 13616439.
  122. WILLIAMS, P. T. ir BAKER, A. J. Numerical simulations of laminar flow over a 3D backward-facing step. *International Journal for Numerical Methods in Fluids*. 1997, 24(11), 1159–1183. ISSN 02712091.
  123. WONG, W. S., QIN, N., SELLARS, N., HOLDEN, H., ir BABINSKY, H. A combined experimental and numerical study of flow structures over three-dimensional shock control bumps. *Aerospace Science and Technology*. 2008, 12(6), 436–447. ISSN 12709638.
  124. WU, W. C. ir KUMAR, A. Numerical Investigation of Nanofluid Flow over a Backward Facing Step. *Aerospace*. 2022, 9(9), ISSN 22264310.
  125. XIA, L., HUA, Y., ir ZHENG, J. G. Numerical investigation of flow separation control over an airfoil using fluidic oscillator. *Physics of Fluids*. 2021, 33(6), ISSN 10897666.
  126. XIAO, H. ir CINNELLA, P. Quantification of model uncertainty in RANS simulations: A review. *Progress in Aerospace Sciences*. 2019, 108(June 2018), 1–31. ISSN 03760421.
  127. XIE, W. A., XI, G. N., ir ZHONG, M. B. Effet de la structure vortique sur le transfert de chaleur dans l'écoulement transitionnel orienté vers l'arrière. *International Journal of Refrigeration*. 2017, 74463–472. ISSN 01407007.
  128. YIN, Y. Current study on active flow control and passive flow control. *Theoretical and Natural Science*. 2023, 26(1), 227–234. ISSN 2753-8818.
  129. YUAN, X., TAO, Z., LI, H., ir TIAN, Y. Experimental investigation of surface roughness effects on flow behavior and heat transfer characteristics for circular microchannels. *Chinese Journal of Aeronautics*. 2016, 29(6), 1575–1581. ISSN 10009361.
  130. YUSOF, S. N. A., ASAKO, Y., SIDIK, N. A. C., MOHAMED, S. B., ir JAPAR, W. M. A. A short review on rans turbulence models. *CFD Letters*. 2020, 12(11), 83–96. ISSN 21801363.
  131. ZAMZARI, F., MEHREZ, Z., EL CAFSI, A., BELGHITH, A., ir LE QUÉRÉ, P. Numerical investigation of entropy generation and heat transfer of pulsating flow in a horizontal channel with an open cavity. *Journal of Hydrodynamics*. 2017, 29(4), 632–646. ISSN 18780342.
  132. ZHANG, C., CHEN, Y., ir SHI, M. Effects of roughness elements on laminar flow and heat transfer in microchannels. *Chemical Engineering and Processing: Process Intensification*. 2010, 49(11), 1188–1192. ISSN 02552701.
  133. ZHANG, F., BIAN, Y., LIU, Y., PAN, J., YANG, Y., ir ARIMA, H. Experimental and numerical analysis of heat transfer enhancement and flow characteristics in

- grooved channel for pulsatile flow. *International Journal of Heat and Mass Transfer*. 2019, 1411168–1180. ISSN 00179310.
134. ZHANG, J., MORISHITA, E., OKUNUKI, T., ir ITOH, H. Experimental investigation on the mechanism of flow-type changes in supersonic cavity flows. *Transactions of the Japan Society for Aeronautical and Space Sciences*. 2002, 45(149), 170–179. ISSN 05493811.
135. ZHANG, Q., LUO, S., MA, H., WANG, X., ir QIAN, J. Simulation on the water flow affected by the shape and density of roughness elements in a single rough fracture. *Journal of Hydrology*. 2019, 573(March), 456–468. ISSN 00221694.
136. ZHANG, Y., EICHHOLZ, B., ir ZHANG, R. Evolution of vortex structures in an open deep cavity under pulsatile flow conditions: An experimental study. *Physics of Fluids*. 2022, 34(9), ISSN 10897666.
137. ZHANG, Y. Z., SUN, C., BAO, Y., ir ZHOU, Q. How surface roughness reduces heat transport for small roughness heights in turbulent Rayleigh-Bénard convection. *Journal of Fluid Mechanics*. 2018, 836R2. ISSN 14697645.



## **CURRICULUM VITAE**

Vardas: Justas

Pavardė: Šereika

Gimimo vieta: Kaunas, Lietuva

El. paštas: justas.sereika@gmail.com

Išsilavinimas:

2014-2018: Kauno technologijos universitetas, šiluminės energetikos ir technologijų bakalauras

2018-2020: Kauno technologijos universitetas, termoinžinerijos magistras

2020-2024: Lietuvos energetikos institutas, doktorantūros studijos technologinių mokslų kryptyje (energetika ir termoinžinerija, T 006)

## PUBLICATIONS RELATED TO THE DISSERTATION

### Articles in journals from “Clarivate Analytics” “Web of Science” database list

1. Šereika J., Vilkinis P., Pedišius N. Investigation of pulsatile flow structure in closed-type cavity. *International Journal of Heat and Fluid Flow*. 2021, Vol. 92, 108877, p. 1-7. ISSN 0142-727X.
2. Šereika J., Vilkinis P., Pedišius N. Analysis of Cavity Corner Geometry Effect on Recirculation Zone Structure. *Applied Sciences*. 2022, Vol. 12, Iss. 12, 6288, p. 1-12. ISSN 2076-3417.
3. Vilkinis P., Šereika J., Pedišius N., Zygmantas G. Experimental study of flows over triangular riblets in cavity-like geometry. *Experimental Thermal and Fluid Science*. New York: Elsevier, 2022, Vol. 134, 110621, p. 1-9. ISSN 0894-1777.
4. Šereika J., Vilkinis P., Skarbalius G., Džiugys A., Pedišius N. Experimental analysis of pulsatile flow effects on flow structure in transitional-type cavity. *Experimental Thermal and Fluid Science*. New York: Elsevier, 2024, Vol. 151, 111073, p. 1-10. ISSN 0894-1777.

### Reports in the international conferences

1. Šereika J. Experimental and numerical analysis of the flow structure in cavities under pulsatile inlet flow conditions. *The 17th International Conference of Young Scientists on Energy and Natural Sciences Issues (CYSENI 2021)*. Kaunas, Lithuania, May 24-28, 2021. Kaunas: Lietuvos energetikos institutas, 2021, p. 585-586. ISSN 1822-7554.
2. Šereika J., Vilkinis P., Pedišius N. Investigation of pulsatile flow structure in closed-type cavity. *14th European Fluid Mechanics Conference (EFMC14)*. Athens, Megaron Athens International Conference Centre, 2022, Session 9, p. 951-951.
3. Šereika J., Vilkinis P., Pedišius N. Experimental analysis of pulsatile flow in a transitional-type cavity. *18th European Turbulence Conference (ETC18)*. 4-6 September, 2023. Valencia, Spain.

UDK 536.2[043.3]

SL344. 2024-07-29, 16,25 leidyb. apsk. I. Tiražas 14 egz. Užsakymas 135.

Išleido Kauno technologijos universitetas, K. Donelaičio g. 73, 44249 Kaunas

Spausdino leidyklos „Technologija“ spaustuvė, Studentų g. 54, 51424 Kaunas

